

The Synthesis and Characterization of Bisisoindigo Polymers with Electron-Deficient Comonomers for Applications in Organic Electronics

A Thesis Submitted to the College of Graduate and Postdoctoral Studies

In Partial Fulfillment of the Requirements for the Degree of Master of Science

In the Department of Chemistry

University of Saskatchewan

Saskatoon

By

Raymond N. Bennett

Permission to Use

In presenting this thesis in partial fulfillment of the requirements for a Postgraduate degree from the University of Saskatchewan, I agree that the Libraries of this University may make it freely available for inspection. I further agree that permission for copying of this thesis/dissertation in any manner, in whole or in part, for scholarly purposes may be granted by the professor or professors who supervised my thesis work or, in their absence, by the Head of the Department of Chemistry or the Dean of the College in which my thesis work was done. It is understood that any copying or publication or use of this thesis or parts thereof for financial gain shall not be allowed without my written permission. It is also understood that due recognition shall be given to me and to the University of Saskatchewan in any scholarly use which may be made of any material in my thesis/dissertation.

Requests for permission to copy or to make other uses of materials in this thesis in whole or part should be addressed to:

Head of the Department of Chemistry

University of Saskatchewan

170 Thorvaldson Building, 110 Science Place

Saskatoon, Saskatchewan S7N 5C9

Canada

OR

Dean

College of Graduate and Postdoctoral Studies

University of Saskatchewan

116 Thorvaldson Building, 110 Science Place

Saskatoon, Saskatchewan S7N 5C9

Canada

Abstract

Organic electronic materials can be used to make low cost, lightweight, and flexible electronic devices that are not possible with traditional inorganic semiconductors. New semiconductors with improved properties will be required to commercialize these devices. This thesis describes the synthesis of new conjugated polymers using the bisisoindigo structure coupled with electron-deficient thiophene dioxide or benzothiadiazole comonomers. These materials combine a core-expanded isoindigo structure with a polymer design that uses all electron-deficient comonomers. The synthesis of thiophene dioxide-containing polymers was attempted through both the synthesis of thiophene dioxide monomers and through post-polymerization modification. Bisisoindigo polymers with a benzothiadiazole comonomer were synthesized using the Stille reaction. The optoelectronic and physical properties of these polymers were characterised, and the materials were applied in organic field effect transistors (OFETs). Ambipolar device performance was observed in OFETs with hole and electron mobilities up to $4.0 \times 10^{-3} \text{ cm}^2 \text{ V}^{-1} \text{ s}^{-1}$ and $1.4 \times 10^{-3} \text{ cm}^2 \text{ V}^{-1} \text{ s}^{-1}$ respectively. Additionally, proper selection of OFET source and drain electrodes produced devices with improved threshold voltages by improving energy alignment between the polymer frontier molecular orbital energies and the contact metal.

Acknowledgements

I would first like to thank my supervisor Dr. Tim Kelly for being unbelievably helpful and supportive throughout my degree. Tim showed a lot of trust in me to take me on as a graduate student just before going on sabbatical. I have learned more than I could have hoped during my degree, and despite some bumps along the way, I can not imagine a more knowledgeable and supportive supervisor.

I would also like to thank all of Kelly group members who have helped me during my degree, particularly Chase Radford, Anindya Ganguly, Kyle Fransishyn, and Derek Zomerman for helpful advice along the way and lots of interesting conversations while washing glassware in the lab.

The University of Saskatchewan Chemistry Department has been hugely supportive and helpful, and as there are too many people to name individually, I would like to thank all of the committee members, professors, instructors, lab coordinators, administrators and support staff that have helped me during my time here.

Many friends and family members across the country have also been very supportive of my studies, which I am very grateful for. From old friends at home and new friends I have met in Saskatoon, these people helped to make my time in graduate school much more enjoyable.

Finally, I would like to thank you, the reader. Completing this thesis was a lot of work; I hope you enjoy reading it as much as I enjoyed writing it.

Table of Contents

Permission to Use	ii
Abstract	iii
Acknowledgements.....	iv
Table of Contents.....	v
List of Figures	ix
List of Charts	xiv
List of Schemes.....	xv
List of Equations	xvi
List of Tables	xvii
Co-Authorship Statement	xviii
List of Symbols and Abbreviations	xix
Chapter 1 – Introduction.....	1
1.1 Organic Semiconductors.....	1
1.1.1 Band Theory and Electronic Conduction in Organic Semiconductors	1
1.2 Chemistry of Conjugated Polymers.....	3
1.2.1 Synthesis of Conjugated Polymers.....	3
1.2.2 Defining Polymer Molecular Weights	6
1.3 Organic Field Effect Transistors.....	8
1.3.1 Architecture and Operation of OFETs	9
1.3.2 Figures of Merit for OFET Devices	12
1.4 Material Design of Organic Semiconductors for n-Channel OFETs.....	21
1.4.1 Donor-Acceptor Design Strategy in Organic Semiconductors	22

1.4.2 Isoindigo – From Dyes to Semiconductors	23
1.4.3 Acceptor-Acceptor Isoindigo Polymers	29
1.4.4 Structural Modifications of Isoindigo	31
1.4.5 Core Expanded Isoindigo and Bisisoindigo Polymers.....	33
1.5 Thesis Objectives	43
Chapter 2 – Bisisoindigo Acceptor-Acceptor Polymers.....	44
2.1 Motivation for Electron-Deficient Bisisoindigo Polymers	44
2.2 Results and Discussion	45
2.2.1 Polymer Synthesis	45
2.2.2 Molecular Weights and Thermal Properties.....	47
2.2.3 DFT Optimized Polymer Structures	49
2.2.4 Polymer Optoelectronic Properties	51
2.2.5 Polymer Thin Film Morphologies	54
2.2.6 OFET Device Performance	57
2.3 Conclusions.....	62
Chapter 3 – Synthesis of Thiophene Dioxide Acceptors	63
3.1 Motivation for Thiophene Dioxides	63
3.2 Results and Discussion	64
3.2.1 Small Molecule Synthesis	64
3.2.2 Post-Polymerization Functionalization	67
3.3 Conclusions.....	72
Chapter 4 – Conclusions and Outlook.....	74
4.1 Summary and Conclusions	74
4.2 Discussion and Limitations.....	74
4.3 Future Work.....	75

Chapter 5 – Experimental	79
5.1 Materials and Methods.....	79
5.2 Gel Permeation Chromatography	80
5.3 Thermal Analysis.....	84
5.4 Computational Details	84
5.5 OFET Manufacturing and Testing	86
5.6 GIWAXS Measurements	86
5.7 Post-polymerization Functionalization	87
5.7.1 Titration of <i>m</i> -CPBA	87
5.7.2 Functionalization of BII-3T with <i>m</i> -CPBA.....	87
5.8 X-ray Photoelectron Spectroscopy	88
5.9 Detailed Synthetic Procedures	88
5.9.1 Synthesis of 2-trimethylstannyl thiophene (1)	88
5.9.2 Synthesis of 5,6-difluoro-2,1,3-benzothiadiazole (2).....	89
5.9.3 Synthesis of 4,7-dibromo-5,6-difluoro-2,1,3-benzothiadiazole (3)	89
5.9.4 Synthesis of 4,7-dithieno-2,1,3-benzothiadiazole (4)	90
5.9.5 Synthesis of 4,7-bis(5-(trimethylstannyl)thiophen-2-yl)-2,1,3-benzothiadiazole (5).....	90
5.9.6 Synthesis of 5,6-difluoro-4,7-dithieno-2,1,3-benzothiadiazole (6).....	91
5.9.7 Synthesis of 5,6-Difluoro-4,7-bis(5-(trimethylstannyl)thiophen-2-yl)-2,1,3-benzothiadiazole (7).....	91
5.9.8 Synthesis of Poly(bisindigo-dithienylbenzothiadiazole) P1(H)	92
5.9.9 Synthesis of Poly(bisindigo-difluoro-dithienyl-benzothiadiazole) P2(F)	93
5.9.10 Synthesis of Poly(bisindigo-benzothiadiazole) P3(B).....	94
5.9.11 Synthesis of 2,5-Trimethylsilylthiophene (8).....	94
5.9.12 Synthesis of 2,5-Trimethylsilylthiophene- <i>S,S</i> -dioxide (9)	95

5.9.13 Synthesis of 2,5-Dibromothiophene- <i>S,S</i> -dioxide (10)	95
5.9.14 Synthesis of 2,5-Thienylthiophene- <i>S,S</i> -dioxide (11)	96
5.9.15 Synthesis of 3,4-Dibutylthiophene (12)	96
5.9.16 Synthesis of 2,5-Dibromo-3,4-dibutylthiophene (13)	97
5.9.17 Synthesis of 3'4'-Dibutylterthiophene (14)	97
5.9.18 Synthesis of 3'4'-Dibutylterthiophene- <i>S',S'</i> -dioxide (15)	98
5.10 NMR Spectra	99
Chapter 6 – References	111

List of Figures

Figure 1.1	Molecular orbital energy level diagrams of conjugated oligomers extending towards poly(acetylene) and its band structure.	2
Figure 1.2	Layered device architectures for a) bottom-gate bottom-contact (BGBC) b) bottom-gate top-contact (BGTC) c) top-gate bottom-contact (TGBC) and d) top-gate top-contact (TGTC) organic field effect transistors, where the device substrate is on the bottom in each case.	9
Figure 1.3	Energy level diagrams showing operation of n-channel OFETs. a) Energy levels of the gate electrode and the semiconductor separated by the gate dielectric with no applied gate potential ($V_G = 0$). b) Application of a positive gate potential ($V_G > 0$) resulting in a lowering of the HOMO and LUMO energy levels near the gate dielectric. c) Sufficient lowering of the LUMO energy level because of applied V_G allows electron injection into the LUMO and a positive drain potential ($V_D > 0$) causes charges to move along the channel to be collected as the drain current.	10
Figure 1.4	BGBC OFET with labeled channel length and width. Positive potentials applied to the gate and drain electrodes relative to the grounded source electrode as required for n-channel device operation are also shown.....	14
Figure 1.5	BGBC OFET with region of significant charge carrier concentration highlighted with white stripes throughout device operation. Carrier concentrations displayed a) with $V_G > V_T$ and $V_D = 0$ b) $V_G - V_T \cong V_D$ (near the change from the linear to the saturation regime) and c) $V_G - V_T < V_D$ (the saturation regime).....	14
Figure 1.6	a) Output curves with varying gate potentials showing the linear (red dots) and saturation (blue dots) regimes. The intersection between the two regimes gives the pinch point in dashed black lines. b) Transfer curve (black line) for the saturation regime current plotted on a logarithmic scale. The square root of the current as a function of V_G is shown as a blue line on a linear scale, whose slope (in red) is usually used to determine μ_{sat} . The slope of the orange line is used to determine the sub-threshold swing, a measure of how quickly and easily the device turns from off to on. Adapted from Lamport, Z. A.; Haneef, H. F.; Anand, S.; Waldrip, M.; Jurchescu, O. D. Tutorial: Organic Field-Effect Transistors: Materials, Structure and Operation. <i>J. Appl. Phys.</i> 2018 , <i>124</i> , 071101. with the permission of AIP Publishing.....	17

Figure 1.7	Ordering of P3HT in thin films in a) edge-on or b) face-on molecular packing arrangements. Figure adapted with permission from Gargi, D.; Kline, R. J.; DeLongchamp, D. M.; Fischer, D. A.; Toney, M. F.; O'Connor, B. T. <i>J. Phys. Chem. C</i> 2013 , <i>117</i> , 17421–17428. Copyright 2013 American Chemical Society.....	18
Figure 1.8	Frontier molecular orbital energy levels of an electron rich donor and electron poor acceptor, and their combination to create a donor-acceptor system.	22
Figure 1.9	a) Isoindigo arylated in the 6,6' positions shown with its quinoidal resonance structure. b) Isoindigo arylated in the 5,5' positions, where a quinoidal resonance structure spanning the isoindigo unit is not present.	25
Figure 1.10	Classification of structural variants on isoindigo. Figure adapted with permission from Randell, N. M.; Kelly, T. L. Recent Advances in Isoindigo-Inspired Organic Semiconductors. <i>Chem. Rec.</i> 2019 , <i>18</i> , 1–17. Copyright 2019 John Wiley & Sons, Inc.	32
Figure 2.1	a) Thermal gravimetric analysis used to determine the polymer decomposition temperatures. The dashed grey line indicates a weight loss of 5%. b) Differential scanning calorimetry of the three polymer samples through a heating-cooling-heating cycle. Heating cycles were performed at 20 °C/minute.	48
Figure 2.2	Structures of DFT optimized oligomers representing a) P1(H) b) P2(F) c) P3(B). Indicated bond angles represent average dihedral angles for the same position in each repeat unit. d) Potential orientations of the dithienyl-benzothiadiazoles in P1(H) and P2(F).	50
Figure 2.3	a) UV/Vis absorption spectra for the three synthesized polymers in CHCl ₃ solution and as spin coated thin-films. b) TD-DFT simulated UV/Vis spectra for polymers P1(H) and P2(F). Extinction coefficients for the simulated spectra are shown on the left axis (in black) and oscillator strengths of the main contributing excitations are displayed as bars and correspond to the right axis (in purple). c) Differential pulse voltammetry scans of the three polymers. d) Cyclic voltammetry for the three studied polymers using a scan rate of 100mV/s.	52
Figure 2.4	GIWAXS patterns of spin-coated polymer thin films for a) as-cast P1(H) b) as-cast P2(F) c) as-cast P3(B) d) thermally annealed P1(H) e) thermally annealed P2(F) and f) thermally annealed P3(B).	55

Figure 2.5	Texture analysis of the lamellar stacking feature ($q = 0.30 - 0.39 \text{ \AA}^{-1}$) in GIWAXS patterns before and after thermal annealing for polymers a) P1(H), b) P2(F) and c) P3(B). Analysis performed for azimuthal angles from -85° to 85°	56
Figure 2.6	Line cuts of GIWAXS scattering patterns for thermally annealed polymer films of P1(H) and P2(F) taken along a) the q_r or b) the q_z axis.....	57
Figure 2.7	Transfer and output curves for BGBC, Au source/drain OFET devices. a) P1(H) p-channel transfer curves with V_D ranging from -80 to -100 V. b) P1(H) n-channel transfer curves with V_D ranging from 80 to 100 V. c) P1(H) output curves. d) P2(F) p-channel transfer curves with V_D ranging from -80 to -100 V. e) P2(F) n-channel transfer curves with V_D ranging from 80 to 100 V. f) P2(F) output curves.	58
Figure 2.8	Transfer and output curves for BGTC, LiF/Al source/drain OFET devices. a) P1(H) n-channel transfer curves with V_D of 100 V. b) P1(H) output curves. c) P2(F) n-channel transfer curves with V_D of 100 V. d) P2(F) output curves.....	61
Figure 3.1	UV/Vis spectra of bisisindigo-terthiophene reacting with <i>m</i> -CPBA as a function of time.	68
Figure 3.2	IR spectra of bisisindigo-terthiophene copolymer before and after reaction with <i>m</i> -CPBA.	69
Figure 3.3	Fitted XPS spectra of the S 2p region for a) bisisindigo-terthiophene polymer before and b) after reaction with <i>m</i> -CPBA.	71
Figure 3.4	Representation of the bisisindigo-terthiophene polymer after reaction with <i>m</i> -CPBA featuring segments of the polymer chain with unreacted bisisindigo (w), oxidized terthiophene units (x), epoxide functionalized bisisindigo units (y), and unreacted terthiophene units (z).	72
Figure 4.1	Thienobisisindigo, a proposed structural analogue of bisisindigo predicted to give a more planar structure.....	76
Figure 4.2	Comparison of dithienyl-benzothiadiazole used in Chapter 2 with proposed dithiazole-benzothiadiazole which could be paired with bisisindigo or thienobisisindigo to make acceptor-acceptor polymers.	76
Figure 4.3	Structures for centrosymmetric benzothiadiazole acceptor units flanked by thiophene or thiazole units.....	77
Figure 5.1	GPC calibration curve based on polyethylene standards.	80

Figure 5.2	GPC traces for P1(H) (top), P2(F) (middle), and P3(B) (bottom) collected using polyethylene standards.	81
Figure 5.3	GPC calibration curve based on polystyrene standards.	82
Figure 5.4	GPC traces for P1(H) (top) and P2(F) (bottom) collected using polystyrene standards.	83
Figure 5.5	TD-DFT calculated UV-Vis spectra for 2.5 repeat unit oligomers (ex. dTBT-BII-dTBT-BII-dTBT) using B3LYP/6-31G(d,p). The lower level of theory relative to ω B97XD allowed for modelling of longer oligomers and resulted in smaller calculated bandgaps more similar to experimental data, but gives poorer reproduction of experimental UV/Vis spectra.	84
Figure 5.6	Orbital isosurfaces for two-repeat-unit oligomers of a) P1(H) (BII-dTBT-BII-dTBT) and b) P2(F) (BII-FdTBT-BII-FdTBT). Isosurfaces generated using ω B97XD/6-31+G(d,p) using a dielectric constant equal to that of chloroform.	85
Figure 5.7	2-trimethylstannyl thiophene (1) ^1H NMR.	99
Figure 5.8	5,6-Difluoro-2,1,3-benzothiadiazole (2) ^{19}F NMR.	99
Figure 5.9	5,6-Difluoro-2,1,3-benzothiadiazole (2) ^{19}F NMR.	100
Figure 5.10	4,7-Dibromo-5,6-difluoro-2,1,3-benzothiadiazole (3) ^{19}F NMR.	100
Figure 5.11	4,7-Dithieno-2,1,3-benzothiadiazole (4) ^1H NMR.	101
Figure 5.12	4,7-Bis(5-(trimethylstannyl)thiophene-2-yl)-2,1,3-benzothiadiazole (5) ^1H NMR.	101
Figure 5.13	5,6-Difluoro-4,7-dithieno-2,1,3-benzothiadiazole (6) ^1H NMR.	102
Figure 5.14	5,6-Difluoro-4,7-dithieno-2,1,3-benzothiadiazole (6) ^{19}F NMR.	102
Figure 5.15	5,6-Difluoro-4,7-bis(5-(trimethylstannyl)thiophen-2-yl)-2,1,3-benzothiadiazole (7) ^1H NMR.	103
Figure 5.16	5,6-Difluoro-4,7-bis(5-(trimethylstannyl)thiophen-2-yl)-2,1,3-benzothiadiazole (7) ^{19}F NMR.	103
Figure 5.17	Poly(bisisoindigo-dithienobenzothiadiazole) P1(H) ^1H NMR.	104
Figure 5.18	Poly(bisisoindigo-difluoro,dithienobenzothiadiazole) P2(F) ^1H NMR.	104
Figure 5.19	Poly(bisisoindigo-difluoro,dithienobenzothiadiazole) P2(F) ^{19}F NMR.	105
Figure 5.20	Poly(bisisoindigo-benzothiadiazole) P3(B) ^1H NMR.	105
Figure 5.21	2,5-Trimethylsilylthiophene (8) ^1H NMR.	106

Figure 5.22	2,5-Trimethylsilylthiophene- <i>S,S</i> -dioxide (9) ^1H NMR.	106
Figure 5.23	2,5-Dibromothiophene- <i>S,S</i> -dioxide (10) ^1H NMR.	107
Figure 5.24	2,5-Thienylthiophene- <i>S,S</i> -dioxide (11) ^1H NMR.	107
Figure 5.25	2,5-Thienylthiophene- <i>S,S</i> -dioxide (11) ^{13}C NMR.	108
Figure 5.26	3,4-Dibutylthiophene (12) ^1H NMR.	108
Figure 5.27	2,5-Dibromo-3,4-dibutylthiophene (13) ^1H NMR.	109
Figure 5.28	3'4'-Dibutylterthiophene (14) ^1H NMR.	109
Figure 5.29	3'4'-Dibutylterthiophene- <i>S',S'</i> -dioxide (15) ^1H NMR.	110
Figure 5.30	3'4'-Dibutylterthiophene- <i>S',S'</i> -dioxide (15) ^{13}C NMR.	110

List of Charts

Chart 1.1	Sampling of common electron-rich donors (top row) and electron-deficient acceptors (bottom row) used in donor-acceptor conjugated polymers.	23
Chart 1.2	Structures of indigo and isoindigo as obtained from <i>Isatis tinctorial</i>	24
Chart 1.3	Survey of isoindigo donor-acceptor polymers for p-channel OFETs reported by Lei et al. ⁵⁸⁻⁶⁰	27
Chart 1.4	Survey of isoindigo-based acceptor-acceptor polymers used as electron conducting materials in organic electronics.....	30
Chart 1.5	Structures of core expanded isoindigo units in donor-acceptor polymers.	37
Chart 1.6	Structures of bisisoindigo and bisisoindigo containing polymers.	41
Chart 2.1	Structures of polymers synthesized and studied throughout Chapter 2.	45

List of Schemes

Scheme 1.1	General schemes of the Stille and Suzuki reaction for the synthesis of conjugated alternating copolymers. Pd ⁰ L _x represents a palladium(0) catalyst with an appropriate number of L-type ligands, which are generally triaryl phosphines.....	4
Scheme 1.2	a) Catalytic cycle mechanism for the Stille reaction. ¹⁴ b) Catalytic cycle mechanism for the Suzuki reaction. ^{15,16}	4
Scheme 1.3	Synthesis of isoindigo via acid catalyzed aldol condensation between isatin and oxindole.....	24
Scheme 2.1	Synthetic routes towards the Stille reagents used in polymerization reactions with dibromobisisoindigo. Detailed synthetic procedures and characterization data are given in Chapter 5.	46
Scheme 2.2	Synthesis of bisoindigo polymers P1(H), P2(F), and P3(B).	47
Scheme 3.1	Synthesis of terthiophene- <i>S',S'</i> -dioxide.....	65
Scheme 3.2	Synthesis of alkylated terthiophene dioxide.	66
Scheme 3.3	Predicted reactivity for post-polymerization modification of bisoindigo-terthiophene with <i>m</i> -CPBA.....	67
Scheme 4.1	DHAP synthesis of isoindigo-terthiophene dioxide copolymer. Synthetic conditions are general, as taken from DHAP reviews by Leclerc and coworkers. ¹⁹⁻²²	78
Scheme 4.2	Preparation of an electron conducting polymer by post-polymerization functionalization of ambipolar dithienyldiketopyrrolopyrrolo-benzothiadiazole copolymer using <i>m</i> -CPBA.	78

List of Equations

Equation 1.1	6
Equation 1.2	6
Equation 1.3	7
Equation 1.4	7
Equation 1.5	7
Equation 1.6	7
Equation 1.7	7
Equation 1.8	8
Equation 1.9	8
Equation 1.10	13
Equation 1.11	13
Equation 1.12	15
Equation 1.13	15
Equation 1.14	15
Equation 1.15	15
Equation 1.16	15
Equation 1.17	15
Equation 1.18	16
Equation 1.19	16
Equation 1.20	20
Equation 1.21	20

List of Tables

Table 1.1	Frontier molecular orbital energies and OFET device performance for p-type isoindigo donor-acceptor polymers.....	28
Table 1.2	Frontier molecular orbital energies and OFET device performance for isoindigo acceptor-acceptor polymers.	31
Table 1.3	Frontier molecular orbital energies and OFET device performance for donor-acceptor polymers using core-expanded isoindigo derivatives.	42
Table 2.1	Molecular weight data and decomposition temperatures of synthesized polymers..	48
Table 2.2	Optoelectronic properties obtained from UV/Vis spectroscopy and electrochemistry.	53
Table 2.3	Tabulated q values and d-spacings for lamellar peaks in the polymer GIWAXS patterns.	55
Table 2.4	OFET device performance of P1(H) and P2(F) polymers using BGBC architecture and Au source and drain electrodes.	59
Table 2.5	OFET device performance of P1(H) and P2(F) polymers using BGTC architecture and LiF/Al source and drain electrodes.	60
Table 5.1	Calibration data from the RI detector for polyethylene conventional calibration kit. The correlation coefficient for this curve was 0.994.	80
Table 5.2	Calibration data from the RI detector for polystyrene conventional calibration kit. The correlation coefficient for this curve was 0.997.....	82

Co-Authorship Statement

I performed all experimental and written work outlined in this thesis unless noted below. Organic field effect transistors were manufactured and tested by Dr. Arthur Hendsbee (Au devices) or Jenner Ngai (LiF/Al devices) at the University of Waterloo under the supervision of Professor Yuning Li. Data collection for mass spectrometry was performed by Ken Thoms and elemental analysis experiments were performed by Ken Thoms or Rosa Phuong Do. Data collection for X-ray photoelectron spectroscopy was performed by Danielle Covelli and Kyle Fransishyn. Gel permeation chromatography experiments were performed by Polyanlytik in London, Ontario. The bisisoindigo-terthiophene polymer used in Chapter 3 for testing the post-polymerization functionalization was synthesized by Chase Radford.

List of Symbols and Abbreviations

ε	Dielectric permittivity
ε_0	Permittivity of a vacuum
μ	Charge carrier mobility
μ_{lin}	Charge carrier mobility within the OFET linear regime
μ_{sat}	Charge carrier mobility within the OFET saturation regime
$\bar{\mu}$	Electrochemical potential
Φ	Work function
ϕ	Galvani potential
BII-3T	Bisindigo-terthiophene
BGBC	Bottom-gate bottom-contact
BGTC	Bottom-gate top-contact
C	Capacitance of OFET dielectric layer
D	Dispersity
d	Thickness of dielectric layer
DFT	Density functional theory
DHAP	Direct-heteroarylation polymerization
dppp	1,3-Bis(diphenylphosphino)propane
E	Electric field strength
e	Fundamental charge of an electron
EA	Electron affinity
E_g	Electronic bandgap
$E_{g,\text{opt}}$	Optical bandgap
Fc/Fc ⁺	Ferrocene/ferrocenium redox couple
GIWAXS	Grazing incidence wide angle X-ray scattering
HOMO	Highest occupied molecular orbital
I_D	OFET drain current
$I_{\text{on/off}}$	OFET current on/off ratio
IP	Ionization potential
J	Current density
k	Dielectric constant

L	OFET semiconductive channel length
LDA	Lithium diisopropylamide
LUMO	Lowest unoccupied molecular orbital
m -CPBA	<i>Meta</i> -chloroperoxybenzoic acid
\bar{M}_n	Number average molecular weight
\bar{M}_w	Weight average molecular weight
MISFET	Metal-insulator-semiconductor field effect transistor
n -BuLi	<i>n</i> -butyllithium
OFETs	Organic field effect transistors
OPVs	Organic photovoltaics
P3HT	Poly(3-hexylthiophene)
PMMA	Poly(methyl methacrylate)
S	OFET subthreshold swing
SCLC	Space charge limited current
TGBC	Top-gate bottom-contact
TGTC	Top-gate top-contact
TMEDA	<i>N,N,N',N'</i> -Tetramethylethylenediamine
V_D	Drain potential
V_G	Gate potential
V_T	Threshold voltage
W	OFET semiconductor channel width
w_i	Weight fraction
XPS	X-ray photoelectron spectroscopy

Chapter 1 – Introduction

1.1 Organic Semiconductors

The significance of conjugated polymers is highlighted by the awarding of the 2000 Nobel prize to Alan Heeger, Alan MacDiarmid, and Hideki Shirakawa for their discovery of conductivity in doped poly(acetylene) films.¹ This observation led to polymers being viewed not just as insulators with favorable mechanical properties, but as materials that could be used in a variety of novel applications in organic electronics. Interest in conjugated polymers is driven by the potential to combine the electronic properties of inorganic semiconductors with the mechanical flexibility and processability of organic polymers, leading to inexpensive and lightweight electronic devices. Conjugated polymers have garnered interest in organic photovoltaics due to the growing need to develop renewable and carbon-neutral energy sources,^{2,3} in organic light emitting diodes to develop new electronic displays, and in organic field effect transistors as circuit switching elements in consumer electronics and chemical sensors.^{4,5} Additionally, the recent development of the internet of things has led to the desire for electronic devices in many everyday items which can be made possible by the versatility of organic electronic devices.⁶

1.1.1 Band Theory and Electronic Conduction in Organic Semiconductors

Due to the localized nature of electrons in the σ -bonds that make up most of organic molecules, these materials tend to be insulating. Additionally, the energy difference between the highest occupied molecular orbital (HOMO) and the lowest unoccupied molecular orbital (LUMO) in these materials is quite high. This difference in energy, termed the electronic bandgap (E_g) for a molecule or material, is lower in materials containing π -bonds. In molecules with extensive conjugation of alternating single and double bonds, this leads to a further reduction in the HOMO – LUMO energy, which eventually leads to a bandgap typical of a semiconductor, and significant delocalization of the π electrons. Poly(acetylene) represents a useful model for this as it is the structurally simplest conjugated polymer. The decrease in bandgap with increasing conjugation can be seen in a comparison of the molecular orbital diagram of poly(acetylene) to smaller conjugated structural analogues, shown in Figure 1.1.

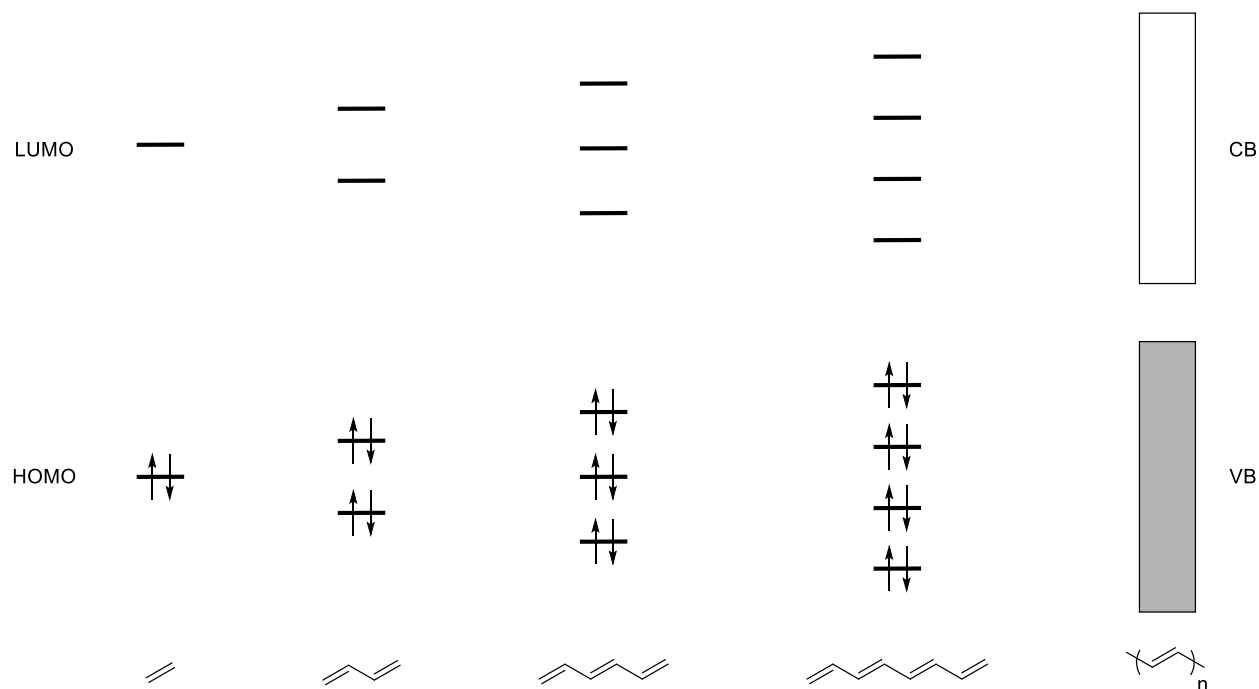


Figure 1.1 Molecular orbital energy level diagrams of conjugated oligomers extending towards poly(acetylene) and its band structure.

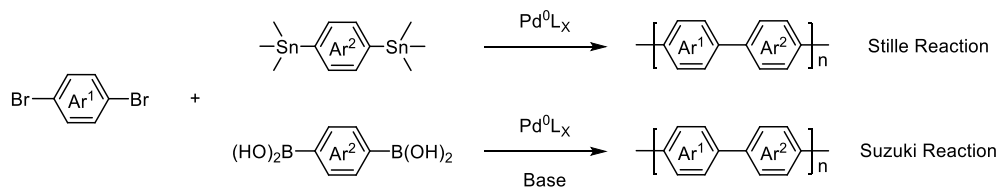
For each π bond that is added to the conjugation length another pair of π (bonding) and π^* (anti-bonding) orbitals are added to the system. As the number of these bonds increase the energy spacing between the π orbitals decreases, eventually leading to a continuum of states in a polymer of infinite length, resulting in an electronic structure similar to an inorganic valence band. Similarly, at an infinite chain length the π^* orbitals can be thought to combine into a conduction band. This allows the electronic structure of conjugated polymers to theoretically mimic that of inorganic semiconductors resulting in semiconducting conjugated polymers. There are however some important differences between organic and inorganic semiconductors and their electrical properties. In inorganic materials, holes and electrons can move freely within the valence and conduction bands, respectively, due to the repeating three-dimensional structure of the semiconductor. Organic materials have frontier molecular orbitals that are more localized, limiting the freedom of charge carriers. Additionally, polymeric semiconductors in practice have an effective conjugation length that is less than its total conjugated chain length due to twisting of the polymer along its backbone or defects in solid state molecular packing. This disrupts the coplanarity of π orbitals and further localizes the polymer's electronic states. As a result, the degree of intermolecular order between polymer chains strongly affects charge transport properties in

conjugated polymers,⁷ as the localized orbitals on different polymer chains must overlap to allow charge hopping. Structural disorder in conjugated polymers results in a range of film morphologies from polycrystalline to amorphous. In these disordered systems electronic states become increasingly localized in more disordered arrangements, resulting in significant deviation from band transport as observed in inorganic semiconductors.⁸ Instead charge transport in conjugated polymers is either through hopping transport or the multiple trapping and release model depending on the degree of localization of the electronic states.⁹ Significant localization requires charges to move by hopping between localized states along and between polymer chains with the rate of hopping depending on the spatial and energetic distance between the states.⁸ In systems with some localized and some extended electronic states charge carriers are mostly trapped in localized states until becoming promoted into a higher energy extended state where they can move more freely until falling into another localized trap state.⁸

1.2 Chemistry of Conjugated Polymers

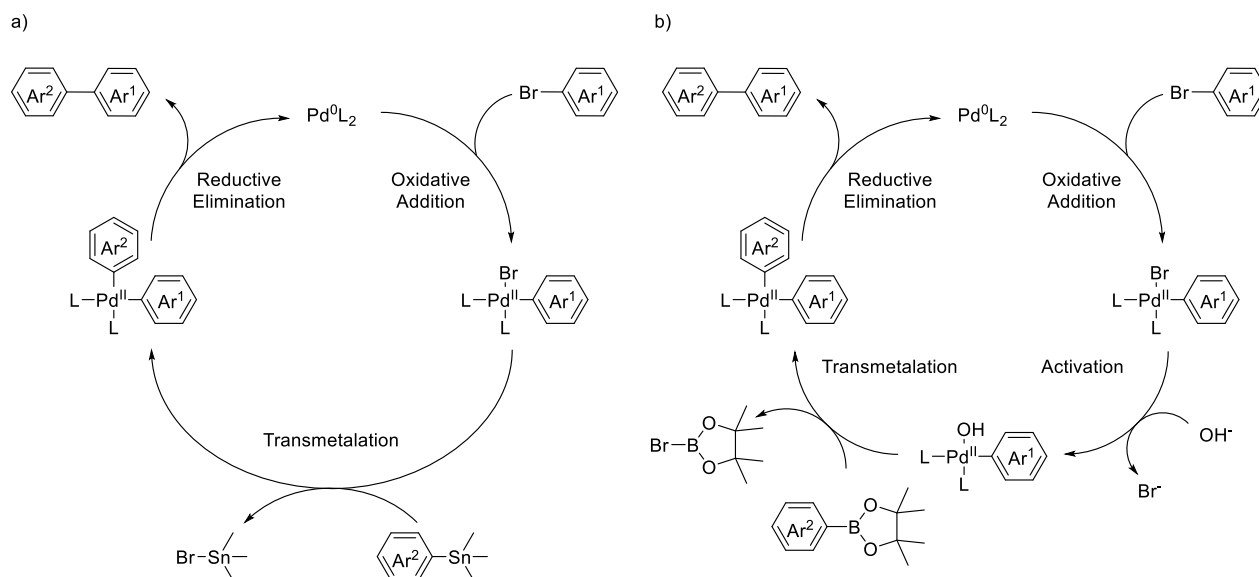
1.2.1 Synthesis of Conjugated Polymers

The methods available for the synthesis of conjugated polymers have developed significantly over time. Some methodologies that have historical significance include the Ziegler-Natta reaction to produce trans poly(acetylene) (the first conductive polymer),¹⁰ ring-opening metathesis polymerization to produce soluble polyacetylenes (which allowed solution processing),¹¹ and the Grignard metathesis reaction for producing regioregular poly(3-hexylthiophene) (P3HT),¹² (a benchmark hole conducting polymer in organic electronics). Currently, researchers typically use a palladium or nickel catalysed cross coupling reaction to synthesize conjugated polymers by reacting an aromatic dihalide with another difunctionalized aromatic unit to form new carbon-carbon bonds and create alternating copolymers. While there are several different cross-coupling reactions available including the Kumada, Heck, Sonogashira, and Negishi reactions,¹³ the Stille and Suzuki reactions are used most commonly for their reliability in making high molecular weight polymers and their broad functional group tolerance. General schemes for the Stille and Suzuki reactions are shown below (Scheme 1.1).



Scheme 1.1 General schemes of the Stille and Suzuki reaction for the synthesis of conjugated alternating copolymers. Pd⁰L_x represents a palladium(0) catalyst with an appropriate number of L-type ligands, which are generally triaryl phosphines.

Both reactions couple an aryl bromide or iodide electrophile with a nucleophile in the presence of a palladium(0) catalyst. The Stille reaction uses either a trimethyl or tributyl tin substituted aryl group as the nucleophile, while the Suzuki reaction uses either a boronic acid or a boronic ester functionalized aryl group. Mechanistically these two reactions are quite similar in that they follow an oxidative addition, transmetalation, reductive elimination catalytic sequence common to many palladium catalyzed reactions. Due to the difference in reactivity of the required nucleophile, the transmetalation in the Suzuki reaction requires the addition of a base or other additive in an activating step, while the Stille reaction does not. The catalytic cycles for each reaction are shown below in Scheme 1.2 with monosubstituted substrates for simplicity.



Scheme 1.2 a) Catalytic cycle mechanism for the Stille reaction.¹⁴ b) Catalytic cycle mechanism for the Suzuki reaction.^{15,16}

The Stille reaction can be thought of as starting from palladium(0) with two L-type ligands, typically phosphines.¹⁴ From there oxidative addition of the aryl halide at the C-Br bond leads to a

square planar palladium(II) intermediate. Transmetallation then abstracts the coordinated halide from the palladium complex and replaces it with the second aryl group. Finally, reductive elimination back to the original palladium(0) species completes the catalytic cycle and produces the desired carbon-carbon bond between the two aryl groups. In the Suzuki reaction these steps work in the same way, however there is one additional step prior to transmetallation. The role of the added base has been studied extensively and while a universal consensus has not yet been reached, the most commonly used explanation is shown above;¹⁶ the base displaces the halide ligand creating a second palladium(II) intermediate. The hydroxide ligand can then act as a Lewis base towards the Lewis acidic boron reagent allowing association of the boron reagent with the palladium complex. From there transmetallation can occur followed by reductive elimination to produce the coupling product.

While these reactions are reliable for the synthesis of conjugated polymers, they do have some drawbacks. In the case of the Suzuki reaction the requirement of base limits its potential scope of coupling partners to those that can tolerate basic reaction conditions. While there are some examples of alternative strategies that do not require an added base,^{17,18} these may not be universally viable. Both the Stille and Suzuki reactions also produce a byproduct through transmetallation in a stoichiometric amount. In the case of the Stille reaction, this production of trialkyltin halides is very problematic due to its high toxicity. This necessitates careful removal of organotin byproducts and greatly limits the potential for scale up of these reactions to being industrially relevant.¹⁴ Recently the development of direct-heteroarylation polymerization (DHAP) has allowed for polymers to be synthesized without these byproducts by using C-H bond activation of the nucleophilic coupling partner, removing the need for boron or tin reagents entirely.^{19–22} While this methodology represents a significant step forward in terms of green chemistry and atom-economy, it also leads to complications due to regioselectivity issues towards the desired C-H bond, leading to defects and branching within the polymers.²³ Also the requirement of base in DHAP limits its substrate scope similar to the Suzuki reaction. Another undesirable characteristic of the Stille, Suzuki, and DHAP reactions are the requirement of an expensive palladium catalyst. Recently the aldol condensation reaction has been used to synthesize polymers without the use of palladium or other transition metal catalysts, with water produced as the main by-product.^{24–26} This also helps to make polymers that are free of any transition metal impurities which are known to create trap states in polymer films used in electronic devices. While this is a much greener

alternative to other methods, the functional group requirements for the aldol condensation reaction likely prevents it from being a universal strategy for synthesis of conjugated polymers.

The above methods are all examples of step-growth polymerizations, rather than chain-growth polymerization.¹³ In step-growth reactions monomers can react with a growing polymer chain, or with other monomers to build oligomers. This means that the reaction mechanism throughout the polymerization stays the same. Alternatively, chain-growth polymerizations require an initiation mechanism to activate some of the monomers, a propagation step to build the polymer by reacting the monomers with the growing chain and may or may not include a termination step to stop the polymerization reaction. For alternating copolymers that are synthesized using a step-growth polymerization these distinctions become important in trying to make polymers of high molecular weight.

1.2.2 Defining Polymer Molecular Weights

As a polymer sample will have chains of different lengths and therefore different molecular weights, the way in which polymer molecular weights are thought about and discussed must be different than small molecules. The simplest measure for polymer molecular weight is the number average molecular weight (\bar{M}_n) given below.¹³

$$\bar{M}_n = \frac{\sum_{i=1}^{\infty} n_i M_i}{\sum_{i=1}^{\infty} n_i} \quad \text{Equation 1.1}$$

In this equation n_i represents the number of polymer chains of a certain length and M_i is the corresponding molecular weight. The number average molecular weight can be thought of as the unweighted average molecular weight of a polymer sample, as it is determined by dividing the total mass of polymer in the sample by the number of polymer chains. To describe the spread of different molecular weights within a sample the weight fraction (w_i) of each size of oligomer must first be defined.

$$w_i = \frac{n_i M_i}{\sum_{i=1}^{\infty} n_i M_i} \quad \text{Equation 1.2}$$

Using this concept, we can then define the weight average molecular weight (\bar{M}_w).

$$\bar{M}_w = \sum_{i=1}^{\infty} w_i M_i \quad \text{Equation 1.3}$$

Equation 1.2 and Equation 1.3 can then be combined to give a second definition for the weight average molecular weight (\bar{M}_w).

$$\bar{M}_w = \frac{\sum_{i=1}^{\infty} n_i M_i^2}{\sum_{i=1}^{\infty} n_i M_i} \quad \text{Equation 1.4}$$

This relation shows that the weight average molecular weight becomes more strongly weighted towards the larger molecular weight polymers due to the M_i^2 term in the numerator. As a result, the weight average molecular weight of a sample is always larger than the number average molecular weight. The most common measure for the spread of molecular weights within a sample is given by the dispersity (\bar{D}), which is the ratio of these two measures.

$$\bar{D} = \frac{\bar{M}_w}{\bar{M}_n} \quad \text{Equation 1.5}$$

The dispersity of a polymer made using a step-growth method will typically range between 1 and 2, and depends on the extent of the reaction, which is displayed below as a function of time.

$$p(t) = \frac{n_0 - n_t}{n_0} \quad \text{Equation 1.6}$$

Here $p(t)$ is the extent of the reaction as a function of time, n_0 is the number of unreacted monomers at the start of the reaction and n_t is the number of unreacted monomers at a time after the reaction has started. The extent of the reaction will start at zero and increase towards one as the reaction progresses. The dispersity of a polymer sample for a polycondensation step-growth polymer is related to the extent of the reaction by Equation 1.7 below.

$$\bar{D} = 1 + p \quad \text{Equation 1.7}$$

This means that most step-growth polymers should theoretically have a dispersity near two. Polymers with a dispersity below 1.2 are termed uniform (or monodisperse in older literature) while polymers with a dispersity greater than 1.5 are termed non-uniform (or polydisperse). Reaction mechanisms competing with the polymerization (homo-coupling, debromination, destannylation, etc.) can lead to premature termination of the polymerization reaction and produce materials with dispersities greater than 2.

As the extent of the reaction increases, so will the degree of polymerization, which is expressed as a function of time as $X_n(t)$.

$$X_n(t) = \frac{n_0}{n_t} \quad \text{Equation 1.8}$$

Combining Equation 1.6 and Equation 1.7 produces Carothers' equation which relates the degree of polymerization to the extent of the reaction.

$$X_n(t) = \frac{1}{1 - p(t)} \quad \text{Equation 1.9}$$

To achieve a high degree of polymerization as required for high molecular weight polymers, Carothers' equation shows that the extent of reaction $p(t)$ needs to be as close to one as possible. This means that equimolar amounts of each monomer are required to prevent any unreacted monomer from remaining in the reaction mixture, limiting the degree of polymerization. This also means that each monomer must be prepared as pure as possible such that the monomer ratio can be accurately calculated and properly weighed out in performing a polymerization reaction.

1.3 Organic Field Effect Transistors

Organic field effect transistors (OFETs) are a more recently developed version of the metal-insulator-semiconductor field effect transistor (MISFET), a key component of computer processors and memory devices, communication chips, backplanes for electronic displays and many other electronic devices.²⁷ These transistors are used in circuits to either amplify an electrical signal or to turn a current on or off. In an OFET, the semiconductor is an organic material rather than the typical single-crystalline silicon in most MISFETs. Changing the semiconductor to organic materials can allow for a significant decrease in the manufacturing costs of these devices, as the single-crystalline silicon wafers used are produced by forming large single crystals from molten

silicon in a very energy intensive and costly process.^{27,28} In contrast, organic semiconductors can be processed from solution, greatly simplifying production. The flexibility of organic thin films also creates the potential for flexible electronic devices such as bendable displays,²⁹ medical sensing devices attached to the skin or textiles,⁶ or electronics printed on paper.³⁰

1.3.1 Architecture and Operation of OFETs

Organic field effect transistor devices are made using a layered architecture including a gate electrode, a resistive dielectric layer, the organic semiconducting layer, and the source and drain electrodes to supply and collect charge carriers.^{4,27,31} The gate electrode is capacitively coupled to the semiconducting layer and controls when charge carriers are present in the channel. In the four typical geometries for OFETs the gate electrode and the semiconducting layer are separated by the dielectric, but the positions of the source and drain electrodes within the organic layer and the layering of the semiconductor, dielectric, and gate can vary, as shown in Figure 1.2.

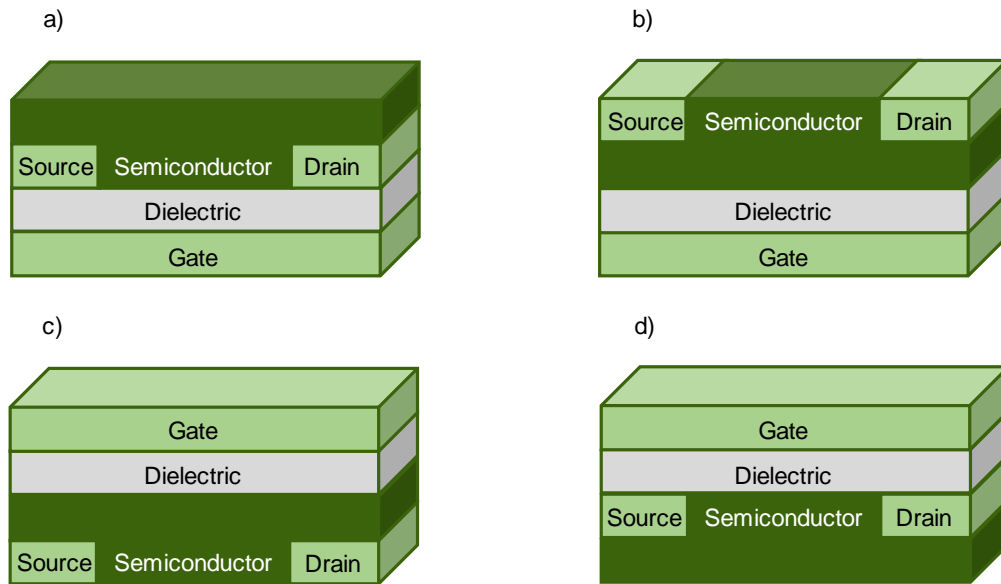


Figure 1.2 Layered device architectures for a) bottom-gate bottom-contact (BGBC) b) bottom-gate top-contact (BGTC) c) top-gate bottom-contact (TGBC) and d) top-gate top-contact (TGTC) organic field effect transistors, where the device substrate is on the bottom in each case.

To understand some of the important differences between these architectures it is useful to understand the operation of the devices. All these architectures can operate for the conduction of holes (p-channel) or electrons (n-channel) by controlling the sign of the applied voltages. As the operating principles are the same only n-channel electron conducting operation will be described.

The application of a positive potential to the gate electrode relative to the source electrode (gate potential, V_G) greater than the threshold voltage (V_T , detailed discussion to follow) causes electrons to be injected into the semiconducting layer and then accumulate at the interface of the semiconductor and the dielectric, forming the conductive channel.^{27,31} The source electrode is held at constant potential throughout operation while a second positive potential is applied to the drain electrode (drain potential, V_D). This potential gradient along the conductive channel causes the electrons in the channel to move from the source electrode to the drain electrode generating current flow.

Injection of charge carriers because of the applied gate potential relies on changing the energy of the charge carriers relative to the HOMO and LUMO levels of the semiconductor. This principle is displayed below in Figure 1.3 for the operation of an n-channel device. Important parameters for this process are the metal work function and electrochemical potential, as well as the ionization potential and electron affinity of the semiconductor layer. The electrochemical potential ($\bar{\mu}$) of a metal is the energy required to remove an electron to a reference level, a distance far enough from the metal surface that the energy of an electron is zero. The electrochemical potential is the sum of the work function (Φ , energy to remove electron to position just outside the metal) and the Galvani potential (ϕ , the work required to move an electron to the reference level against the electric field produced by the surface dipoles and charge). The energy to remove an electron from its ground state to the reference level is given by its ionization potential (IP), while the energy to add an electron from reference level to a ground state molecule is given as the electron affinity (EA).

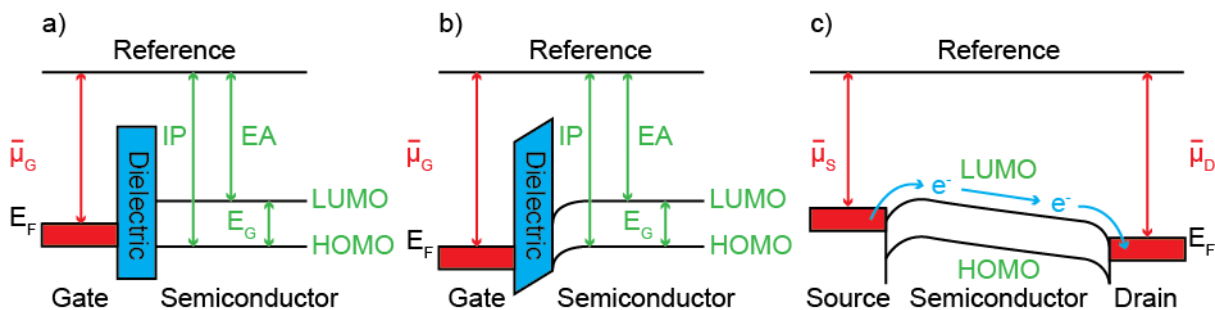


Figure 1.3 Energy level diagrams showing operation of n-channel OFETs. a) Energy levels of the gate electrode and the semiconductor separated by the gate dielectric with no applied gate potential ($V_G = 0$). b) Application of a positive gate potential ($V_G > 0$) resulting in a lowering of the HOMO and LUMO energy levels near the gate dielectric. c) Sufficient lowering of the LUMO energy level

because of applied V_G allows electron injection into the LUMO and a positive drain potential ($V_D > 0$) causes charges to move along the channel to be collected as the drain current.

In the absence of any applied potentials the energy level diagram will exist as in Figure 1.3 a). Application of the positive gate potential lowers the Fermi energy of the gate electrode relative to the rest of the system by increasing the Galvani potential. While the position of the gate Fermi energy relative to the frontier molecular orbitals does not impact charge injection, the accumulated positive charge with a positive gate potential results in a lowering of the energies of the HOMO and LUMO near the semiconductor-dielectric interface (Figure 1.3 b). With large enough applied gate potential, the LUMO of the semiconductor is lowered to the point where electrons can be injected from the source electrode into the semiconductor (Figure 1.3 c). The gate potential required for this charge injection to occur is referred to as the threshold voltage (V_T). As the semiconductor LUMO energy has been lowered in the region near the dielectric due to the gate potential, injected electrons accumulate at this interface forming a capacitive layer to oppose the charge in the gate electrode. It is typical that both the source and drain electrodes are the same material, and therefore have the same Fermi energy. This means that there is no inherent bias towards the direction of charge flow until a drain potential is applied, shown in Figure 1.3 c), leading to the collection of the source-drain current.

One difference between the different types of OFET device architectures is the distance between the source/drain electrodes and the dielectric layer. The bottom-gate bottom-contact and top-gate top-contact architectures (Figure 1.2 a, d) have direct contact between the source and drain electrodes with the gate dielectric. As a result, charge injection occurs predominantly from the vertical face of the source electrode and these charges have a small distance to travel before reaching the accumulation region in the semiconductor channel.³² In the case of bottom-gate top-contact and top-gate bottom-contact architectures (Figure 1.2 b, c) the semiconductor separates the source from the dielectric. This allows charges to be injected more easily from both the vertical and horizontal faces of the source, potentially leading to increased currents.³² Another important consideration in selecting a device architecture is the position of the gate electrode and dielectric. Having these two layers on the bottom as in BGBC and BGTC (Figure 1.2 a, b) makes device manufacturing much simpler.²⁷ The typical materials used for these layers are a heavily doped silicon substrate used for the gate electrode followed by a thermally grown layer of SiO_2 for the dielectric layer,³³ however other materials such as polymeric dielectrics and plastic substrates can

be used to make flexible OFETs.^{34–36} While having the gate and dielectric deposited after the organic semiconductor is more challenging to manufacture it can give increased performance, particularly in electron conducting materials that are not stable to air and moisture. In these devices the gate and dielectric act as encapsulation layers and can help to prevent the degradation of the semiconducting layer due to atmospheric conditions.⁴ The ordering of the deposition of the source and drain electrodes relative to the semiconductor can also have an effect on device performance. The most commonly used metals for source and drain contacts are gold and aluminium.³³ The TGBC architecture (Figure 1.2 c) requires the semiconducting layer to be deposited before the source and drain electrodes are applied by thermal evaporation. This gives good contact between the semiconductor and electrodes resulting in lower contact resistances but can damage the semiconductor during the electrode deposition. Also using shadow masks to control the deposition of the electrodes during thermal evaporation gives limited control over the channel length, an important variable in developing OFETs which can operate at high frequencies.^{37,38} In BGBC devices (Figure 1.2 a) the source and drain electrodes are deposited first using photolithography techniques, resulting in consistent and small channel lengths.³³ The organic semiconductor layer is then deposited from solution, giving higher contact resistance between the electrodes and the semiconductor, but overall easier device manufacturing. With all these factors needing to be considered, selecting the ideal device architecture is challenging; however, the BGBC architecture is often chosen for prototype testing of new semiconductor materials. This is because the devices can be easily manufactured as the organic semiconductor layer is the last to be deposited. As a drawback these devices typically show poorer performance relative to other architectures.

1.3.2 Figures of Merit for OFET Devices

To this point in the discussion of organic field effect transistors there have been frequent references to the performance of the devices, but how device performance has been measured and defined was not mentioned. This section will cover the various figures of merit used to compare different OFET materials and devices, along with their theoretical basis and how they are determined experimentally.

The most common figure of merit used for benchmarking organic semiconductors as OFET materials is the charge carrier mobility (μ), which is the charge carrier average drift velocity per unit applied electric field. The charge carrier mobility is thought of as an intrinsic property of a

material but can be determined in OFETs in two ways, which may give different results. Variations in processing conditions, material purity and film quality can also lead to different extracted charge carrier mobilities. The current flowing through the OFET channel can be in either the linear or the saturation regime based on the magnitudes of V_G , V_D and V_T . These two current regimes have different equations relating the drain current to the charge carrier mobility and the charge carrier mobilities are designated as μ_{sat} (saturation regime) or μ_{lin} (linear regime).³¹ The linear current regime occurs when the difference between the gate and threshold voltages is greater than the drain voltage ($V_G - V_T > V_D$), while the saturation regime is when the drain potential is greater than the difference in gate and threshold voltages ($V_G - V_T < V_D$). The threshold voltage is a separate figure of merit for OFETs which will be discussed later, but for now can be thought of as the required turn-on gate voltage to induce charge carriers into the semiconducting channel. The relations between the charge carrier mobilities and the drain current in the linear and saturation regimes are displayed below in Equation 1.10 and Equation 1.11 respectively.

$$I_D = \frac{W}{L} \mu_{\text{lin}} C \left[(V_G - V_T) V_D - \frac{V_D^2}{2} \right] \quad \text{Equation 1.10}$$

$$I_D = \frac{W}{2L} \mu_{\text{sat}} C (V_G - V_T)^2 \quad \text{Equation 1.11}$$

In these equations L and W represent the length and width of the semiconductor channel as labeled in Figure 1.4, C is the capacitance of the dielectric layer, and I_D is the measured drain current.

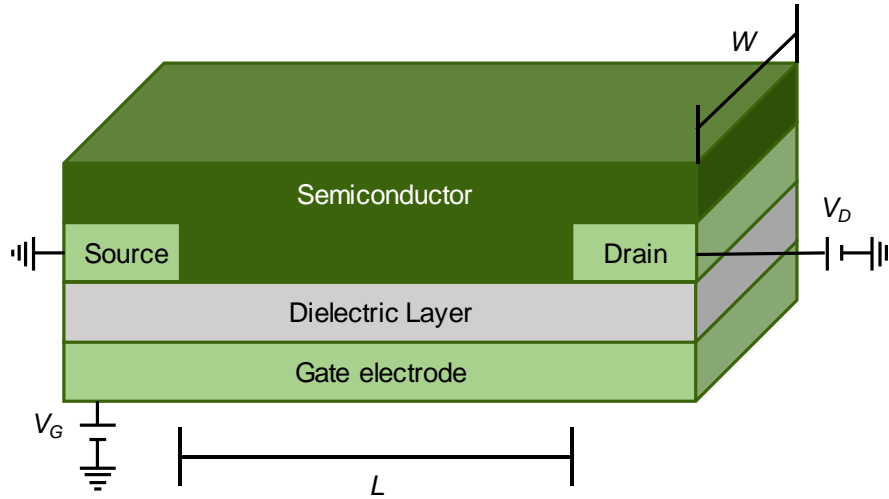


Figure 1.4 BGBC OFET with labeled channel length and width. Positive potentials applied to the gate and drain electrodes relative to the grounded source electrode as required for n-channel device operation are also shown.

To arrive at the relationships for the charge carrier mobilities in the linear and saturation regimes, it is useful to consider the charge carrier concentration profile along the channel length as a function of V_G and V_D , shown in Figure 1.5.

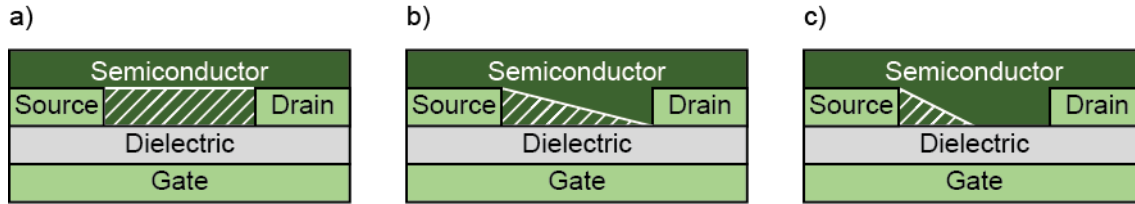


Figure 1.5 BGBC OFET with region of significant charge carrier concentration highlighted with white stripes throughout device operation. Carrier concentrations displayed a) with $V_G > V_T$ and $V_D = 0$ b) $V_G - V_T \cong V_D$ (near the change from the linear to the saturation regime) and c) $V_G - V_T < V_D$ (the saturation regime).

In the case of an applied gate potential greater than the threshold potential as in Figure 1.5 a), charges are injected into the semiconductor channel and form a capacitive layer at the semiconductor-dielectric interface, resulting in a constant charge carrier concentration along the channel. As a positive potential is applied to the drain electrode (in an n-channel device) electrons are extracted by the electrode, depleting the charge carrier concentration near the drain electrode. This results in a linear gradient of charge carriers as in Figure 1.5 b) going from high concentration near the source to low concentration near the drain. The linear regime exists between the conditions shown in Figure 1.5 a) and b) where there is a linear gradient of charge carrier concentration

spanning the channel length. The amount of charge at a position along the channel $q(x)$ in terms of areal density (C/cm^2) is given by Equation 1.12 and depends on the voltage difference between the gate and that position x along the channel.

$$q(x) = n(x)et = C(V_G - V(x)) \quad \text{Equation 1.12}$$

Here $n(x)$ is the number density of charge carriers within the channel at a particular position along the channel, e is the fundamental charge of an electron, t is the channel thickness and C is the capacitance of the dielectric in F/cm^2 . To account for the non-zero turn on voltages in OFETs the threshold voltage is subtracted from the applied gate potential to more accurately represent the charge along the channel.

$$q(x) = n(x)et = C(V_G - V_T - V(x)) \quad \text{Equation 1.13}$$

This relation gives a constant amount of charge along the channel, as shown in Figure 1.5 a). In the case of an applied drain voltage as in Figure 1.5 b) we can use this as a starting point for determining the average amount of charge at any point along the channel while in the linear regime, given in Equation 1.14

$$q(x)_{\text{avg}} = C \left(V_G - V_T - \frac{V_D}{2} \right) \quad \text{Equation 1.14}$$

This will give the amount of charge at the halfway point along the channel length. Combining this equation with Ohm's law allows for the derivation of a relation between the drain current and the charge carrier mobility. Ohm's law can be written in terms of current density (J) and electric field (E), given below in Equation 1.15, and then rewritten in terms of the drain current, drain potential and geometry of the channel in Equation 1.16.

$$J = \sigma E \quad \text{Equation 1.15}$$

$$\frac{I_D}{tW} = \frac{\sigma V_D}{L} \quad \text{Equation 1.16}$$

Using the definition of conductivity, we can substitute σ for $n(x)e\mu$, and then rearranging this arrive at Equation 1.17.

$$I_D = \frac{W}{L} \mu(n(x)et)V_D \quad \text{Equation 1.17}$$

Equation 1.17 can be combined with Equation 1.14 to give Equation 1.18, which is then rearranged to give the current law for the linear regime as given above in Equation 1.10.

$$I_D = \frac{W}{L} \mu_{\text{lin}} C (V_G - V_T - \frac{V_D}{2}) V_D \quad \text{Equation 1.18}$$

$$I_D = \frac{W}{L} \mu_{\text{lin}} C \left[(V_G - V_T) V_D - \frac{V_D^2}{2} \right] \quad \text{Equation 1.10}$$

This relation for the linear regime will apply given that $V_G - V_T > V_D$, however as the drain potential is increased, more and more charge carriers will be swept out of the channel and collected as the drain current. When the drain potential becomes approximately equal to $V_G - V_T$ the area nearest to the drain electrode will be completely depleted of charge carriers, as depicted in Figure 1.5 b). This is referred to where the channel becomes pinched and represents the transition between the linear regime and the saturation regime. If the drain potential is increased further, a larger area near the drain electrode will be depleted of charge, pushing the pinch point along the channel towards the source, depicted in Figure 1.5 c). This changes the behaviour of charge carriers in the channel; carriers are injected at the source electrode and travel towards the drain until reaching the pinch point, where they are injected into a space-charge region before collection at the drain electrode.³⁹ As a result, there is no increase in the drain current as the drain potential is increased. Because the drain current is constant for all $V_D \geq V_G - V_T$ we can substitute $V_G - V_T$ in place of V_D in Equation 1.10 to reach the current law for the saturation regime, previously given as Equation 1.11.

$$I_D = \frac{W}{2L} \mu_{\text{sat}} C (V_G - V_T)^2 \quad \text{Equation 1.11}$$

The performance of OFET devices is usually measured by monitoring the drain current as a function of the gate or drain potential while the other is held constant. This data is plotted either as an output curve (I_D vs. V_D with constant V_G) or a transfer curve (I_D vs. V_G with constant V_D). Examples of each is shown below in Figure 1.6.⁴⁰

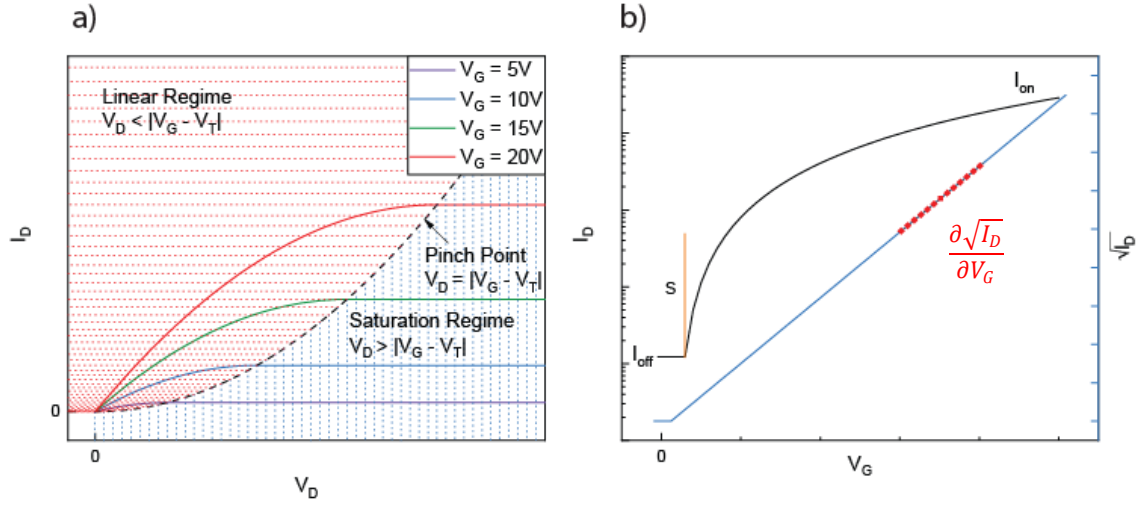


Figure 1.6 a) Output curves with varying gate potentials showing the linear (red dots) and saturation (blue dots) regimes. The intersection between the two regimes gives the pinch point in dashed black lines. b) Transfer curve (black line) for the saturation regime current plotted on a logarithmic scale. The square root of the current as a function of V_G is shown as a blue line on a linear scale, whose slope (in red) is usually used to determine μ_{sat} . The slope of the orange line is used to determine the sub-threshold swing, a measure of how quickly and easily the device turns from off to on. Adapted from Lamport, Z. A.; Haneef, H. F.; Anand, S.; Waldrip, M.; Jurchescu, O. D. Tutorial: Organic Field-Effect Transistors: Materials, Structure and Operation. *J. Appl. Phys.* **2018**, 124, 071101. with the permission of AIP Publishing.

In the output curve the drain current increases as a function of the drain potential in the linear regime until the pinch point, where the current remains constant throughout the saturation regime even with increasing drain potential. Typically, a range of gate potentials are measured and plotted, with increasing gate potentials giving rise to increased drain currents. Transfer curves showing the drain current as a function of gate potential with constant drain potential are plotted on a logarithmic scale and are often used to measure charge carrier mobility. To determine the charge carrier mobility in the saturation regime first the square root of both sides of Equation 1.11 are taken, then the resulting equation is differentiated with respect to the gate voltage. This equation is then squared on both sides and rearranged to isolate for the charge carrier mobility μ_{sat} .

$$\mu_{\text{sat}} = \frac{2L}{CW} \left(\frac{\partial \sqrt{I_D}}{\partial V_G} \right)^2 \quad \text{Equation 1.19}$$

A similar relation could be determined for the charge carrier mobility in the linear regime as well, however μ_{sat} and μ_{lin} should theoretically give the same result. Experimentally it is found that the

charge carrier mobility in the saturation regime is often larger, so only μ_{sat} is reported. This difference in measured mobility results from contact resistance between the source/drain electrodes and the semiconductor. Contact resistance at the electrodes will reduce the effective drain potential, which becomes problematic in the linear regime where the drain potential is already small relative to the saturation regime.⁴⁰ Measurement of the charge carrier mobility in the saturation regime mitigates the risk for underestimation. Another consideration relating to charge carrier mobility and contact resistance in OFETs is that in cases where devices have very large contact resistances as a result of mismatched electrode work functions and semiconductor orbital energies, the obtained square root of the transfer curve (the blue line in Figure 1.6 b) may become kinked, giving two different slope values that can be used.²⁹ Extracting the charge carrier mobility from the larger of the two slopes can lead to overestimation of the charge carrier mobility, as has become somewhat problematic in the OFET literature.²⁹

Despite the charge carrier mobility being thought of as an intrinsic property for organic materials, the way that it is determined experimentally can impact the measured charge carrier mobility. It is well known that many organic conjugated polymers form ordered thin films when deposited onto a substrate and these films can have preferential orientation relative to the substrate. An example of this is P3HT, which exhibits either predominantly edge-on or face-on orientation relative to the substrate depending on the conditions of deposition.⁴¹

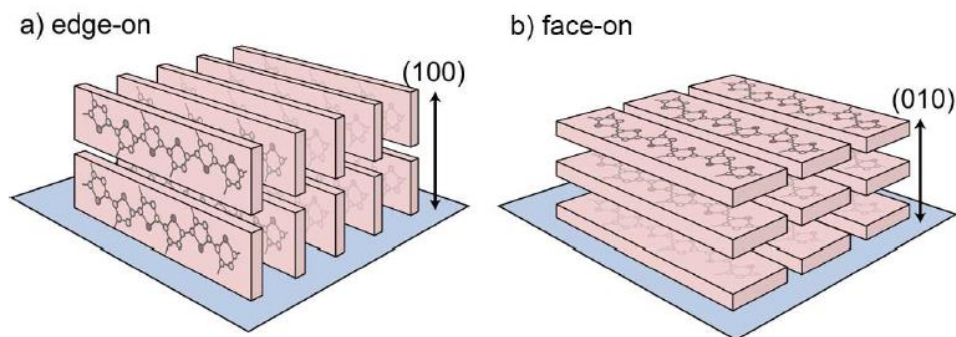


Figure 1.7 Ordering of P3HT in thin films in a) edge-on or b) face-on molecular packing arrangements. Figure adapted with permission from Gargi, D.; Kline, R. J.; DeLongchamp, D. M.; Fischer, D. A.; Toney, M. F.; O'Connor, B. T. *J. Phys. Chem. C* **2013**, *117*, 17421–17428. Copyright 2013 American Chemical Society.

It is known that the degree and direction of π -stacking in organic semiconductors impacts the resulting charge carrier mobility.⁴² Thin films of organic semiconductors that are preferentially ordered either face-on or edge-on should then have different mobilities for charges carried in the same direction as the π -stacking direction compared to currents in the perpendicular direction. For OFETs, the source and drain electrodes are in the same plane and charges must move parallel to the substrate for collection as the drain current. This type of transport is favored by the edge-on orientation which has π -stacking parallel to the substrate plane. Another common way to determine charge carrier mobilities in organics is the space-charge limited current (SCLC) method. This method uses a layered device structure with the organic material in between two electrodes, where charges must be carried perpendicular to the substrate surface. The orientation of these devices results in better charge transport with organic materials that exhibit face-on orientation relative to the substrate. This means that organic semiconductors that create preferentially oriented thin films can have different charge carrier mobilities in different directions based on the orientation of the repeating structure relative to the substrate, resulting in different mobility values as determined using OFETs or SCLC devices. Additionally, this indicates the importance of determining the relative orientation of polymer films when measuring charge carrier mobilities by any method.

The threshold voltage in an OFET is another figure of merit and is thought of as the required gate voltage for passing current through the semiconducting layer. The concept of a threshold voltage was developed for MISFETs, where it was defined as the minimum gate voltage required to induce strong inversion of the charge carrier concentration in the channel.²⁷ Inversion in MISFETs is achieved by applying a potential to a doped semiconductor to first deplete the semiconductor of charge carriers, then increasing the magnitude of the potential to eventually induce charge carriers of the opposite polarity to enter the channel.³⁹ As OFETs do not operate in inversion mode this definition does not apply, however the threshold voltage is still a useful metric for performance of OFETs as it gives the gate potential required for the device to function. The first factor that contributes to V_T in n-channel OFETs is a mismatch between the work function of the source electrode and the semiconductor LUMO energy. This energy mismatch contributes to the threshold voltage as it must be compensated for before charges can be injected into the channel. Additionally, deep trap states within the channel will need to be filled before the channel will conduct charge increasing the threshold voltage, while any doping of the channel with charge carriers can reduce the threshold voltage.³¹ Experimentally the threshold voltage can be determined

by the intercept of the square-root drain current with $I_D = 0$ (see intersection of curve with flat line in blue trace in Figure 1.6 b). Devices with low threshold voltages are desirable as they allow for lower power consumption during operation.^{43,44} One strategy to lower the threshold voltage is to produce devices with dielectric layers with larger capacitance, as these will more easily induce charges into the channel. Based on the equation for capacitance given in Equation 1.20 where ϵ_0 is the permittivity of a vacuum, capacitance (C) can be increased either by using materials with a high dielectric constant (k), or by minimizing the thickness of the dielectric layer (d).

$$C = \frac{k\epsilon_0}{d} \quad \text{Equation 1.20}$$

Some literature examples of low threshold OFETs involved reducing the number of defects at the dielectric-semiconductor interface to minimize trap states,⁴⁵ using polymer dielectric materials,³⁴ or by using electrolytes as the gate to greatly reduce the effective thickness of the capacitor.⁴⁶ For the mass production of electronics based on OFETs and their consistent performance it is also critical for there to be low variation in the threshold voltage between devices, as this can cause differences in pixel brightness in OFET driven displays or limit the number of transistors that can be combined in an integrated circuit.⁴⁷

The on/off current ratio ($I_{\text{on/off}}$) is important for OFETs both in applications where they act as switches or for signal amplification. These values are determined from the maximum drain current in the saturation regime (on-state) and the minimum drain current with no applied gate potential (off-state) and are reported as 10^x , where values between 10^2 and 10^8 are typical. The on/off current ratio can be optimized by maximizing the I_{on} by using a semiconductor with a high charge carrier mobility and by minimizing I_{off} by eliminating unwanted dopants and impurities which could generate current.

The subthreshold swing (S) is determined from the inverse slope of the transfer curve (orange line in Figure 1.6 b) at the point where the device turns from off to on. The subthreshold swing is defined by Equation 1.21.

$$S = \frac{dV_G}{d(\log I_D)} \quad \text{Equation 1.21}$$

This is usually reported in either V per decade or mV per decade and is a measure of how quickly a device switches from its off state to its on state. A low value of S is more desirable and indicates a lower concentration of interfacial trap states.

1.4 Material Design of Organic Semiconductors for n-Channel OFETs

The development of electron conducting organic semiconductors has been driven by their potential in a variety of applications. As the field of organic photovoltaics moves increasingly towards using non-fullerene electron acceptors, more and more electron conducting materials are being developed.⁴⁸ In organic field effect transistors n-channel devices can be combined with p-channel devices to create logic circuits or light emitting field effect transistors.^{4,49} Despite the drive for production of these electron conducting materials their performance is still trailing that of their hole conducting counterparts. Part of the challenge in developing new electron conducting materials is their instability towards moisture and oxygen. It has been shown both theoretically and empirically that for these materials to be stable while conducting electrons they require a LUMO energy level of approximately -4.0 eV relative to vacuum.⁵⁰⁻⁵² During n-channel device operation the semiconductor exists as an organic anion as a result of electron injection from the source electrode and a low LUMO energy helps to stabilize this anion and prevent oxidation by atmospheric water or oxygen.³¹ As a synthetic strategy, electron withdrawing groups are installed onto organic semiconductors to lower the LUMO energy level helping to stabilize these materials towards ambient conditions. This leads to the second challenge in developing electron conducting materials; there are relatively few conjugated building blocks that are electron-deficient enough and these structures tend to be difficult to synthesize. While the LUMO energy is most important for stability of electron conducting materials, the HOMO energy level also helps determine whether the material is unipolar (conducts either electrons or holes exclusively) or is ambipolar (conducts holes or electrons). A low HOMO energy level will create a large hole injection barrier from the device electrodes ensuring unipolar electron transport rather than ambipolar performance. Ambipolar materials are not as desirable in OFETs as they tend to have higher off currents and therefore lower $I_{\text{on/off}}$ ratios.

1.4.1 Donor-Acceptor Design Strategy in Organic Semiconductors

While some early conjugated polymers were homo-polymers with one type of conjugated unit within the polymer repeat unit, like P3HT for example, the donor-acceptor structure for alternating copolymers has become the most common design strategy. Donor-acceptor copolymers feature two different conjugated units, one of which is relatively electron rich (the donor) and one is relatively electron poor (the acceptor). The donor-acceptor design helps to localize frontier molecular orbitals in different regions along the polymer backbone helping charge transport, reducing the polymer's bandgap, and makes it easier to tune orbital energy levels by modifying either of the conjugated units.⁵³ The combination of molecular orbitals resulting from linking the donor and acceptor leads to the reduced bandgap as shown in Figure 1.8.

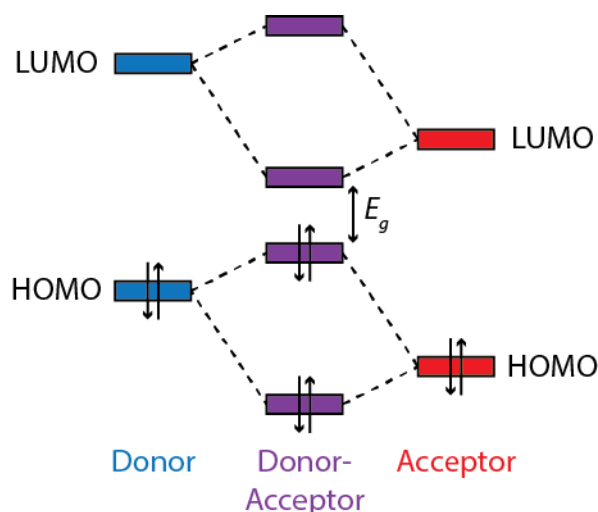


Figure 1.8 Frontier molecular orbital energy levels of an electron rich donor and electron poor acceptor, and their combination to create a donor-acceptor system.

In the donor-acceptor structure the newly formed frontier molecular orbitals retain some of the localization from the separated donor and acceptor. As the newly formed HOMO in the donor-acceptor is similar in energy to the HOMO of the donor it is typically localized mainly to the donor structure in the alternating copolymer. Similarly the donor-acceptor LUMO is close in energy to the acceptor LUMO and is typically localized to the acceptor unit.⁵³ Additionally, this localization makes tuning the frontier molecular orbital energies somewhat straightforward; modification of the donor leads to changes in the HOMO energy level while the LUMO is relatively unchanged, and modification of the acceptor changes the LUMO while the HOMO remains approximately the same.

To produce materials with a wide range of frontier molecular orbital energies chemists have developed many donors and acceptors to build into donor-acceptor conjugated polymer. Many of the donor building blocks involve thiophene either as polythiophenes or as ring fused oligomers. Acceptor building blocks usually have more electron withdrawing functional groups and heteroatoms, mainly featuring oxygen and nitrogen atoms in amides, imides or other groups. A selection of common donor and acceptor units for polymers is shown below in Chart 1.1.

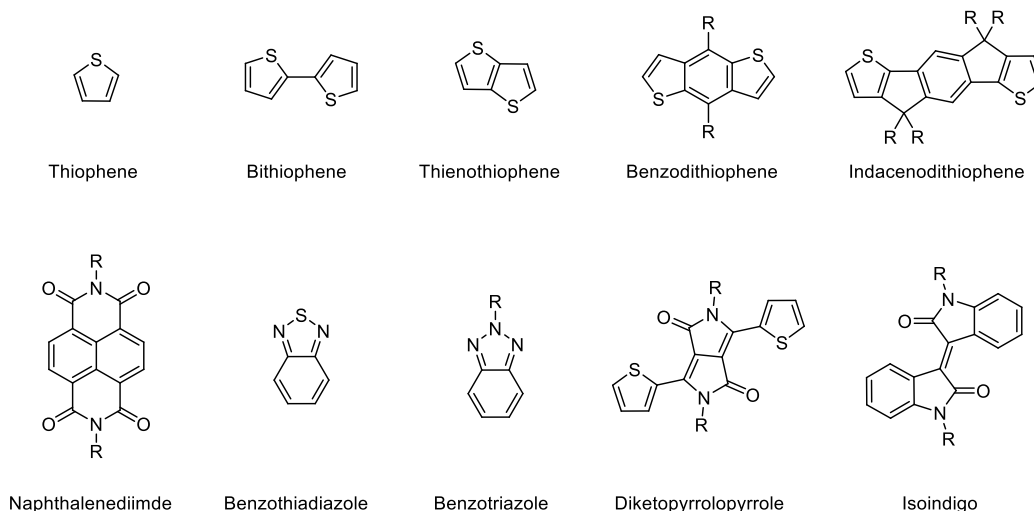


Chart 1.1 Sampling of common electron-rich donors (top row) and electron-deficient acceptors (bottom row) used in donor-acceptor conjugated polymers.

While there are a variety of different electron-deficient acceptor groups available that have been studied in many different systems, the current project of this thesis focuses mainly on isoindigo and benzothiadiazole acceptors and so the others will not be discussed in depth.

1.4.2 Isoindigo – From Dyes to Semiconductors

Indigo is one of the oldest known dyes, as it has been used in the textile industry for hundreds of years and is still used today to dye denim in blue jeans.⁵⁴ When indigo is extracted from plants it exists as a mixture of isomers with a range of colors, causing pure synthetic indigo to have a different appearance than natural indigo.⁵⁵ Isoindigo is one of these isomers that can be extracted along with indigo from the leaves of *Isatis tinctorial*.⁵⁵

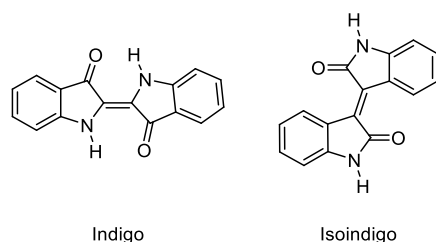
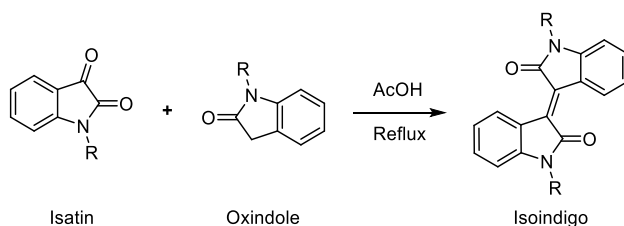


Chart 1.2 Structures of indigo and isoindigo as obtained from *Isatis tinctorial*.

Isoindigo tends to be insoluble in most organic solvents due to strong π stacking and intermolecular hydrogen bonding of the lactam hydrogens. The installation of alkyl chains on the amide nitrogen atoms does not disrupt the coplanarity of the conjugated structure, but helps solubilize the isoindigo by breaking up π stacking and preventing hydrogen bonding.⁵⁶ Synthesis of isoindigo involves an acid-catalysed aldol condensation between an isatin and an oxindole which can be performed in very high yields. This reaction produces mainly one isomer at the exocyclic carbon-carbon double bond, as the other isomer would lead to unfavorable steric clash between the C-H bonds of the aryl rings that would be put into close proximity to each other. This selectivity is one of the advantages of using isoindigo compared to indigo and its other natural isomers, which can each exist in either a *cis* or *trans* geometry.⁵⁵



Scheme 1.3 Synthesis of isoindigo via acid catalyzed aldol condensation between isatin and oxindole.

For the synthesis of organic semiconductors isoindigo is usually brominated to provide a synthetic handle for further functionalization through metal catalyzed cross coupling reactions. Bromination of isoindigo in the 6,6' positions ensures effective conjugation between the isoindigo unit and the subsequent aryl groups installed using cross-coupling reactions. This substitution position allows for a quinoidal resonance form through the isoindigo structure giving increased electron delocalization and allowing easier charge transport.⁵⁷

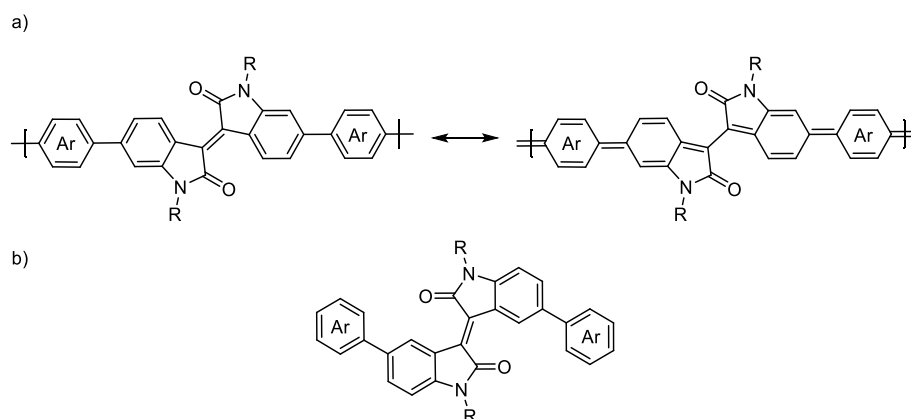


Figure 1.9 a) Isoindigo arylated in the 6,6' positions shown with its quinoidal resonance structure. b) Isoindigo arylated in the 5,5' positions, where a quinoidal resonance structure spanning the isoindigo unit is not present.

The first isoindigo based semiconductors for organic electronics was reported in 2010 by Mei et al.⁵⁸ who synthesized small molecules with donor-acceptor-donor and acceptor-donor-acceptor structures using isoindigo as the electron-deficient acceptor and a bithiophene donor unit. These materials were measured to have low LUMO energies between -3.8 and -3.9 eV in the solid state and bandgaps between 1.67 and 1.76 eV and were used to make organic solar cells. The electronic properties of these materials quickly inspired more work on isoindigo based semiconductors, including isoindigo containing polymers. The use of polymeric semiconductors rather than small molecules brings advantages of more consistent, high quality films as well as improved charge transport through polymer chains. In 2011 the first isoindigo donor-acceptor polymers were synthesized by Lei et al.⁵⁹ using thiophene and bithiophene as the donor unit. These polymers had similar frontier molecular orbital energies to those reported by Mei et al.⁵⁸ and produced p-channel OFETs with hole mobilities as high as $0.79 \text{ cm}^2 \text{ V}^{-1} \text{ s}^{-1}$ after thermal annealing. Despite both polymers (structures given in Chart 1.3) having the same 2-octyldodecyl side chains attached to the isoindigo unit the bithiophene containing polymer (P2) gave much higher molecular weights than the thiophene containing polymer (P1). This higher molecular weight was then linked to more ordered edge-on oriented films observed by grazing incidence X-ray diffraction, which was presumed to be the reason for increased hole mobility.

As a continuation of this work, Lei et al.⁶⁰ produced a series of eight additional isoindigo donor-acceptor polymers with varied thiophene-based electron rich donor units, as shown in Chart 1.3. The donor units were classified as either centrosymmetric (P2 – P7) or axisymmetric (P1, P8

– P10) and it was shown that the axisymmetric units led to deviations from linearity along the polymer backbone and disrupted molecular packing in thin films. For these reasons they observed increased hole mobility in the polymers with centrosymmetric donors, with a high of $1.06 \text{ cm}^2 \text{ V}^{-1} \text{ s}^{-1}$ in P2. Across their series of polymers, they found the LUMO energy level to remain relatively constant while the HOMO energy level varied with the different donor units. Additionally, higher HOMO energies tended to give lower threshold voltages in OFETs as a result of the decreased hole injection barrier from the gold source electrode. All polymers studied also were found to give unipolar p-channel OFETs, as the LUMO energies were not low enough to allow electron injection or transport. Further study of isoindigo-bithiophene polymers with different solubilizing alkyl chains showed that moving the alkyl branching position farther from the isoindigo core reduced the sterics of the alkyl group. This led to smaller π - π stacking distances and improved hole mobilities up to $3.62 \text{ cm}^2 \text{ V}^{-1} \text{ s}^{-1}$.⁶¹

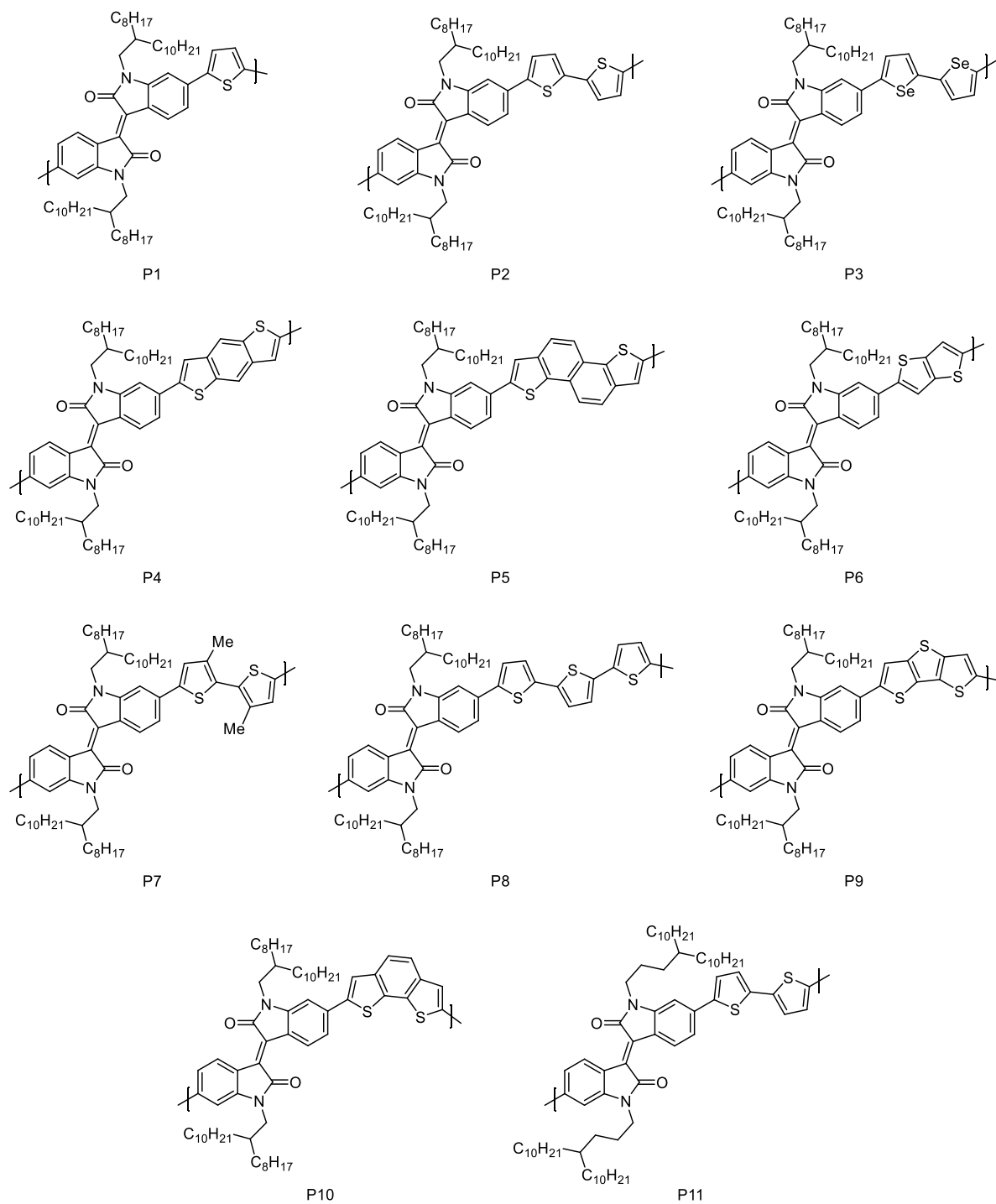


Chart 1.3 Survey of isoindigo donor-acceptor polymers for p-channel OFETs reported by Lei et al.^{59–61}

Table 1.1 Frontier molecular orbital energies and OFET device performance for p-type isoindigo donor-acceptor polymers.

Polymer	$E_{\text{HOMO}}^{\text{a}}$ (eV)	$E_{\text{LUMO}}^{\text{a}}$ (eV)	OFET Structure ^d	$\mu_{\text{h}}^{\text{b}}$ ($\text{cm}^2\text{V}^{-1}\text{s}^{-1}$)	$\mu_{\text{e}}^{\text{b}}$ ($\text{cm}^2\text{V}^{-1}\text{s}^{-1}$)	V_{T}^{b} (V)	Ref.
P1	-5.80 ^c	-3.81 ^c	BGTC(Au)	0.019	-	-20	59,60
P2	-5.65 ^c	-3.78 ^c	BGTC(Au)	1.06	-	-18	59,60
P3	-5.56 ^c	-3.79 ^c	BGTC(Au)	0.66	-	-10	60
P4	-5.84 ^c	-3.77 ^c	BGTC(Au)	0.48	-	-28	60
P5	-5.90 ^c	-3.75 ^c	BGTC(Au)	0.32	-	-30	60
P6	-5.70 ^c	-3.73 ^c	BGTC(Au)	0.34	-	-6	60
P7	-5.54 ^c	-3.78 ^c	BGTC(Au)	0.11	-	-5	60
P8	-5.48 ^c	-3.70 ^c	BGTC(Au)	0.016	-	-4	60
P9	-5.44 ^c	-3.72 ^c	BGTC(Au)	1.03×10^{-3}	-	-4	60
P10	-5.55 ^c	-3.70 ^c	BGTC(Au)	1.35×10^{-4}	-	-16	60
P11	-5.52 ^c	-3.74 ^c	BGTC(Au)	3.62	-	-2	61

^aHOMO and LUMO energies estimated from the onset of the first oxidation or reduction event in voltammetry, referenced against Fc/Fc^+ , typically assumed to be at an energy of -5.1 eV vs. vacuum. ^bDevice figures of merit recorded as best values. ^c Fc/Fc^+ assumed at -4.8 eV. ^dOFET architecture designated by abbreviations given in Figure 1.3.1, with metal used as the source and drain contacts given in brackets.

While there have been many additional polymers produced based on isoindigo for p-channel OFETs using a variety of donor units, these materials have similar LUMO energy levels due to the localization of the LUMO to the isoindigo unit. Two strategies have been used to produce isoindigo based materials with lowered LUMO energy levels; coupling isoindigo to another electron poor unit to create an acceptor-acceptor polymer delocalizes the LUMO and changes its energy, while modifications of the isoindigo core structure to make it more electron-deficient also changes the LUMO energy of donor-acceptor polymers. These strategies allow for isoindigo based systems to be used in ambipolar and n-channel OFETs rather than only p-channel devices and will be covered in the next two sections.

1.4.3 Acceptor-Acceptor Isoindigo Polymers

One of the first examples of an all-acceptor polymer was the poly(isoindigo) homopolymer, shown as P12 in Chart 1.4. This was synthesized along with poly(isoindigo-benzothiadiazole) (P13) using Suzuki coupling reactions.⁶² Poly(isoindigo) had relatively low frontier molecular orbital energies and was used primarily as electron acceptor materials for organic solar cells paired with the electron donor P3HT. In addition, the electron mobility for poly(isoindigo) was measured as $3.7 \times 10^{-7} \text{ cm}^2 \text{ V}^{-1} \text{ s}^{-1}$ using the SCLC method. This example showed that the all-acceptor design strategy could be used to produce electron conducting materials. A polymer with the same conjugated backbone was synthesized by Ganguly et al.²⁶ and the material was measured in OFETs to give unipolar n-channel devices with an electron mobility of $1.0 \times 10^{-4} \text{ cm}^2 \text{ V}^{-1} \text{ s}^{-1}$. While the study of poly(isoindigo-benzothiadiazole) by Stalder et al.⁶² did not include a measurement of its charge carrier mobility, this polymer had a low LUMO energy of -3.90 eV. The same polymer structure was made using longer alkyl chains in 2014 along with an isoindigo-thienopyrroledione copolymer (P14, P15) as a set of acceptor-acceptor polymers for OFETs.⁶³ Based on electrochemical and spectroscopic measurements the thienopyrroledione was determined to be a stronger acceptor unit compared to the benzothiadiazole. Interestingly they also observed that the HOMO and LUMO were delocalized along the entire conjugated backbone when visualised using density functional theory (DFT) calculations. This is different than what is usually observed in donor-acceptor systems where the HOMO is localized to the donor and the LUMO is localized to the acceptor. When tested in OFETs both polymers showed unipolar n-channel performance, with the benzothiadiazole polymer producing the higher electron mobility measured at $0.22 \text{ cm}^2 \text{ V}^{-1} \text{ s}^{-1}$. The difference in performance between the polymers was attributed to their packing in thin films, where the benzothiadiazole containing polymer produced more intense edge-on diffraction peaks in X-ray diffraction experiments. This example showed both that the isoindigo based materials could be used as high-performance electron conducting materials and that the acceptor-acceptor design strategy was a viable route to these materials.

In 2013 Grenier et al.⁶⁴ produced a series of isoindigo acceptor-acceptor polymers based on thienopyrroledione and diketopyrrolopyrrole using either Suzuki reactions or direct (hetero)arylation polymerization, with structures shown as P16-P18. The thienopyrroledione containing polymers (P16, P17) made by Suzuki reactions led to either no conversion to the desired

polymer due to decomposition of the brominated monomers, or polymers of low molecular weights in low yields. As an alternative to the unsuccessful Suzuki coupling the polymers were synthesized using direct-(hetero)arylation polymerization which gave the desired products in improved yields and molecular weights. Through optimization of the polymerization reactions with a variety of phosphine ligands and bases, polymers of a range of molecular weights were produced. When these polymers were measured using UV/Vis spectroscopy it was observed that the absorption onset was red shifted with increasing molecular weight, indicating a smaller bandgap in the large molecular weight polymers. Charge carrier mobility measurements in OFETs showed that the thienopyrroledione containing polymers performed better than those with the diketopyrrolopyrrole, with P17 giving the highest electron mobility of $3.5 \times 10^{-3} \text{ cm}^2 \text{ V}^{-1} \text{ s}^{-1}$. Similar to the previous observations of Lei et al.^{59,60} the polymer containing the centrosymmetric unit produced better device performance compared to its axisymmetric analogue.

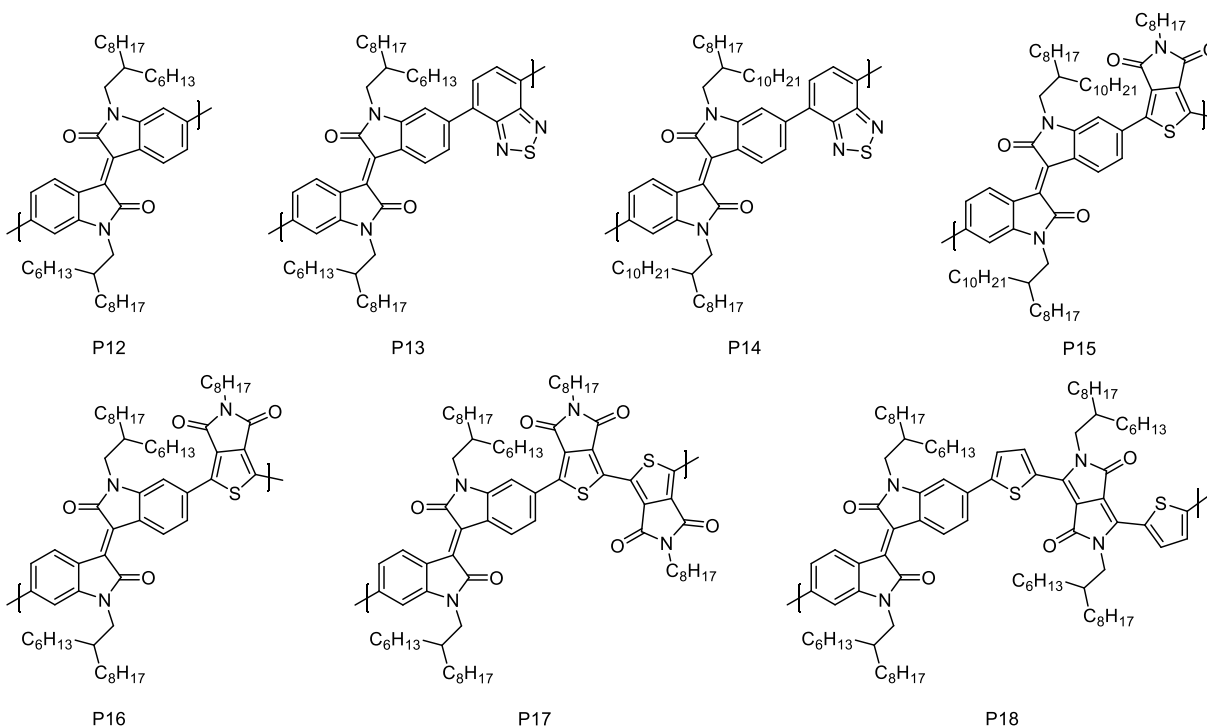


Chart 1.4 Survey of isoindigo-based acceptor-acceptor polymers used as electron conducting materials in organic electronics.

Table 1.2 Frontier molecular orbital energies and OFET device performance for isoindigo acceptor-acceptor polymers.

Polymer	$E_{\text{HOMO}}^{\text{a}}$ (eV)	$E_{\text{LUMO}}^{\text{a}}$ (eV)	OFET Structure ^d	$\mu_{\text{h}}^{\text{b}}$ ($\text{cm}^2\text{V}^{-1}\text{s}^{-1}$)	$\mu_{\text{e}}^{\text{b}}$ ($\text{cm}^2\text{V}^{-1}\text{s}^{-1}$)	V_{T}^{b} (V)	Ref.
P12	-5.54	-3.84	-	-	$3.7 \times 10^{-7}^{\text{d}}$	-	62
P12	-6.22	-3.79	BGBC(Au)	-	2.8×10^{-4}	48	26
P13	-5.67	-3.90	-	-	-	-	62
P14	-5.68 ^c	-3.54 ^c	BGTC(Au)	-	0.22	42	63
P15	-5.70 ^c	-3.66 ^c	BGTC(Au)	-	0.01	8	63
P16	-6.0 ^f	-4.1 ^f	BGBC(Au)	-	3.0×10^{-4}	47	64
P17	-6.1 ^f	-4.1 ^f	BGBC(Au)	-	3.5×10^{-3}	17	64
P18	-5.3 ^f	-4.0 ^f	BGBC(Au)	-	2.7×10^{-4}	30	64

^aHOMO and LUMO energies estimated from the onset of the first oxidation or reduction event in voltammetry, referenced against Fc/Fc^+ , typically assumed to be at an energy of -5.1 eV vs. vacuum. ^bDevice figures of merit recorded as best values. ^c Fc/Fc^+ assumed at -4.8 eV. ^dOFET architecture designated by abbreviations given in Figure 1.3.1, with metal used as the source and drain contacts given in brackets. ^eCharge carrier mobility determined using the SCLC method. ^fElectrochemistry referenced against SCE, assumed to be at -4.71 eV vs. vacuum.

While these examples show that the acceptor-acceptor design strategy can be used to produce high quality isoindigo-based materials for n-channel OFETs, it has still been relatively unexplored. This is likely due to the small number of acceptor units that can be easily coupled, and traditional cross coupling reactions sometimes are not well suited for some pairs of electron-deficient units, as shown by Grenier et al.⁶⁴ An alternative strategy is to structurally modify the isoindigo structure to optimize its electronics and geometry, which has been much more commonly used in the literature and will be discussed in the next section.

1.4.4 Structural Modifications of Isoindigo

There have been several different ways that isoindigo has been structurally modified to make it more well suited for organic electronics. These structural modifications are made to change the frontier molecular orbital energies, increase the planarity of the conjugated unit, or to increase the conjugation length of the unit. These modified isoindigo analogues can be classified as halogenated, heterocycle substituted, peripherally expanded, or core expanded, as shown in Figure 1.10.⁶⁵

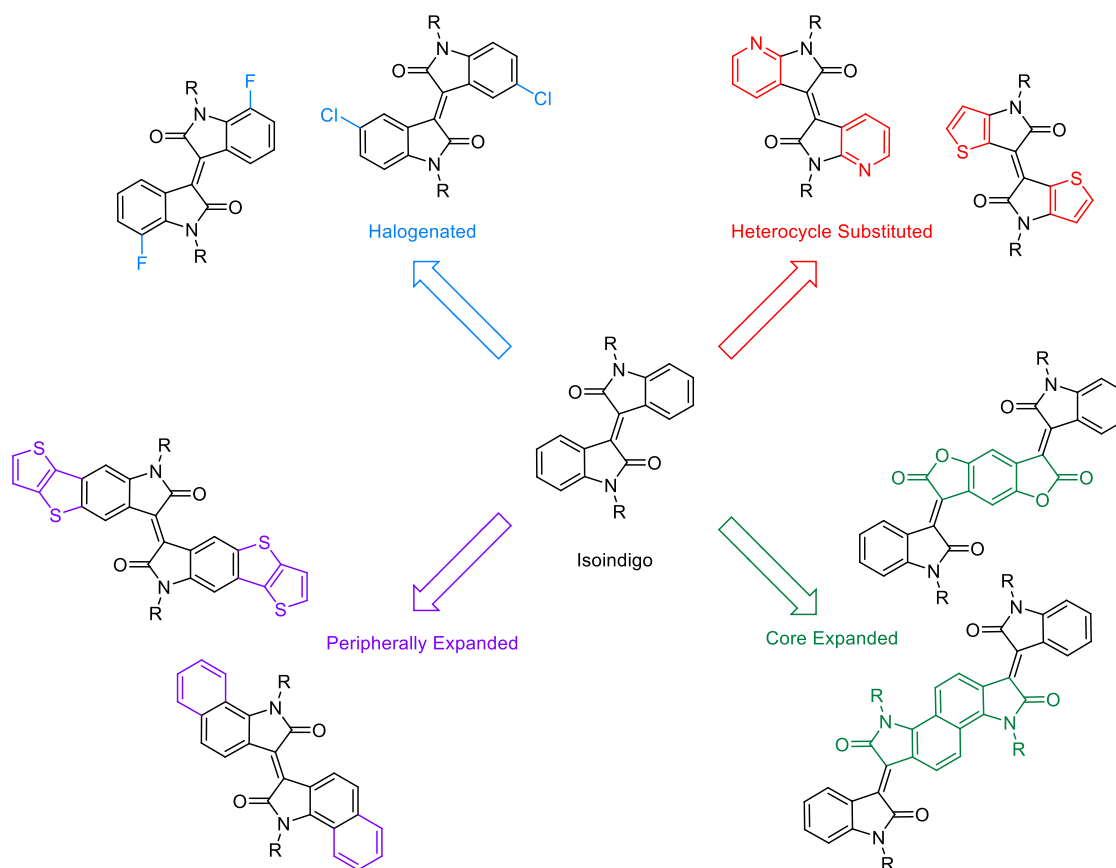


Figure 1.10 Classification of structural variants on isoindigo. Figure adapted with permission from Randell, N. M.; Kelly, T. L. Recent Advances in Isoindigo-Inspired Organic Semiconductors. *Chem. Rec.* **2019**, *18*, 1–17. Copyright 2019 John Wiley & Sons, Inc.

Halogenation of isoindigo is used to lower the frontier molecular orbital energy levels and can also play a role in solid state packing depending on either the size of the halogen or if there is any potential for planarizing non-covalent interactions. Heterocycle substituted isoindigo variants also give altered HOMO and LUMO energies and help to planarize the isoindigo core. In isoindigo there is a steric clash between the amide oxygen and hydrogen atoms in the C-H bonds at the 4,4' positions. This interaction is removed in thienoisindigo, where the two terminal benzene rings in isoindigo are replaced with thiophenes, giving a more planar structure.⁶⁶ Similarly, the replacement of isoindigo C-H bonds at the 7,7' positions with a nitrogen atom to give azaisoindigo removes the potential for steric clash between this hydrogen and substituents installed in the 6,6' positions in conjugated polymers. In peripherally and core expanded isoindigo structures, extended conjugation results in materials with lower bandgaps and large regions with planar geometries to help give ordered packing in the solid state. The present work focuses on core expanded isoindigo structures

and so the other classes will not be reviewed, however other reviews on the topic of structural modifications to isoindigo have been published.^{4,56,57,65–67}

1.4.5 Core Expanded Isoindigo and Bisisoindigo Polymers

Structural variants on isoindigo using an expanded core insert an additional conjugated unit in the place of the exocyclic carbon-carbon double bond of isoindigo. This alteration, while useful in extending conjugation, can also be used to increase the coplanarity of the isoindigo unit to increase π - π stacking and tune the density of alkyl chains along the polymer backbone. Many core-expanded isoindigo derivatives have been reported because of the potential insertion of many different conjugated units, giving different materials properties. The first was reported by Yan et al.⁶⁸ who used a benzodifurandione unit to extend the conjugation of isoindigo to create two donor-acceptor polymers (P19 and P20, Chart 1.5). The benzodifurandione unit gave a planar geometry allowing for strong π - π stacking. It was found that the bithiophene containing polymer (P20) was insoluble despite its long and branched alkyl chains, however the thiophene containing polymer (P19) was soluble and fully characterized. OFET devices were made both with and without a poly(methyl methacrylate) encapsulation layer using a bottom-gate bottom-contact architecture. The encapsulated devices gave unipolar n-channel performance with electron mobilities up to $5.4 \times 10^{-3} \text{ cm}^2 \text{ V}^{-1} \text{ s}^{-1}$, while the unencapsulated devices were ambipolar with balanced mobilities of $9.0 \times 10^{-3} \text{ cm}^2 \text{ V}^{-1} \text{ s}^{-1}$ and $4.9 \times 10^{-3} \text{ cm}^2 \text{ V}^{-1} \text{ s}^{-1}$ for electrons and holes respectively. This change from n-channel to ambipolar was unexpected and hypothesized to be a result of atmospheric water or air altering the polymer frontier orbital energies or the work function of the gold electrodes to change the charge injection barriers, however this was not explored experimentally.

Another example of this structure was reported by Lei et al.⁶⁹ where a benzodifurandione unit was incorporated to give a polymer backbone resembling poly(*p*-phenylene vinylene) in a locked geometry (P21). Poly(*p*-phenylene vinylene) based polymers had previously performed rather poorly as hole carrying materials due to their *cis-trans* isomerization under UV light and orientational disorder due to poor intermolecular interactions. The benzodifurandione polymers prevented the unwanted isomerization while also giving a very low LUMO energy of -4.10 eV due to the electron withdrawing groups within the polymer backbone. The alkyl chains were also modified relative to those used by Yan et al.⁶⁸ to be much longer to help solubilize the polymers, and the branching position was moved farther away from the polymer backbone. These

improvements in morphology and electronics led to an impressive electron mobility of $1.1 \text{ cm}^2 \text{ V}^{-1} \text{ s}^{-1}$ in top-gate bottom-contact OFET devices. These devices were also stable up to 30 days as a result of the low LUMO energy and the device geometry, as the top-gate architecture gives some encapsulation.

Based on the success of this benzodifurandione containing polymer, more donor-acceptor polymers were synthesized using this core or modifications on it. Lei et al.⁷⁰ produced a polymer (P22) with the same core structure as the bithiophene polymer by Yan et al.⁶⁸ (P20) but with the longer alkyl chains that were more successful in the benzodifurandione work by Lei et al.⁶⁹ When tested in OFET devices while under an inert atmosphere in a glove box this polymer produced n-channel devices with an electron mobility up to $1.74 \text{ cm}^2 \text{ V}^{-1} \text{ s}^{-1}$. When tested under ambient conditions they found the devices were ambipolar with carrier mobilities of $1.45 \text{ cm}^2 \text{ V}^{-1} \text{ s}^{-1}$ and $0.47 \text{ cm}^2 \text{ V}^{-1} \text{ s}^{-1}$ for electrons and holes respectively. This change from n-channel to ambipolar was similar to that observed by Yan et al.⁶⁸ To further investigate this, Lei et al.⁷⁰ performed DFT calculations to model the interaction between oxygen and polymer P22 which suggested a stable complex between molecular oxygen and the polymer. Further, the oxygen complex was calculated to have a slightly lower LUMO energy and slightly higher HOMO energy. A higher HOMO energy should result in a lower hole injection barrier which could explain the ambipolar character of the polymer in the presence of oxygen as due to oxygen doping. This is an interesting finding as electron conducting polymers and ambipolar polymers are typically thought to be unstable towards oxygen.

A fluorinated analogue of the benzodifurandione containing core expanded isoindigo was reported by Zheng et al.⁷¹ and was incorporated into polymers with bithiophene and biselenophene donor units (P23 and P24). Fluorination was used to lower the polymer LUMO energy but due to the similar van der Waals radii of hydrogen and fluorine it was not predicted to negatively impact the polymer planarity. Calculations using DFT predicted hydrogen bonding between the hydrogen in the thiophene 3 position and one of the fluorine atoms, while the other fluorine was predicted to be in a non-covalent interaction with the chalcogen of the thiophene or selenophene. The rotational barrier of the bond between the fluorinated unit and the thiophene in P23 was found to be $3.8 \text{ kcal mol}^{-1}$, indicating the presence of a non-covalent conformational lock preserving coplanarity in the polymer. Substitution of the thiophenes for selenophenes gave little change to the frontier

molecular orbital energies and packing in the solid state as measured by grazing incident X-ray diffraction. Performance of these polymers in OFETs gave unipolar n-channel devices, however the square root transfer curves were observed to be significantly kinked. Typically, this is observed as a result of large contact resistance, however it was shown that in this case the frequency of the kinked transfer curve could be linked to the polymer casting conditions where higher spin coating spin speeds decreased the percentage of non-ideal transfer curves. It was also shown that faster spin speeds led to more disordered films, suggesting morphology could play a role in the non-ideal transfer curves. Another hypothesis for the kinked transfer curves was electron trapping at the interface of the SiO₂ dielectric layer, however when devices were made using a different dielectric, the non-ideality was still present. As it was unclear whether the kinked transfer curves were resulting in overestimation of the charge carrier mobility, mobilities were reported at both low and high gate voltages before and after the kink. The thiophene containing polymer P23 had mobilities up to 14.9 cm² V⁻¹ s⁻¹ and 1.24 cm² V⁻¹ s⁻¹ with low and high gate voltages respectively, while the selenophene polymer P24 had mobilities up to 6.14 cm² V⁻¹ s⁻¹ and 0.64 cm² V⁻¹ s⁻¹ with low and high gate voltages respectively. Despite the confusion resulting from the non-ideal transfer curves, these materials were some of the highest mobility electron conducting polymers reported.

Dai et al.⁷² modified the benzodifurandione structure by performing an aza-substitution on the isatin units to replace the benzene ring with a pyridine. This was designed to lower the LUMO energy due to the more electronegative sp² nitrogen atom, while also helping to increase the planarity, as the nitrogen atom is less sterically demanding than the C-H unit it is replacing. Based on DFT calculations the pyridine nitrogen and the sulfur of the neighboring thiophene are on the same side of the polymer backbone with a calculated S-N distance significantly smaller than the sum of their van der Waals radii. This suggested the presence of a non-covalent electronic interaction between the sulfur and nitrogen atoms and led to a decrease in the DFT calculated dihedral angle between the pyridine and thiophene units to give a more planar polymer backbone. The planar geometry and low LUMO energy were both beneficial for device performance and P25 gave n-channel OFETs with a charge carrier mobility up to 3.22 cm² V⁻¹ s⁻¹.

A series of core expanded isoindigo polymers were reported by Deng et al.^{73–75} containing two quinoindal thiophene dioxide units, with the highest performing material P26 displayed. The quinoindal structure was used to ensure a planar geometry and to help with charge transfer along the

polymer backbone, as it was thought that the quinoidal thiophenes were more conductive than their aromatic form.⁷³ The modified isoindigo unit was prepared using the indophenine reaction which is well known to produce a mixture of inseparable isomers,⁷⁶ however after oxidation of the thiophenes the materials could be thermally isomerized to the most thermodynamically stable isomer. Stille reactions were then used to prepare donor-acceptor polymers.⁷³ Despite having relatively disordered packing in thin films as observed by X-ray diffraction these polymers worked quite well in OFET devices and resulted in charge carrier mobilities up to $0.18 \text{ cm}^2 \text{ V}^{-1} \text{ s}^{-1}$ with low threshold voltages and high $I_{\text{on/off}}$ ratios.

An extension on the benzodifurandione unit was reported by Deng et al.⁷⁷ where its central benzene ring was replaced with a naphthalene unit in P27. This modification was predicted to reduce the electron-deficient nature of the structure leading to ambipolar device performance. The larger aromatic system was also used to increase the potential for π - π interactions allowing for stronger intermolecular interactions and better film morphologies. It was found that this structural change led to higher frontier molecular orbital energies in polymers when compared to the original benzodifurandione unit report by Lei et al.⁷⁰ in P22. This polymer was ambipolar in OFET devices with well balanced electron and hole mobilities of $0.51 \text{ cm}^2 \text{ V}^{-1} \text{ s}^{-1}$ and $0.50 \text{ cm}^2 \text{ V}^{-1} \text{ s}^{-1}$ respectively. It was proposed that the HOMO and LUMO energy levels were favourably positioned relative to the work function of the gold source/drain electrodes resulting in similar injection barriers to account for the similar electron and hole transport. Additionally, they observed the polymer to take an edge-on orientation relative to the substrate and crystallize with thermal annealing, helping to produce improved OFET results.

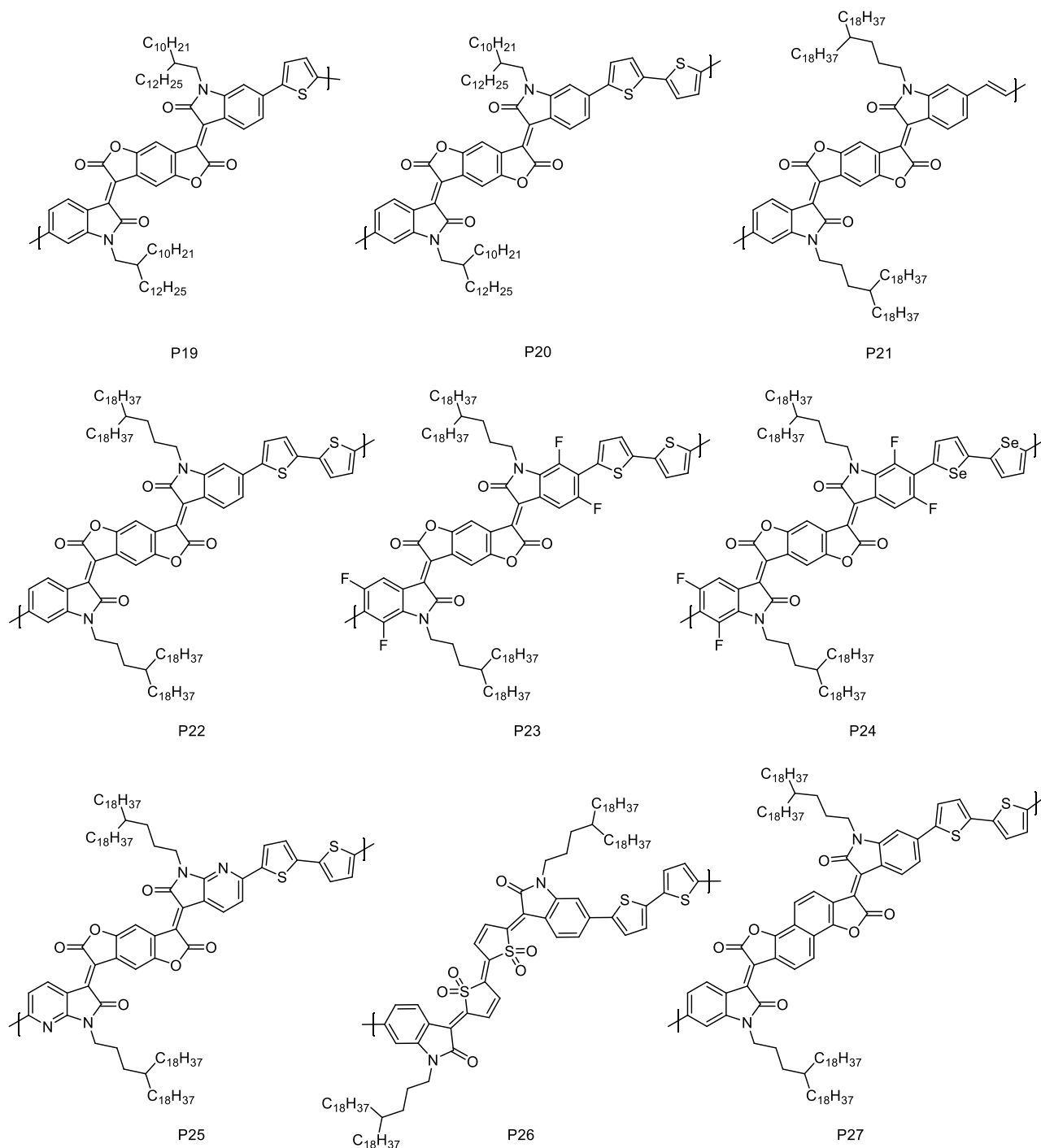


Chart 1.5 Structures of core expanded isoindigo units in donor-acceptor polymers.

Randell et al.⁷⁸ developed the bisisoindigo acceptor, another structural analogue of the naphthodifurandione structure in P27 where the ester oxygens are replaced with alkylated nitrogen atoms. This structure can also be viewed as a dimer of isoindigo where two isoindigo units are ring fused together in a naphthalene core. The structure of bisisoindigo is displayed in Chart 1.6 along

with polymers incorporating this structure. Like other structural variations on isoindigo, bisisoindigo provided extended conjugation and a relatively low LUMO energy due to its electron withdrawing lactam rings. Additionally, the two additional nitrogen atoms relative to the benzodifurandione based materials meant that there was potential for more alkyl chains along the polymer, reducing the need for such large alkyl chains to provide solubility. Soon after the initial report of the bisisoindigo structure it was used in donor-acceptor polymers by Jiang et al.⁷⁹ with a series of thiophene based acceptors, P28-P30. These polymers showed limited solubility as they could only be dissolved in hot chlorinated solvents, and there was little change in the solution and thin film UV/Vis spectra suggesting some preaggregation in solution. It was also observed by DFT calculations that both the HOMO and LUMO were predominantly localized to the bisisoindigo unit and that the HOMO energy level did not increase as the conjugation length of the donor was increased. When testing these materials in BGTC OFETs they showed ambipolar charge transport with kinked transfer curves in the hole transport region attributed to interface related traps near the dielectric layer. Electron transport was observed to degrade quickly when devices were tested in air as a result of the relatively high LUMO energies for these polymers. Further testing was done using the TGBC architecture while switching the dielectric from SiO₂ to poly(methyl methacrylate) (PMMA) which circumvented the issues of air stability and non-linear transfer curves. This supports the idea that the non-linearity in the square root transfer curves was a result of defects at the dielectric semiconductor interface and showed that encapsulation by the dielectric PMMA layer can be used to stabilize the electron transport in these polymers.

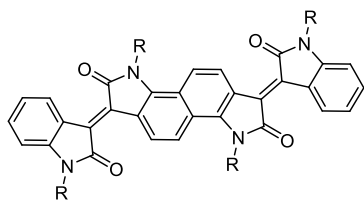
Two more bisisoindigo donor-acceptor polymers were reported by Randell et al.⁸⁰ containing thiophene and terthiophene donor units. These materials were compared to isoindigo-thiophene copolymers and showed that altering the number of acceptor units or their conjugation length can be used to alter the LUMO energy and charge transport properties. This report mainly focused on organic photovoltaic (OPV) applications, but the polymers were also tested in OFETs giving ambipolar performance. Film morphology was studied using grazing incidence wide angle X-ray scattering (GIWAXS) which showed that the polymers displayed a preferential face-on orientation relative to the substrate and relatively amorphous packing. The high LUMO energy relative to other polymers discussed so far was likely the cause of the low electron mobilities in these polymers, but this example showed that by increasing the number or strength of the acceptor units the LUMO energy could be lowered and the electron mobility could be improved.

Some other examples of bisoindigo based polymers have been reported that do not use the donor-acceptor design strategy. A recent example by Ganguly et al.²⁶ synthesized a bisoindigo homo-polymer using a metal free aldol synthesis. This synthetic strategy is beneficial for producing conjugated polymers as it circumvents the use of expensive transition metal catalysts, is atom-economical, and prevents the production of stoichiometric toxic by-products as in Stille coupling reactions. In this case the aldol polymerisation also allowed for synthesis of the bisoindigo homo-polymer which could not be performed using Stille or Suzuki methods because of difficulties in preparing the required synthetic precursors. Molecular weights of the aldol produced polymer were also similar to those obtained by traditional cross-coupling reactions. In OFET devices this polymer gave unipolar n-channel performance, where the other bisoindigo polymers were ambipolar. The relatively low electron mobility of poly(bisoindigo) of $9.2 \times 10^{-5} \text{ cm}^2 \text{ V}^{-1} \text{ s}^{-1}$ was attributed to poor interchain transport, potentially caused by disordered solid-state packing.

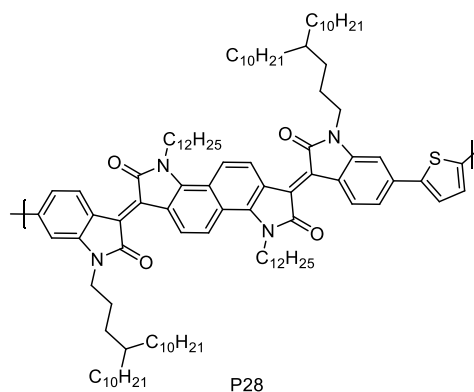
Another way to create a homo-polymer based on the bisoindigo structure is to create a polymer which links the bisoindigo units through ring fusion rather than a single C-C bond. This idea was explored by Jiang et al.⁸¹ who created a series of oligomers with two, three, four or six isoindigo units (one to three bisoindigo units) ring fused together. It was observed that the increasing conjugation lowered both the HOMO and LUMO energies and decreased the optical bandgap significantly. The bandgap also varied linearly with the number of isoindigo repeat units suggesting that the effective conjugation length followed the oligomer chain length and that further extensions could further reduce the bandgap. This also indicated that the structures were very planar along the polymer length, which was supported by DFT calculations of optimized structures. Only the oligomer with four isoindigo repeat units was tested in OFETs which gave ambipolar performance and charge carrier mobilities of $8.4 \times 10^{-4} \text{ cm}^2 \text{ V}^{-1} \text{ s}^{-1}$ and $1.1 \times 10^{-5} \text{ cm}^2 \text{ V}^{-1} \text{ s}^{-1}$ for electrons and holes respectively. The modest performance was attributed to weak intermolecular interactions giving poor film morphologies due to the bulky 2-butyloctyl chains used. This design strategy was extended to polymers by Onwubiko et al.²⁴ who used a metal free aldol polymerisation to create materials with a continuous locked geometry all along the polymer backbone. It was shown that by controlling the identity of the alkyl chains as well as the concentrations of monomers and acid catalyst the molecular weights of the resulting polymers could be controlled to some extent. DFT calculations showed that despite the locked geometry there was a dihedral angle of approximately 18 degrees across the exocyclic C-C double bonds resulting from steric hindrance.

between the amide carbonyl and C-H bonds on the neighboring aromatic unit. The best performing material in OFETs achieved an electron mobility of $0.03 \text{ cm}^2 \text{ V}^{-1} \text{ s}^{-1}$ and showed extended stability in air up to 300 hours due to the polymers low LUMO energy level.

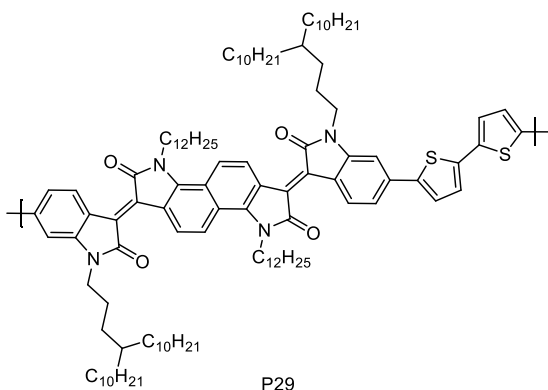
These examples show that core-expanded isoindigo structures can be used to produce electron conducting materials for OFETs, often with high performance and device stability. This makes the core-expanded isoindigo structure a useful design principle for the synthesis of the next generation of high performance isoindigo-based OFET materials.



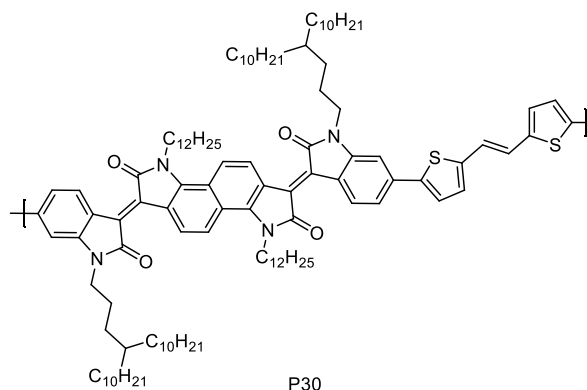
Bisisoindigo



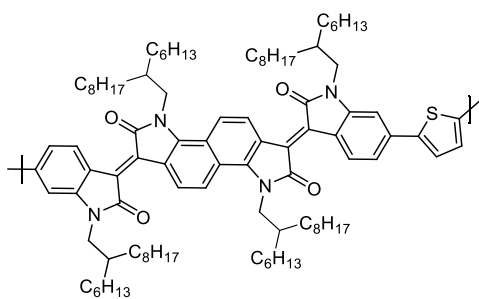
P28



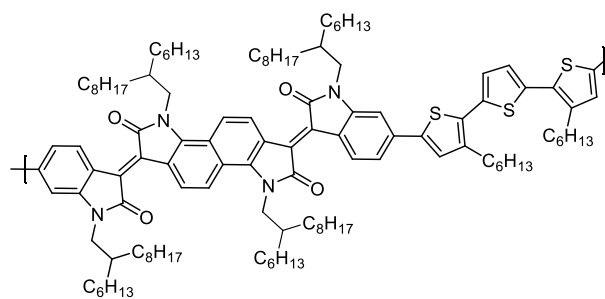
P29



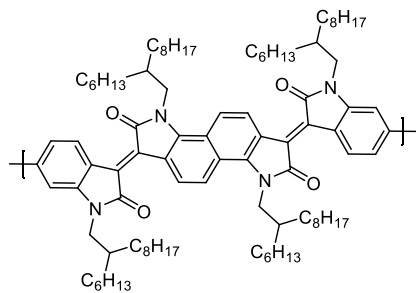
P30



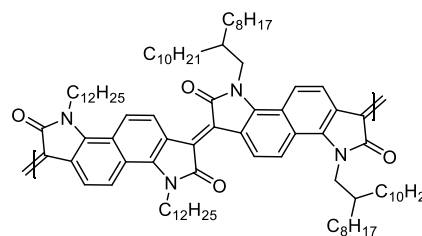
P31



P32



P33



P34

Chart 1.6 Structures of bisisoindigo and bisisoindigo containing polymers.

Table 1.3 Frontier molecular orbital energies and OFET device performance for donor-acceptor polymers using core-expanded isoindigo derivatives.

Polymer	$E_{\text{HOMO}}^{\text{a}}$ (eV)	$E_{\text{LUMO}}^{\text{a}}$ (eV)	OFET Structure ^j	$\mu_{\text{h}}^{\text{b}}$ ($\text{cm}^2\text{V}^{-1}\text{s}^{-1}$)	$\mu_{\text{e}}^{\text{b}}$ ($\text{cm}^2\text{V}^{-1}\text{s}^{-1}$)	V_{T}^{b} (V)	Ref.
P20	-5.79 ^c	-4.11 ^c	BGBC(Au) ^d	-	5.4×10^{-3}	10 ^e	68
P20	-5.79 ^c	-4.11 ^c	BGBC(Au)	4.9×10^{-3}	9.0×10^{-3}	-30 / 20 ^e	68
P21	-6.21 ^c	-4.10 ^c	TGBC(Au)	-	1.1	5	69
P22	-5.72 ^c	-4.15 ^c	TGBC(Au)	-	1.74	40	70
P22	-5.72 ^c	-4.15 ^c	TGBC(Au) ^f	0.47	1.45	-57 / 55	70
P23	-5.96 ^c	-4.32 ^c	TGBC(Au)	-	1.24 (14.9) ^g	-17	71
P24	-5.91 ^c	-4.34 ^c	TGBC(Au)	-	0.64 (1.64) ^g	3	71
P25	-5.80 ^c	-4.37 ^c	TGBC(Au)	-	3.22	40	72
P26	-5.99 ^c	-4.18 ^c	BGBC(Au)	-	0.18	2.3	75
P27	-5.65 ^c	-3.84 ^c	BGBC(Au)	0.50	0.51	-40 / 10 ^e	77
P28	-5.16 ^c	-3.66 ^c	BGTC(Au)	3.2×10^{-3}	-	10	79
P28	-5.16 ^c	-3.66 ^c	TGBC(Au)	1.1×10^{-3}	6.2×10^{-3}	1 / 9	79
P29	-5.16 ^c	-3.58 ^c	BGTC(Au)	1.55	0.021	2 / 38	79
P29	-5.16 ^c	-3.58 ^c	TGBC(Au)	0.41	0.18	-13 / 40	79
P30	-5.24 ^c	-3.58 ^c	BGTC(Au)	1.79	0.087	-6 / 40	79
P30	-5.24 ^c	-3.58 ^c	TGBC(Au)	0.45	0.16	-13 / 36	79
P31	-5.73	-4.09	BGBC(Au)	1.5×10^{-3} ^h	1.7×10^{-3} ^h	-30 / 30 ^e	80
P32	-5.64	-4.02	BGBC(Au)	2.6×10^{-3} ^h	6.0×10^{-4} ^h	-20 / 50 ^e	80
P33	-6.03	-3.94	BGBC(Au)	-	9.3×10^{-5}	51	26
P34	-5.30 ⁱ	-4.20 ⁱ	BGTC(Au)	-	0.03	30 ^e	24

^aHOMO and LUMO energies estimated from the onset of the first oxidation or reduction event in voltammetry, referenced against Fc/Fc^+ , typically assumed to be at an energy of -5.1 eV vs. vacuum. ^bDevice figures of merit recorded as best values. For ambipolar OFETs the threshold voltage for p-channel is reported first. ^c Fc/Fc^+ assumed at -4.8 eV. ^dOFET devices encapsulated using a PMMA layer. ^eThreshold voltages not reported in reference, estimated by eye using onset of I_{on} in transfer curves. ^fDevices were manufactured under ambient conditions. ^gCharge carrier mobilities extracted from kinked transfer curves. Measurement at high V_{G} listed first, measurement at low V_{G} listed in brackets. ^hAverage values reported. ⁱHOMO determined by photoelectron spectroscopy, LUMO estimated as $\text{HOMO} - E_{\text{g, opt}}$. ^jOFET architecture designated by abbreviations given in Figure 1.3.1, with metal used as the source and drain contacts given in brackets.

1.5 Thesis Objectives

In the preceding literature review it was shown that both all-acceptor polymers and core expanded isoindigo donor-acceptor polymers can be used as high-performance ambipolar and electron conducting materials for OFETs and other organic electronics. It was hypothesized that a combination of these two strategies can also be used to produce conjugated polymers with improved figures of merit in OFET applications. This hypothesis was explored in two ways, outlined below:

1. Acceptor-acceptor polymers based on bisisoindigo, a core expanded isoindigo developed by Randell et al.⁷⁸, in combination with benzothiadiazole-based acceptors are synthesized and applied in OFET devices. The optical and electronic properties of these materials are characterised, and their figures of merit discussed and compared to similar literature examples. This topic will be discussed in Chapter 2.
2. Synthetic methods towards thiophene dioxide containing acceptor units are investigated towards the goal of producing all-acceptor copolymers with bisisoindigo. The installation of electron withdrawing thiophene dioxide units is studied using both pre-polymerisation and post-polymerisation methods. This topic will be discussed in Chapter 3.

Chapter 2 – Bisisoindigo Acceptor-Acceptor Polymers

2.1 Motivation for Electron-Deficient Bisisoindigo Polymers

In the previous chapter it was shown that the synthesis of electron conducting materials based on isoindigo could be achieved through either the pairing of two electron-deficient units in an acceptor-acceptor polymer, or by synthesizing core-expanded isoindigo derivatives in donor-acceptor polymers. In a study by Randell et al.⁸⁰ it was shown that increasing the number of electron-deficient units in isoindigo and bisisoindigo polymers led to improved electron mobilities in ambipolar OFETs. In work by Ganguly et al.²⁶ it was shown that a bisisoindigo homopolymer displayed unipolar n-channel OFET performance, albeit with a lower electron mobility. Pairing bisisoindigo with more electron-deficient units compared to the thiophene donors used in work by Randell et al.⁸⁰ allows for the study of relatively underexplored electron-deficient polymers and potentially lead to improved OFET device performance.

In this chapter I combine the above two synthetic strategies by producing bisisoindigo and benzothiadiazole containing polymers and study their optoelectronic properties and OFET performance. Structures of each synthesized polymer is given in Chart 2.1. The electron-deficient benzothiadiazole unit in P1(H) is installed to increase the acceptor strength in these polymers relative to previously reported thiophene and alkene based bisisoindigo polymers. Fluorination of the benzothiadiazole unit in P2(F) is used to further reduce the LUMO energy of the resulting polymer, while helping to planarize the polymer backbone. Polymer P3(B) is synthesized without thiophene units to compare the effect of these electron rich units in the otherwise electron-deficient polymers. In all three materials, the acceptor-rich polymer design helped to delocalize the frontier molecular orbitals and lower their energy levels. The shape of the polymer backbone was observed to depend on the orientation of the benzothiadiazole units, impacting the physical and optoelectronic properties of these materials in comparison to previously reported bisisoindigo polymers. Ambipolar OFET performance was achieved for polymers P1(H) and P2(F) due to their small bandgap, with balanced hole and electron mobilities in bottom-gate bottom-contact (BGBC) OFETs. In addition, bottom-gate top-contact (BGTC) devices with LiF/Al electrodes are used to produce n-channel OFETs with significantly reduced threshold voltages due to improved alignment of the polymer LUMO energy level and the metal Fermi energy. This report shows that two common synthetic strategies to conjugated polymers can be combined to modify frontier molecular

orbital energies and produce high performance materials for OFETs and other areas of organic electronics.

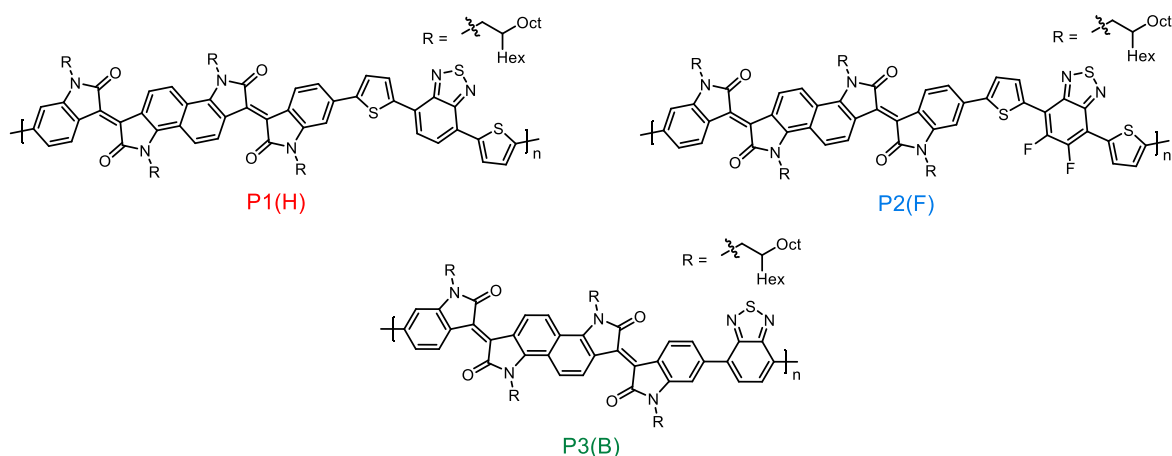
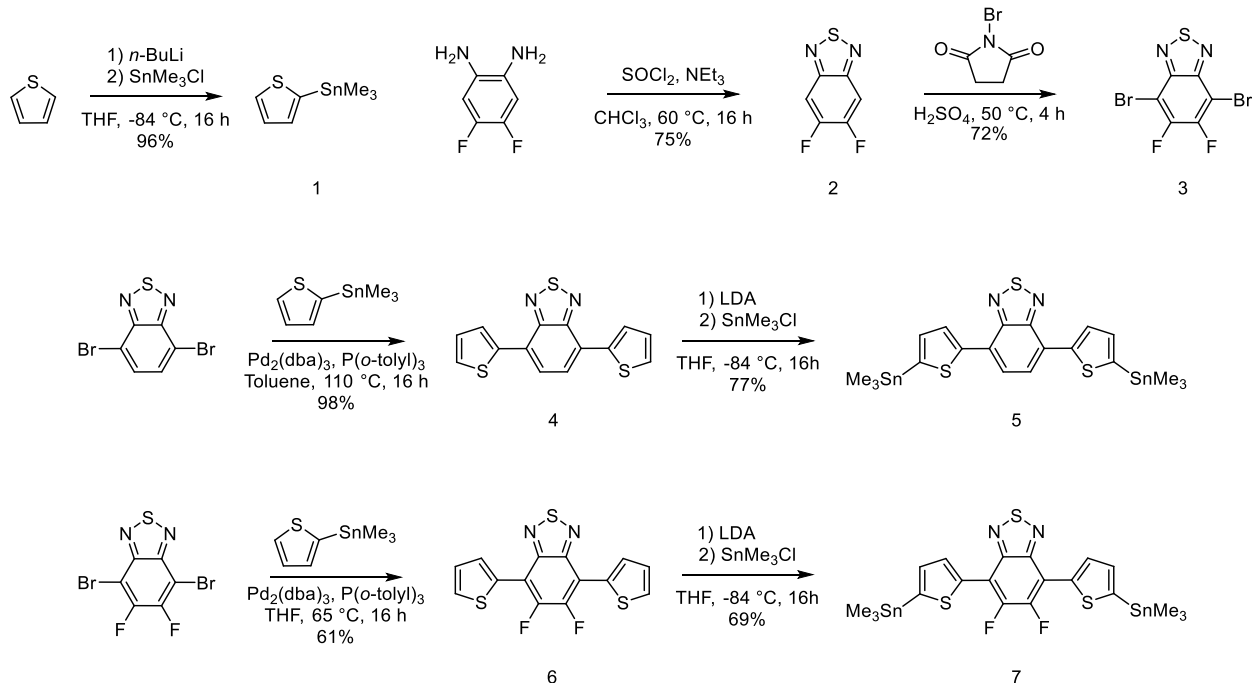


Chart 2.1 Structures of polymers synthesized and studied throughout Chapter 2.

2.2 Results and Discussion

2.2.1 Polymer Synthesis

Synthesis of dibromobisisoindigo was performed as previously reported by Randell et al.⁸⁰ The bisoindigo polymers containing the dithienyl-benzothiadiazole units P1(H) and P2(F) were synthesized using Stille reactions, and the synthesis of the distannylated monomer units were prepared as shown in Scheme 2.1. Both Stille reagents required the use of 2-trimethylstannyl thiophene (1), which was synthesized by the sequential reaction of thiophene with *n*-BuLi and trimethyltin chloride.⁸² To produce the Stille reagent required for the synthesis of polymer P1(H), 2-trimethylstannyl thiophene (1) was reacted with the commercially available 4,7-dibromo-2,1,3-benzothiadiazole using a palladium catalyzed Stille reaction to produce dithienyl-benzothiadiazole (4).^{83–85} To synthesize 4,7-bis(5-(trimethylstannyl)thiophen-2-yl)-2,1,3-benzothiadiazole (5), dithienyl-benzothiadiazole (4) was deprotonated by reaction with lithium diisopropylamide followed by reaction with trimethyltin chloride.⁸⁶ The synthesis of the Stille reagent required for synthesis of P2(F) followed a similar route, however started from 1,2-difluoro-4,5-diaminobenzene. This was reacted with thionyl chloride in the presence of triethylamine as a base to produce 5,6-difluoro-2,1,3-benzothiadiazole (2).⁸⁷ This was subsequently brominated using *N*-bromosuccinimide,⁸⁷ coupled with 2-trimethylstannyl thiophene to give the fluorinated dithienyl-benzothiadiazole (6),^{88,89} and lithiated and stannylated as in the synthesis of 5 to produce 7.^{88,89}



Scheme 2.1 Synthetic routes towards the Stille reagents used in polymerization reactions with dibromobisisoindigo. Detailed synthetic procedures and characterization data are given in Chapter 5.

Polymers P1(H) and P2(F) were synthesized using Stille reactions with $\text{Pd}_2(\text{dba})_3$ and $\text{P}(o\text{-tolyl})_3$ as the catalyst system, as shown in Scheme 2.2. Synthetic routes towards the synthesis of a Stille reagent for preparation of P3(B) were unsuccessful, so a commercially available boronic ester functionalized benzothiadiazole was used instead to produce P3(B) using the Suzuki reaction. Typically, Suzuki reactions require the use of a base to activate the boronic ester, however it was found that this led to decomposition of the dibromobisisoindigo starting material, presumably through a base-catalysed retro-aldol reaction of the exocyclic double bonds within bisoindigo. As an alternative, cesium fluoride was used to activate the boronic esters, as this has been previously reported as a method for performing base free Suzuki coupling reactions.^{15,17,90,91} After Soxhlet purification polymers P1(H) and P2(F) were blue-black solids with reasonable solubility in chlorinated organic solvents, while P3(B) was slightly more purple in color and displayed lower solubility.

Table 2.1 Molecular weight data and decomposition temperatures of synthesized polymers.

Polymer	M_w (kDa) ^a	\bar{D} ^a	M_w (kDa) ^b	\bar{D} ^b	T_{Decomp} (°C) ^c
P1(H)	19.4	3.40	57.8	3.83	358
P2(F)	18.5	3.24	51.8	3.01	345
P3(B)	3.9	1.68	-	-	277

^a Molecular weights and dispersities determined by GPC with retention times calibrated relative to polyethylene standards. ^b Molecular weights and dispersities determined by GPC with retention times calibrated relative to polystyrene standards. All GPC measurements were performed using solutions of polymers dissolved in 1,2,4-trichlorobenzene at 130 °C. ^c Decomposition temperatures reported as the 5% weight loss temperature from thermal gravimetric analysis.

Thermal gravimetric analysis showed that both Stille synthesized polymers (P1(H) and P2(F)) have high thermal stability with decomposition temperatures near 350 °C, while P3(B) decomposed at a much lower temperature as a result of its lower molecular weight (Table 2.1, Figure 2.1 a). Differential scanning calorimetry for the three materials showed no phase changes or glass transitions under a heat-cool-heat cycle from room temperature up to 250 – 300 °C, staying below the decomposition temperature for each material (Figure 2.1 b).

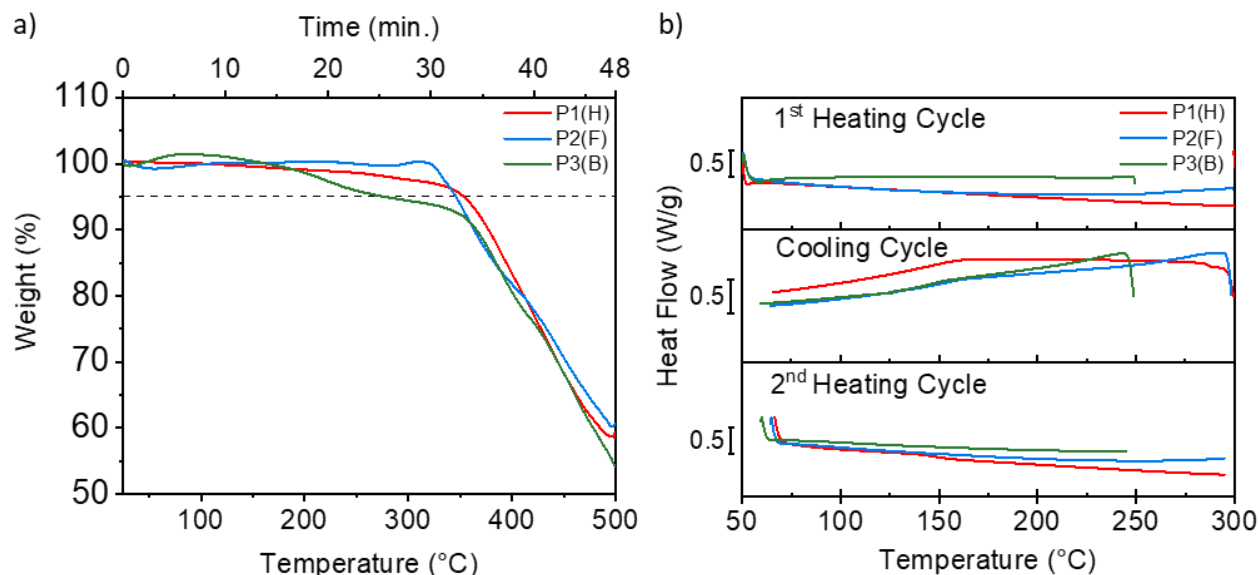


Figure 2.1 a) Thermal gravimetric analysis used to determine the polymer decomposition temperatures. The dashed grey line indicates a weight loss of 5%. b) Differential scanning calorimetry of the three polymer samples through a heating-cooling-heating cycle. Heating cycles were performed at 20 °C/minute.

2.2.3 DFT Optimized Polymer Structures

Density functional theory calculations were performed at the ω B97XD/6-31+g(d,p) level of theory and were used to obtain optimized structures of oligomers with alkyl chains truncated to methyl groups to simplify the calculations. Optimized oligomer structures are shown in Figure 2.2 and show that the bisisoindigo structure is not completely coplanar. The exocyclic carbon-carbon double bond in bisisoindigo is twisted due to steric repulsion between the amide oxygen and the neighboring hydrogen atom. This results in a twist at this bond, giving an average dihedral angle of 17° in both polymers. This finding agrees well with results from Onwubiko et al.²⁴ who observed an 18° angle at the same position in related polymers based on an extended ring fused isoindigo system. Fluorination in P2(F) was observed to decrease the average thiophene-benzothiadiazole dihedral angle from 19° to 5° , suggesting the presence of a non-covalent interaction between the thiophene sulfur and benzothiadiazole fluorine atom, as previously observed in other dithienyl-benzothiadiazole containing polymers.⁹²

The optimized structures for P1(H) and P2(F) (Figure 2.2 a, b) both resulted in the dithienyl-benzothiadiazole unit being axisymmetric rather than having the thiophenes oriented centrosymmetrically. Previously reported crystal structures for dithienyl-benzothiadiazoles have shown examples where the flanking thiophenes are either oriented in the same or opposite directions.^{93,94} These conformations lead to different conjugated backbone shapes to give either a pseudo-linear or curved polymer structure (Figure 2.2 d).^{93,95} As both of these materials are modelled to exist predominantly in the axisymmetric conformation, a curved polymer backbone is predicted, as seen in Figure 2.2 a) and b). In contrast to these materials, P3(B) can have only one possible orientation due to the para substitution of the benzothiadiazole, leading to a more linear polymer backbone shape. The combination of the twisted bisisoindigo core and the curved backbone from the dithienyl-benzothiadiazole units in P1(H) and P2(F) are predicted to give helical-type structures in these polymers, which could impact their packing in thin films relative to the more linear P3(B). The non-planar and curved polymer geometries predicted here help explain the lack of distinct thermal events in differential scanning calorimetry, as more disordered polymer packing would make phase changes more difficult to observe.

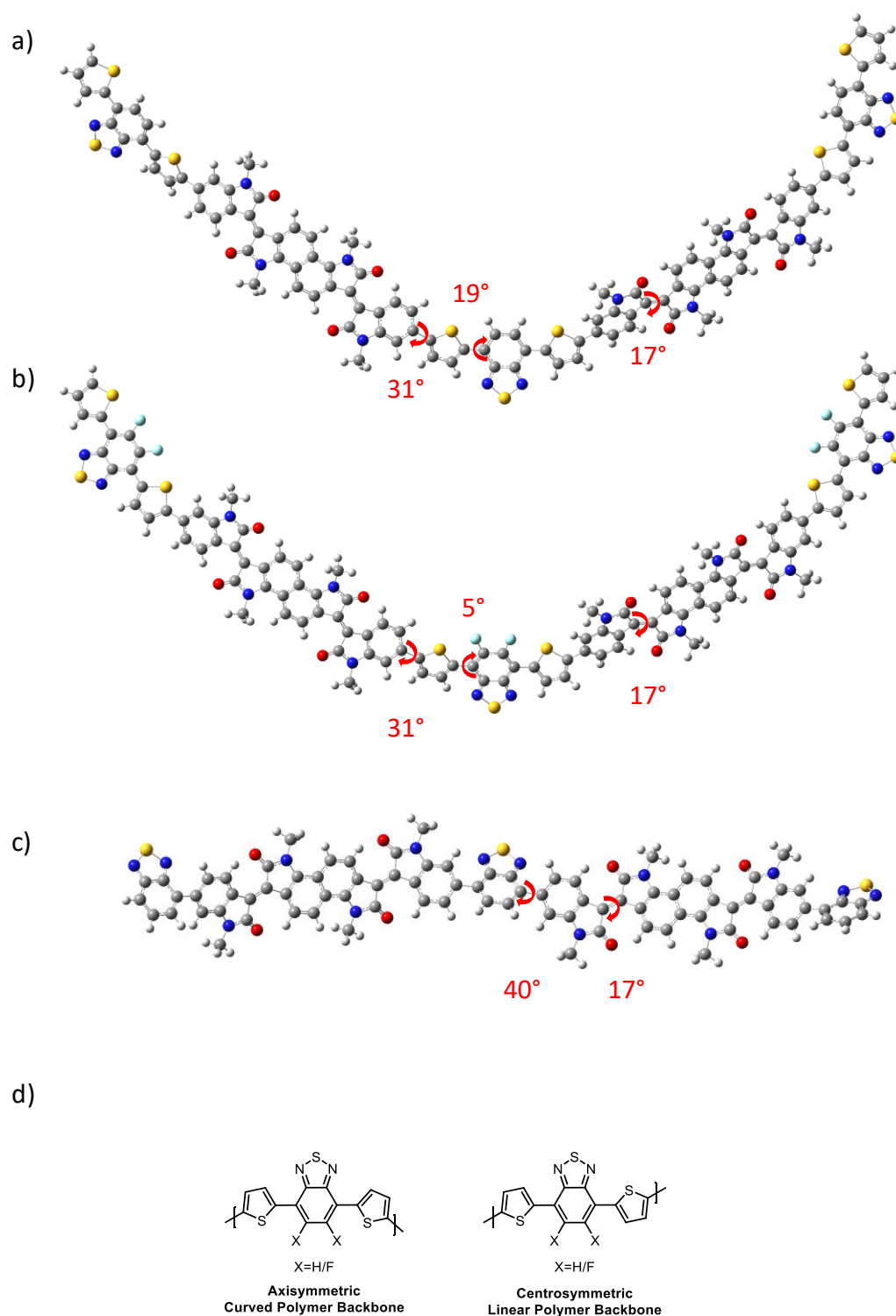


Figure 2.2 Structures of DFT optimized oligomers representing a) P1(H) b) P2(F) c) P3(B). Indicated bond angles represent average dihedral angles for the same position in each repeat unit. d) Potential orientations of the dithienyl-benzothiadiazoles in P1(H) and P2(F).

2.2.4 Polymer Optoelectronic Properties

The optical properties of the three polymers were characterized using UV/Vis spectroscopy both in chloroform solution and on spin-coated thin films (Figure 2.3 a). All materials show broad absorption bands that extend out to 1000 nm as a result of the extended conjugation of bisisoindigo. In comparing the solution spectra to the thin films, there is a slight redshift in the absorption onset indicating some J-aggregation in the solid state. Thermal annealing of the polymer thin films was observed to not have a significant effect on the UV/Vis absorption profiles. The solution-to-film redshift is in contrast to work by Jiang et al.⁷⁹ who observed slight blueshifts for similar bisisoindigo polymers when comparing *o*-dichlorobenzene solution and thin film UV/Vis. The polymers in the work by Jiang et al.⁷⁹ had longer alkyl chains and an alkene spacer in the place of the benzothiadiazoles in P1(H) and P2(F). This suggests that the benzothiadiazole unit may be impacting the packing of these polymers in thin films. Supporting this is the fact that the thiophene-alkene-thiophene unit in the reported polymers displayed a centrosymmetric geometry leading to more linear polymer chains based on DFT calculations, as opposed to the more bent structures predicted in the DFT calculations for the polymers in this project.⁷⁹

Due to the structural and spectral similarities of P1(H) and P2(F), time-dependent density functional theory (TD-DFT) calculations were performed to model the optical transitions of both polymers. TD-DFT calculations were performed at the ω B97XD/6-31G+(d,p) level of theory to model the UV/Vis absorption spectra based on oligomers of each polymer with two repeat units (Figure 2.3 b). Qualitatively, the calculated and experimental spectra match quite well in that they have four regions of strong absorption transitions, and the calculated transitions produce a similarly shaped spectra when fit with Gaussian peak shapes. Notably, the calculated energies of each transition are higher than observed experimentally for each region of strong absorption, as seen in the lower calculated absorption onset. This is not entirely unexpected for the ω B97XD functional, as its calculated energy levels scale relatively accurately with the number of polymer repeat units.⁹⁶ As only oligomers of two repeat units could be modelled with TD-DFT at this level of theory, polymers of increased lengths would be expected to have longer conjugation and smaller bandgaps. This is supported by TD-DFT calculations on longer oligomers run using B3LYP functional. These calculations produced spectra with absorption onsets at lower energies, matching more closely with the energies observed experimentally (Figure 5.5).

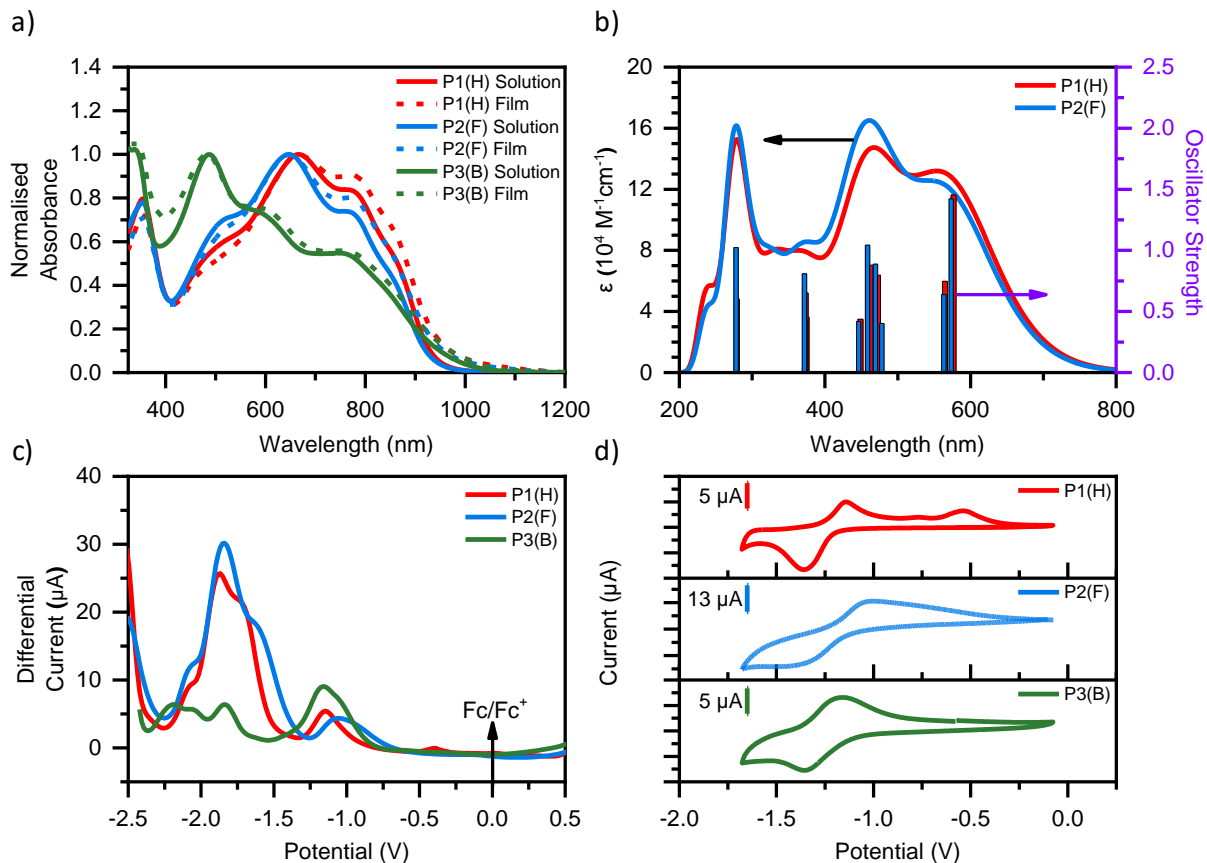


Figure 2.3 a) UV/Vis absorption spectra for the three synthesized polymers in CHCl_3 solution and as spin coated thin-films. b) TD-DFT simulated UV/Vis spectra for polymers P1(H) and P2(F). Extinction coefficients for the simulated spectra are shown on the left axis (in black) and oscillator strengths of the main contributing excitations are displayed as bars and correspond to the right axis (in purple). c) Differential pulse voltammetry scans of the three polymers. d) Cyclic voltammetry for the three studied polymers using a scan rate of 100mV/s.

Examination of the molecular orbital isosurfaces involved in each transition determined by TD-DFT can indicate which structural features are involved in each transition in the simulated UV/Vis spectra. The low energy transitions near 575 nm in the TD-DFT spectra predominantly represent HOMO to LUMO $\pi \rightarrow \pi^*$ transitions involving orbitals localized to the bisoindigo structure (Figure 5.6). In the fluorinated P2(F), there is also a slight contribution corresponding to a charge transfer to bisoindigo from the electron-deficient benzothiadiazole and region around the bisoindigo exocyclic carbon-carbon double bond. In the region around 475 nm in the calculated spectra there are many peaks closely spaced which correspond to a variety of transitions of different origins. The peaks appearing near 375 nm correspond to two different transitions, mainly corresponding to transitions localized to the bisoindigo structure. There is also increased

contribution from a charge transfer from the electron rich thiophene and naphthalene structure towards the benzothiadiazole in P2(F). Comparing these observations to the experimental spectra, the interpreted TD-DFT data suggests that the fluorinated benzothiadiazole in P2(F) leads to decreased absorption in the spectral shoulder near 800 nm caused by decreased charge transfer from this electron poor region. Similarly, the electron withdrawing fluorine atoms aid in charge transfer towards the benzothiadiazole, slightly increasing the absorption intensity in the peak shoulder near 500 nm.

Frontier molecular orbital energies for the polymers were estimated using a combination of UV/Vis spectroscopy differential pulse voltammetry (DPV) (Figure 2.3 c, Table 2.2). The first reduction peaks in DPV were used to estimate the polymer LUMO energy levels. As no oxidation peaks were observed within the solvent window, the HOMO energy was estimated by subtracting the thin film UV/Vis bandgap from the LUMO energy. Notably, all polymers have LUMO energy levels around -4.0 eV, indicating they should allow for stable electron transport. Similar LUMO energies were estimated by cyclic voltammetry (Figure 2.3 d), however the first reduction peaks are quasi-reversible and quite broad, making accurate analysis challenging. It appears that in P1(H) the first reduction event when moving to more negative potentials is followed by two oxidation events in the positive sweep, which suggests that the first reduction may be a two-electron process. As in the DPV data, oxidation peaks at positive potentials corresponding to removal of an electron from the HOMO were not observed in cyclic voltammetry when scanning to positive potentials.

Table 2.2 Optoelectronic properties obtained from UV/Vis spectroscopy and electrochemistry.

Polymer	$E_{g,opt}$ (eV) ^a	E_{LUMO} (eV) ^b	E_{HOMO} (eV) ^c
P1(H)	1.29	-3.95	-5.24
P2(F)	1.29	-4.04	-5.33
P3(B)	1.23	-3.97	-5.23

^a Determined from absorption onset in the thin film UV/Vis spectra. ^b Estimated from the first reduction peak in the differential pulse voltammogram; voltammograms were referenced to the Fc/Fc⁺ redox couple, which was assumed to be -5.1 eV relative to vacuum.

^c E_{HOMO} estimated as $E_{LUMO} - E_{g,opt}$.

The obtained HOMO and LUMO energies are lower than what has been previously observed in bisisoindigo donor-acceptor polymers as a result of the more acceptor rich design.^{79,80} The comparison between P1(H) and P3(B) shows that the thiophene rings do not significantly affect

the HOMO and LUMO energy levels in these polymers. Fluorination in P2(F) lowers the LUMO energy relative P1(H); however, because the LUMO is only slightly delocalized onto the benzothiadiazole containing units (Figure 5.6), the reduction is less significant than what is observed in donor-acceptor polymers. For example, fluorination of benzothiadiazoles can lower the measured LUMO energy by 0.2-0.3 eV,^{97,98} while the difference in LUMO energies is estimated at about 0.1 eV in these polymers. This suggests that the bisoindigo and dithienyl-benzothiadiazole units have comparable acceptor strengths, which is unsurprising as isoindigo and benzothiadiazole are considered to have similar acceptor strengths.⁹⁹ Interestingly, in the calculated orbital isosurfaces (Figure 5.4), P1(H) and P2(F) feature large HOMO and LUMO isosurfaces predominantly localized to the bisoindigo unit, while the benzothiadiazoles contribute to other molecular orbitals. This contrasts with donor-acceptor polymers which typically have the HOMO localized to the donor unit and the LUMO localized to the acceptor unit.

2.2.5 Polymer Thin Film Morphologies

Grazing incidence wide angle X-ray scattering (GIWAXS) was used to study polymer thin film morphologies. Polymer films were spin-coated from chloroform onto single crystal Si wafers and scattering patterns collected for both as-cast films and films after 20 minutes of thermal annealing at 200 °C (Figure 2.4). All thin films gave relatively weak scattering patterns as a result of fairly disordered solid-state packing, similar to what has been observed previously for other bisoindigo polymers.^{79,80} A weak scattering ring is observed at $q \sim 0.30 \text{ \AA}^{-1}$ in the as-cast films corresponding to the (100) lamellar spacing of the polymer chains (assuming orthorhombic packing). In the thermally annealed samples this feature becomes more prominent near the q_z and q_x axes due to reorganization of the films. After annealing, the q values of 0.30 \AA^{-1} and 0.31 \AA^{-1} for P1(H) and P2(F) correspond to d-spacings of 21 Å and 20 Å respectively. These lamellar d-spacings correspond well to what is seen in the literature for bisoindigo polymers with the same length alkyl chains,⁸⁰ while longer alkyl chains in other studies gave larger lamellar d-spacing values.⁷⁹ The scattering pattern for P3(B) after thermal annealing is noticeably different, with $q = 0.39 \text{ \AA}^{-1}$ for the lamellar peak, corresponding to a d-spacing of 16 Å, significantly smaller than the spacing observed for P1(H) and P2(F). Tabulated q values and d-spacings are given in Table 2.3.

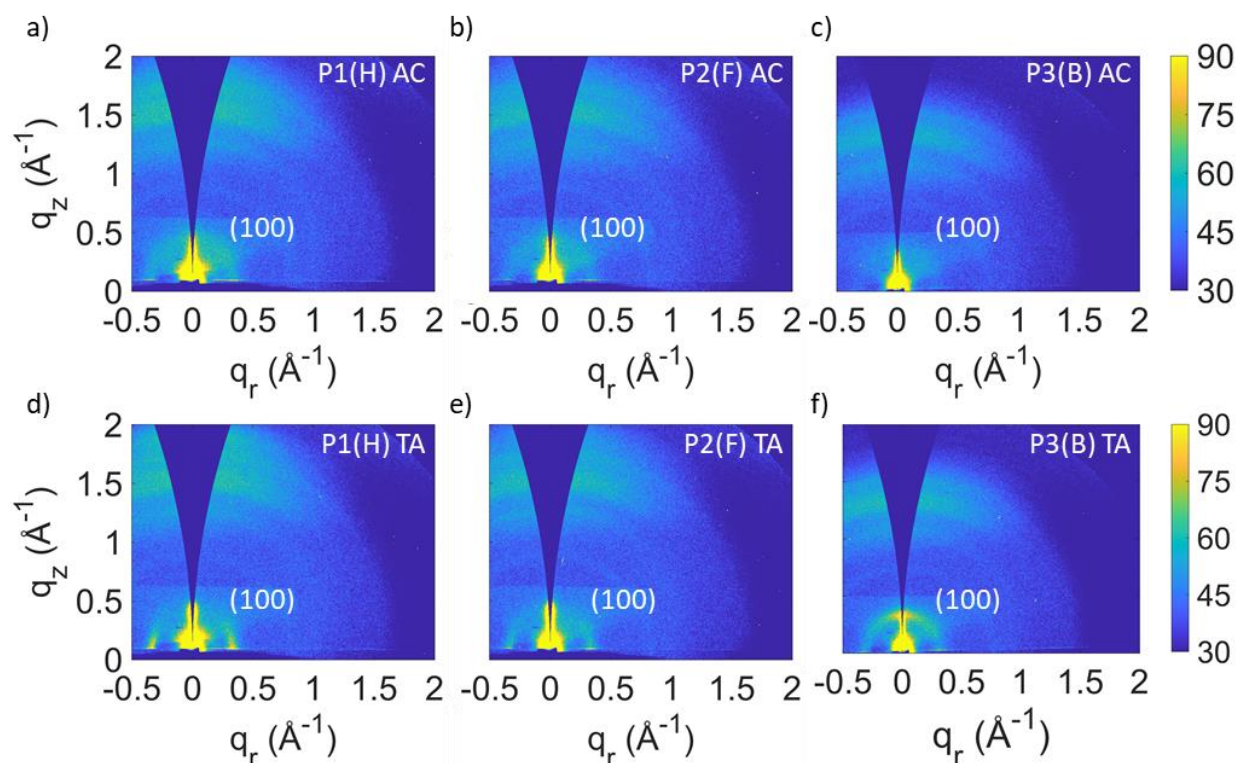


Figure 2.4 GIWAXS patterns of spin-coated polymer thin films for a) as-cast P1(H), b) as-cast P2(F), c) as-cast P3(B), d) thermally annealed P1(H), e) thermally annealed P2(F), and f) thermally annealed P3(B).

Table 2.3 Tabulated q values and d-spacings for lamellar peaks in the polymer GIWAXS patterns.

Polymer	q (\AA^{-1}) ^a	Lamellar d-spacing (\AA)	Polymer Shape ^b
P1(H)	0.30	21	Curved
P2(F)	0.31	20	Curved
P3(B)	0.39	16	Linear

^a q values obtained from scattering rings in the thermally annealed GIWAXS patterns (Figure 2.4 d – f). ^b Polymer shapes determined through DFT structural optimizations in Section 2.2.3.

The difference in d-spacing between the different polymers can be correlated with the polymer backbone shapes discussed earlier in Section 2.2.3. Both P1(H) and P2(F) show similar d-spacings for the lamellar stacking and were modelled to give curved polymer backbones based on the axisymmetric orientation of the dithienyl-benzothiadiazoles. In contrast P3(B) displayed smaller d-spacing distances and a more linear polymer backbone shape. This suggests that the benzothiadiazole containing units are affecting the packing of these polymers in a similar way to the isoindigo donor-acceptor polymers reported by Lei et al.⁶⁰ where axisymmetric donor units led

to curved polymer backbones and more disordered packing in thin films. The curved polymer backbone shape results in the polymers alkyl chains branching off at irregular angles and preventing polymer chains from ordering as strongly, resulting in the larger observed d-spacing values. Scattering peaks due to π - π stacking were not clearly identified due to the large amount of diffuse scattering at $q \sim 1.6 \text{ \AA}^{-1}$, where they are predicted to appear based on previous literature.^{79,80} The lack of a resolved π - π stacking feature could also be related to the non-linear and twisted polymer structures, which limits the ordering of the polymer stacking. This observation is also consistent with the differential scanning calorimetry data as well as the DFT optimized structures.

Texture analysis of the lamellar scattering peaks was used to determine orientation of the polymers relative to the substrate (Figure 2.5). In the as-cast films, all polymers showed little variation in scattering intensity as a function of the azimuthal angle χ , indicating little to no preferred orientation. With thermal annealing of P1(H) and P2(F) an increase in scattering intensity is observed at both high and low χ angles, indicating a mixture of edge-on and face-on orientation of the polymer packing relative to the substrate. In contrast, P3(B) showed increased scattering after annealing, however there was no significant orientation of this sample relative to the substrate, likely due to its low molecular weight. It qualitatively appears that there is stronger scattering intensity for the thermal annealed P1(H) films compared to P2(F), particularly at the lamellar scattering ring, suggesting slightly increased crystallinity in this polymer (Figure 2.4, 2.6 a).

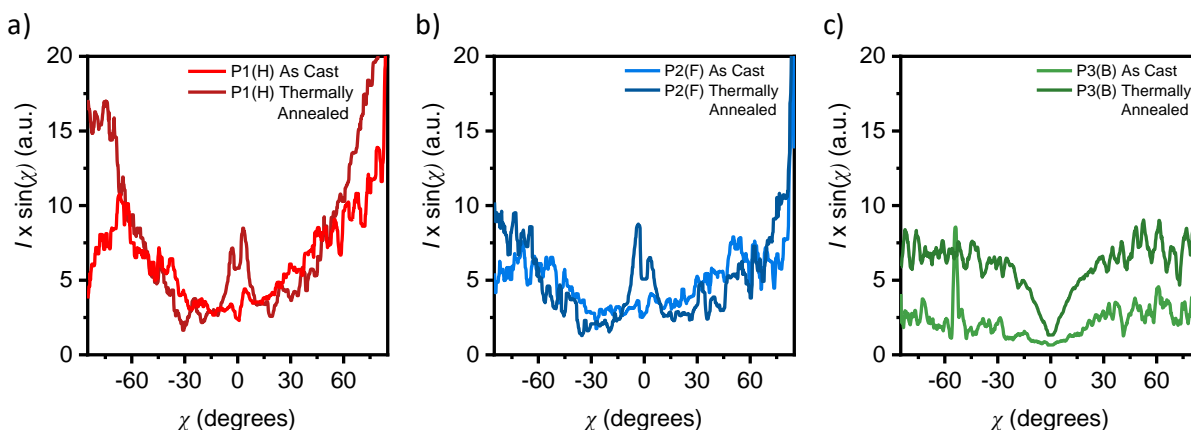


Figure 2.5 Texture analysis of the lamellar stacking feature ($q = 0.30 - 0.39 \text{ \AA}^{-1}$) in GIWAXS patterns before and after thermal annealing for polymers a) P1(H), b) P2(F) and c) P3(B). Analysis performed for azimuthal angles from -85° to 85° .

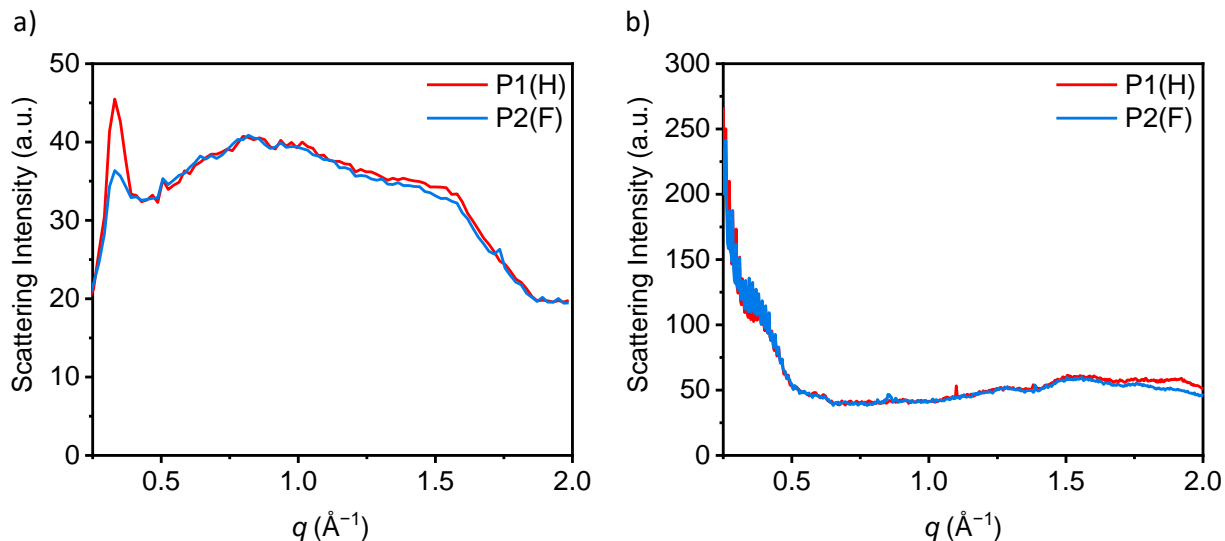


Figure 2.6 Line cuts of GIWAXS scattering patterns for thermally annealed polymer films of P1(H) and P2(F) taken along a) the q_r or b) the q_z axis.

2.2.6 OFET Device Performance

All polymers were used as the semiconducting layer in OFETs using the bottom-gate bottom-contact (BGBC) geometry. Devices were fabricated using a silicon wafer as the gate electrode, a thermally grown SiO_2 dielectric layer and a pair of Au contacts as the source and drain electrodes. Polymers were spin-coated from chloroform solutions and thermally annealed at different temperatures prior to testing. Devices with P1(H) and P2(F) showed ambipolar performance with balanced hole and electron mobilities (Table 2.4). Devices manufactured with P3(B) as the semiconductor layer were found to be non-functional. This is possibly the result of poor film morphology or a film that is too thin as a result of the lower solubility of this polymer, as solutions were syringe filtered prior to spin coating. Alternatively, the low molecular weight and dispersity of the polymer sample could have hampered charge injection into the organic material. Representative output and transfer curves for P1(H) and P2(B) are shown in Figure 2.7.

Thermal annealing results in improved charge carrier mobilities for both p-channel and n-channel device operation, likely resulting from more ordered film morphologies as observed in the GIWAXS patterns (Figure 2.4). Optimal annealing temperatures were found to be 100 °C for P1(H) and 200 °C for P2(F) as these produced the highest average charge carrier mobilities. Both polymers in BGBC devices had better hole mobilities than electron mobilities. The best hole mobility was achieved by P1(H) ($4.0 \times 10^{-3} \text{ cm}^2 \text{ V}^{-1} \text{ s}^{-1}$) while the best electron mobility (5.0×10^{-4}

$\text{cm}^2 \text{V}^{-1} \text{s}^{-1}$) was achieved in P2(F). This suggests that the more electron withdrawing fluorinated benzothiadiazole unit may be aiding in electron transport. The degree of order in the polymer thin film likely also impacts the measured charge carrier mobility values. In a study of a series of isoindigo donor-acceptor polymers Lei et al.⁶⁰ found that using axisymmetric donors led to curved polymer backbones, which resulted in more disordered packing and reduced charge carrier mobilities relative to linear polymers. As the polymers reported here had curved back-bones resulting from axisymmetric dithienyl-benzothiadiazole units, this suggests that more centrosymmetric electron-deficient units paired with bisisoindigo could lead to OFET materials with improved charge carrier mobilities in the future.

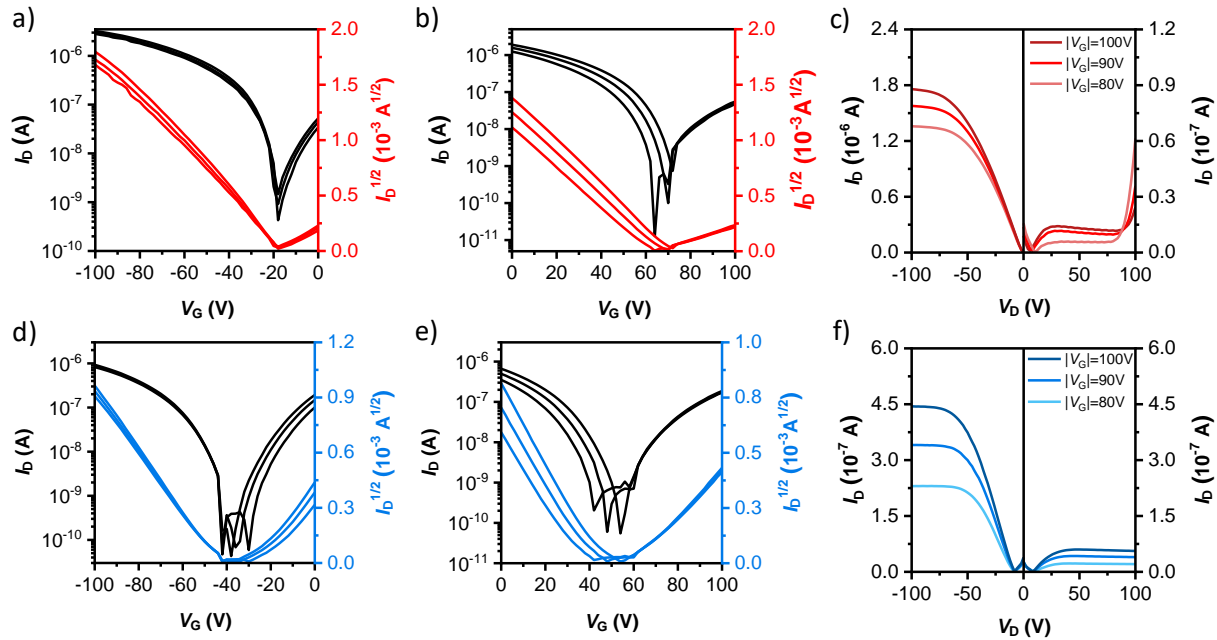


Figure 2.7 Transfer and output curves for BGBC, Au source/drain OFET devices. a) P1(H) p-channel transfer curves with V_D ranging from -80 to -100 V. b) P1(H) n-channel transfer curves with V_D ranging from 80 to 100 V. c) P1(H) output curves. d) P2(F) p-channel transfer curves with V_D ranging from -80 to -100 V. e) P2(F) n-channel transfer curves with V_D ranging from 80 to 100 V. f) P2(F) output curves.

Table 2.4 OFET device performance of P1(H) and P2(F) polymers using BGBC architecture and Au source and drain electrodes.

Polymer	T (°C) ^a	N ^b	μ_h (cm ² V ⁻¹ s ⁻¹) ^c	μ_e (cm ² V ⁻¹ s ⁻¹) ^c	V_T (p-/n-channel) ^d		$I_{on/off}$ (p-/n-channel) ^d	
P1(H)	N/A	5	$(1.6 \pm 0.4) \times 10^{-3}$	$(1.5 \pm 0.3) \times 10^{-4}$	-25±2	68±2	10 ⁴	10 ²
		Best	2.1×10^{-3}	1.8×10^{-4}				
	50	5	$(1.9 \pm 0.6) \times 10^{-3}$	$(1.7 \pm 0.5) \times 10^{-4}$	-20±3	69±1	10 ⁴	10 ²
		Best	2.7×10^{-3}	2.6×10^{-4}				
	100	5	$(3 \pm 1) \times 10^{-3}$	$(2.2 \pm 0.9) \times 10^{-4}$	-18±3	66±3	10 ³	10 ²
		Best	4.0×10^{-3}	3.5×10^{-4}				
	150	5	$(1.9 \pm 0.4) \times 10^{-3}$	$(1.8 \pm 0.3) \times 10^{-4}$	-24±3	65±3	10 ⁴	10 ²
		Best	2.4×10^{-3}	2.1×10^{-4}				
	200	5	$(2.8 \pm 0.7) \times 10^{-3}$	$(2.2 \pm 0.6) \times 10^{-4}$	-33±3	62±3	10 ³	10 ²
		Best	3.6×10^{-3}	2.9×10^{-4}				
P2(F)	N/A	5	$(5.2 \pm 0.8) \times 10^{-4}$	$(7 \pm 1) \times 10^{-5}$	-41±1	66±1	10 ⁴	10 ²
		Best	6.4×10^{-4}	8.4×10^{-5}				
	50	5	$(8.5 \pm 0.3) \times 10^{-4}$	$(1.3 \pm 0.1) \times 10^{-4}$	-27±1	62±2	10 ⁴	10 ³
		Best	1.0×10^{-3}	1.5×10^{-4}				
	100	5	$(7.8 \pm 0.2) \times 10^{-4}$	$(2.5 \pm 0.4) \times 10^{-4}$	-29±4	64±3	10 ⁴	10 ²
		Best	9.7×10^{-4}	3.0×10^{-4}				
	150	5	$(7.0 \pm 0.1) \times 10^{-4}$	$(2.5 \pm 0.6) \times 10^{-4}$	-35±5	63±3	10 ⁵	10 ³
		Best	8.0×10^{-4}	3.1×10^{-4}				
	200	5	$(1.0 \pm 0.3) \times 10^{-3}$	$(3.5 \pm 0.1) \times 10^{-4}$	-40±3	60±3	10 ⁴	10 ³
		Best	1.5×10^{-3}	5.0×10^{-4}				

^a Devices thermally annealed for 20 minutes at specified temperature in inert atmosphere glovebox.

^b Number of devices used to determine average mobilities along with best performing device.

^c Mobilities determined from saturation region. ^d Average results displayed for threshold voltage and on/off current ratios.

It was noted that the observed threshold voltages for BGBC devices were quite high, ranging from -20 to -40 V for p-channel operation and 60 to 70 V for n-channel operation. This is problematic for the production of OFET devices with low power consumption, as is desirable for lightweight or wearable electronics.¹⁰⁰ Threshold voltages can be impacted by the morphology of the polymer film, impurities and trap states within the film, as well as the energy level alignment

between the Fermi level of the source and drain electrodes and the frontier molecular orbitals of the polymer. To improve the threshold voltages for n-channel operation, OFETs with the bottom-gate top-contact (BGTC) architecture with LiF/Al source and drain contacts were fabricated. As electrons are injected into the polymer LUMO for n-channel operation, it was hypothesized that the similar LUMO energies of the polymers (-3.95 or -4.04 eV) and contact Fermi energy (-4.2 eV)¹⁰¹ would result in improved threshold voltages in these OFETs. The device performance metrics for these OFETs are displayed in Table 2.5 and representative output and transfer curves in Figure 2.8.

Table 2.5 OFET device performance of P1(H) and P2(F) polymers using BGTC architecture and LiF/Al source and drain electrodes.

Polymer	T (°C) ^a	N ^b	μ_h (cm ² V ⁻¹ s ⁻¹) ^c	μ_e (cm ² V ⁻¹ s ⁻¹) ^c	V_T (p-/n-channel) ^d		$I_{on/off}$ (p-/n-channel) ^d	
P1(H)	100	5	N/A	$(8 \pm 4) \times 10^{-4}$	N/A	5±2	N/A	10
		Best	N/A	1.4×10^{-3}				
P2(F)	100	5	N/A	$(2.7 \pm 0.4) \times 10^{-4}$	N/A	15±6	N/A	10^2
		Best	N/A	3.3×10^{-4}				

^a Devices thermally annealed for 20 minutes at specified temperature in inert atmosphere glovebox.

^b Number of devices used to determine average mobilities along with best performing device.

^c Mobilities determined from saturation region. ^d Average results displayed for threshold voltage and on/off current ratios.

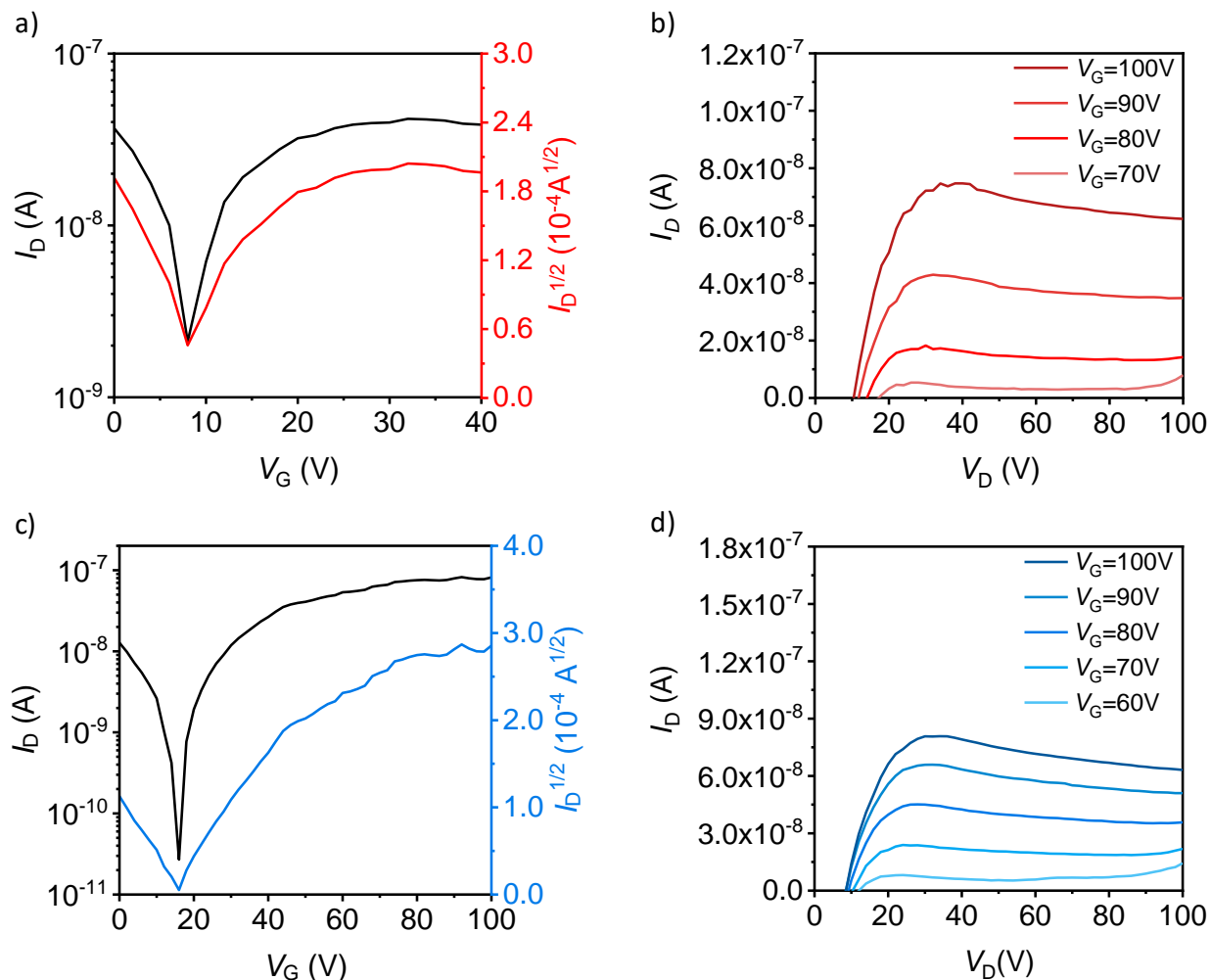


Figure 2.8 Transfer and output curves for BGTC, LiF/Al source/drain OFET devices. a) P1(H) n-channel transfer curves with V_D of 100 V. b) P1(H) output curves. c) P2(F) n-channel transfer curves with V_D of 100 V. d) P2(F) output curves.

The change in OFET architecture and source/drain contacts to the BGTC (LiF/Al) devices results in a significantly lower threshold voltage for both polymers. This suggests that the large threshold voltage in the Au source/drain devices was a result of poor matching between the polymer LUMO and metal Fermi energy, rather than the other potential causes discussed above. The improved energy level alignment results in threshold voltages of 5 ± 2 V for P1(H) and 15 ± 6 V for P2(F). These threshold voltages are significantly lower than what has been previously observed in bisisindigo polymers,^{79,80,102} core-expanded isindigo D-A polymers,^{69–71} or isindigo A-A polymers.^{62–64} The larger threshold voltage in the fluorinated polymer P2(F) is surprising when considering it has a lower LUMO energy than P1(H). This difference could be a result of poorer morphology of these films, as they appeared to be qualitatively less ordered in thin-film GIWAXS

patterns. Additionally it has been shown that fluorinated polymers may be unstable when in close proximity to Al electrodes,¹⁰³ which could further impact the polymer frontier molecular orbital energies, thin film morphology, or lead to the creation of additional trap states. Electron mobilities between the two architectures were similar for P2(F), while P1(H) showed an increased electron mobility with the LiF/Al electrodes, reaching up to $1.4 \times 10^{-3} \text{ cm}^2 \text{ V}^{-1} \text{ s}^{-1}$. Hole mobilities could not be measured as the devices were not operational as p-channel devices. Both polymers had a smaller $I_{\text{on/off}}$ ratio with the LiF/Al contacts, presumably due to lower currents from the addition of the resistive LiF layer. This suggests that using LiF/Al lowers $I_{\text{on/off}}$ ratios and possibly reduces device stability due to the more reactive Al electrodes, but allows for significant improvement in threshold voltage for n-channel OFETs. Additionally, this highlights the importance of proper selection of source and drain electrodes for the testing of new OFET materials.

2.3 Conclusions

In this chapter, two conjugated polymer design strategies were combined to produce new OFET materials. Pairing bisisoindigo, a core-expanded isoindigo derivative, with benzothiadiazole containing units gave acceptor-acceptor polymers that showed ambipolar OFET performance. In comparison to other bisisoindigo containing polymers, these materials had lower LUMO energies and more delocalized frontier molecular orbital isosurfaces as a result of the acceptor-rich structure. The low LUMO energies allowed for electron transport and resulted in ambipolar OFET performance with hole and electron mobilities up to $4.0 \times 10^{-3} \text{ cm}^2 \text{ V}^{-1} \text{ s}^{-1}$ and $1.4 \times 10^{-3} \text{ cm}^2 \text{ V}^{-1} \text{ s}^{-1}$ respectively. The orientation of the dithienyl-benzothiadiazole units was shown to impact the polymer backbone shape, in turn impacting the physical and optoelectronic properties of these polymers relative to previous bisisoindigo polymers. Additionally, this potentially affects the packing order in polymer thin films and the charge carrier mobilities measured in OFETs. This suggested that careful control of the symmetry of acceptor units could lead to improved charge carrier mobilities in future generations of isoindigo-based acceptor-rich polymers. Changing the OFET source and drain contacts from Au to LiF/Al resulted in a significant decrease in threshold voltage to $5 \pm 2 \text{ V}$, which is the result of improved energy alignment between the polymer LUMO and the metal Fermi energy. This reduced threshold voltage is lower than what is observed in most isoindigo based polymers and highlights the importance of source and drain contacts in testing new materials for OFETs.

Chapter 3 – Synthesis of Thiophene Dioxide Acceptors

Due to the limited number of electron-deficient acceptor units commonly used in organic semiconductors there is increasing interest in developing new acceptors to improve material properties and device performance. Additionally, acceptor units that are relatively easy to synthesize are advantageous, as this helps to shorten material development time and reduces manufacturing costs for organic electronics. This chapter is focused on the development of thiophene dioxide acceptor units for conjugated polymers. These methods use thiophene, ubiquitous in conjugated polymers and small molecules, as a starting material to simplify synthesis. Thiophene dioxides are strongly electron withdrawing and stabilize a quinoidal conjugated pathway through the resulting polymers,^{104,105} which may allow for improved electron transport through these materials.

3.1 Motivation for Thiophene Dioxides

Thiophene dioxides are interesting electron acceptor units because of their strongly electron withdrawing character. Previous examples in OPV and OFET materials have shown that the installation of a thiophene dioxide significantly decreases the LUMO energy level relative to the corresponding thiophene containing material.^{106–108} This makes thiophene dioxides well suited for building stable materials for n-channel OFETs. Additionally, oxidation of the thiophene sulfur atom disrupts the aromaticity of the thiophene ring, therefore removing the energetic barrier between the quinoidal and formerly aromatic resonance forms.¹⁰⁹ Stabilization of the quinoidal resonance form can help to lower the bandgap of the semiconductor and improve charge transport along a polymer chain. Despite the promise of this heterocycle, it has not yet been used extensively in conjugated polymers as it is challenging to functionalize properly for use in standard Stille and Suzuki coupling methods. Part of the reason for this synthetic challenge is the high reactivity of the thiophene dioxide; with the loss of aromaticity in the thiophene ring, the thiophene dioxide has increased reactivity towards Diels-Alder type cycloaddition chemistry, which leads irreversibly towards unwanted dimers.¹¹⁰

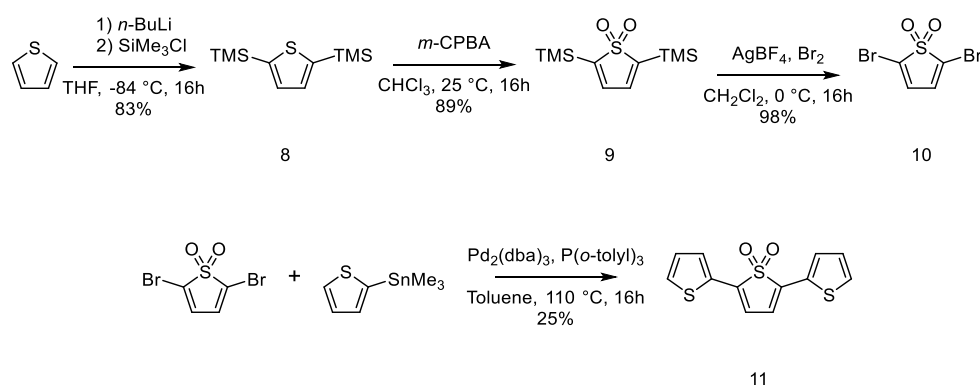
Much of the early work on the production of thiophene dioxides was performed by Barbarella et al.^{109,111–113} who showed that thiophene units could be converted to the corresponding thiophene dioxide using *m*-chloroperoxybenzoic acid (*m*-CPBA). This changes the electron-rich

thiophene unit to an electron-deficient structure. In the case of polythiophene oligomers it was shown that terminal thiophenes were oxidized preferentially over internal thiophenes. Importantly, all the thiophenes and polythiophenes studied needed to be functionalized in the 2 and 5' positions of the terminal thiophenes to prevent unwanted self reactivity of the oxidized product. Pappenfus et al.¹¹⁴ later reported that by installing butyl chains in the 3',4' positions of a the central thiophene in a terthiophene unit, the selectivity observed by Barbarella et al.^{109,111–113} was reversed and the internal thiophene dioxide was now predominantly formed. In this example the terthiophene units were also end capped to prevent unwanted dimerization upon oxidation as reported by Miller et al.¹¹⁵ Rozen's reagent ($\text{HOF}\cdot\text{CH}_3\text{CN}$) is an alternative oxidant to *m*-CPBA and contains an electrophilic oxygen atom.¹¹⁶ This is a very potent oxidizing agent and can be used to convert all thiophenes within a polythiophene to the corresponding thiophene dioxide, rather than the selective oxidations achieved with *m*-CPBA. The main issue with using Rozen's reagent is that it is produced by bubbling a corrosive F_2/N_2 gas mixture through a cooled mixture of acetonitrile and water, then titrated before use.¹¹⁷ The high toxicity of fluorine gas in this method significantly limits its broad application. Another method to produce a strong oxidizing agent for making thiophene dioxides involves the reaction of trifluoroacetic anhydride with 98-99% H_2O_2 , which has also not seen wide usage due to safety concerns associated with concentrated peroxides.^{118,119} With these examples in mind, a mild and safe route to thiophene dioxides that can be functionalized for Stille or Suzuki coupling methods is desirable. This chapter explores synthetic routes towards these intermediates, with the eventual goal of producing additional bisoindigo containing polymers that can be compared to those produced in Chapter 2.

3.2 Results and Discussion

3.2.1 Small Molecule Synthesis

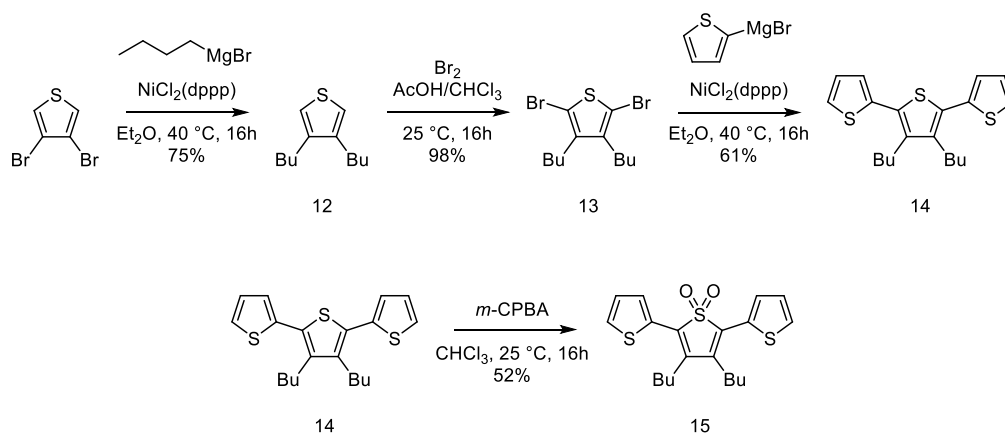
The initial synthetic target for this project was a terthiophene containing a central thiophene dioxide, as this would allow the synthesis of structurally similar polymers to P1(H) and P2(F) in Chapter 2. As the benzothiadiazole unit would be replaced by a thiophene dioxide the relative strength of these acceptors could be compared. Towards this goal, terthiophene-*S',S'*-dioxide was synthesized as shown in Scheme 3.1. The procedures for synthesis of 2,5-dibromo-*S,S*-thiophene dioxide (from thiophene through to product 10) were followed from Coombs et al.¹²⁰



Scheme 3.1 Synthesis of terthiophene-*S',S'*-dioxide.

Thiophene was first functionalized with trimethylsilyl groups in the 2,5 positions, which allowed oxidation by *m*-CPBA to the thiophene dioxide (9) without self reactivity of the product. Silver tetrafluoroborate was used to help deprotect the thiophene ring to allow for bromination. This intermediate (10) was then subjected to a Stille coupling to produce the desired terthiophene dioxide. The low yield in the reaction to produce the terthiophene dioxide (11) is consistent with the yield observed in similar catalytic systems,¹²¹ and so was not optimized further, but could be a result of coordination of the sulfone oxygen atoms to the palladium catalyst, slowing the catalytic cycle.

To convert the terthiophene dioxide (11) to a Stille reagent for polymerization, reactions with strong bases such as *n*-butyllithium (*n*-BuLi) and lithium diisopropylamide (LDA) were used to deprotonate the terthiophene in the 5,5'' positions. Subsequent reactions with trimethyltin chloride (SnMe₃Cl) were used to make the desired product, similar to reactions to make Stille reagents 5 and 7 in Chapter 2. Unfortunately, this strategy always resulted in a mixture of products that could not be sufficiently separated and purified to allow further use. It was hypothesized that the distribution of products was a result of low selectivity for the desired deprotonation, as hydrogens in the 3',4' positions of the central thiophene could also be deprotonated. Work performed by Leclerc et al.¹⁰⁸ had previously shown that deprotonation and stannylation could be performed at the 5,5'' positions if there were alkyl chains on the central thiophene in the 3',4' positions. Based on this a new synthetic route was used to produce a terthiophene dioxide with these butyl chains to prevent the unwanted deprotonations, as shown in Scheme 3.2.



Scheme 3.2 Synthesis of alkylated terthiophene dioxide.

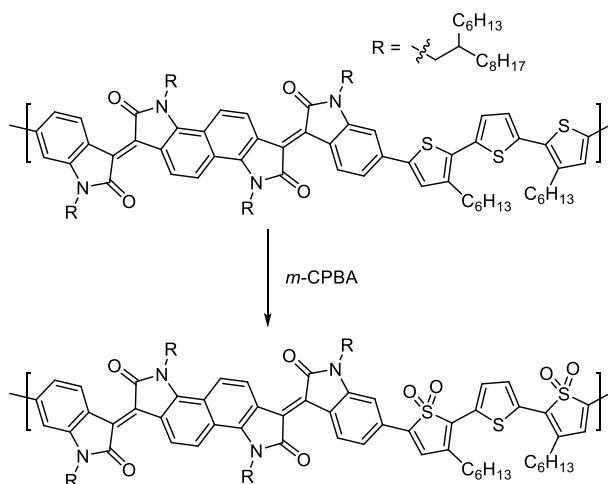
A Kumada coupling between 3,4-dibromothiophene and butylmagnesium bromide allowed for the installation of butyl chains onto thiophene. A bromination reaction followed by a second Kumada coupling with 2-thienylmagnesium bromide produced the alkylated terthiophene (14). This could be directly oxidized using *m*-CPBA to give the alkylated terthiophene dioxide (15) as in work by Pappenfus.¹¹⁴ Previously it was shown that terthiophene units were susceptible to dimerizing when oxidized to radical anions,¹¹⁵ and previous *m*-CPBA oxidations of polythiophenes had used end capping to prevent this type of coupling. As no dimerization was observed in the case of the oxidation of this terthiophene to the product (15), it can be presumed that this reaction does not proceed predominantly through a radical anion, and so end capping to prevent dimerization was unnecessary.

The same strategy was used to attempt to produce a Stille reagent by deprotonation of (15) and subsequent reaction with SnMe_3Cl to produce a Stille reagent for polymerization. Initial attempts followed the same procedure used by Leclerc et al.¹⁰⁸ reacting the terthiophene with LDA as the base at low temperatures, which led to no stannylated product. Increasing the reaction temperature led to some stannylated products, however not in sufficient quantity or purity. Switching from LDA to the more reactive, less bulky *n*-BuLi gave similar results. To try and improve product formation, *N,N,N',N'*-tetramethylethylenediamine (TMEDA) was used as an additive along with *n*-BuLi, as this has been shown to change the aggregation state of *n*-BuLi in solution to allow for faster reactions.^{122,123} Despite these efforts, none of the desired product was isolated.

With the lack of success in developing thiophene dioxide containing Stille reagents to be used in polymerizations, an alternate strategy was pursued using a post-polymerization oxidation reaction to produce thiophene dioxide polymers from previously reported thiophene containing polymers. This strategy can be used to install a desirable functionality that is difficult or impossible to install otherwise. Wei et al.¹²⁴ have used post-polymerization functionalization to modify thiophene containing polymers using Rozen's reagent. It was shown that the optical and electronic properties of the resulting polymers can be carefully tuned depending on the extent of the functionalization reaction by controlling the stoichiometry of the oxidant. Notably, this method uses the $\text{HOF} \cdot \text{CH}_3\text{CN}$ mixture that must be generated using fluorine gas, which limits its applications due to safety precautions, especially at large scales. As an alternative the safer, milder *m*-CPBA was used as the oxidizing agent to modify previously reported bisisoindigo polymers.

3.2.2 Post-Polymerization Functionalization

Post-polymerization modification was performed on a bisisoindigo-terthiophene (BII-3T) donor-acceptor polymer that had been previously studied in OPVs and OFETs.⁸⁰ It was predicted that oxidation using *m*-CPBA would lead to incomplete conversion to the oxidized product as seen previously.¹¹¹ Based on the selectivity observed by Barbarella et al.^{109,111–113} the two outer thiophenes would likely react while the central thiophene would most likely remain unreacted. Scheme 3.3 shows the predicted reactivity of this polymer with *m*-CPBA.



Scheme 3.3 Predicted reactivity for post-polymerization modification of bisisoindigo-terthiophene with *m*-CPBA.

It was predicted that successful oxidation to the thiophene dioxide product would lead to a decrease in the polymer bandgap, as is typical for comparison between a polythiophene and the corresponding thiophene dioxide.^{106,125} With this in mind the reaction of the polymer with *m*-CPBA was monitored over time using UV/Vis spectroscopy, with results shown below in Figure 3.1.

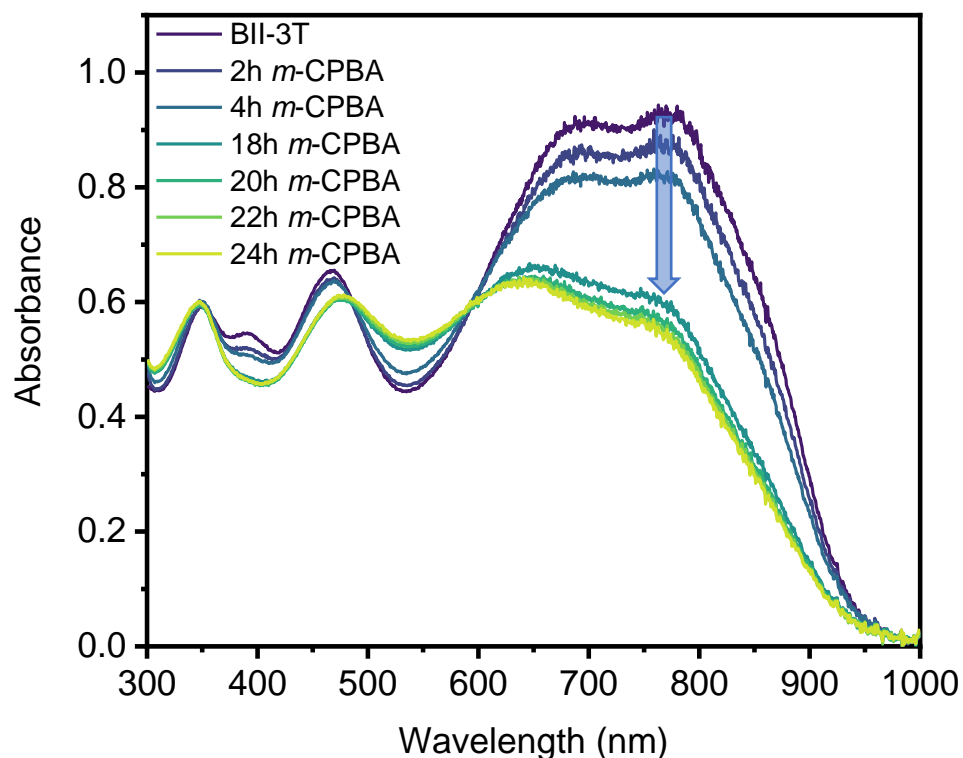


Figure 3.1 UV/Vis spectra of bisisoindigo-terthiophene reacting with *m*-CPBA as a function of time.

The bisisoindigo-terthiophene polymer was dissolved in dry chloroform under an inert argon atmosphere before addition of small amounts of an *m*-CPBA solution (in dry chloroform). No significant changes were observed in the UV/Vis spectra with increasing amounts of the peroxide until the addition of 6 equivalents of *m*-CPBA, at which point no more oxidant was added and spectra were collected periodically. Throughout the experiment the solution volume was kept constant to ensure comparable UV/Vis spectra. Throughout the experiment there was no increase in the absorption onset wavelength that was predicted with the introduction of the thiophene dioxides. Additionally, there was a significant decrease in the absorption between 600 and 900 nm

corresponding mainly to the HOMO to LUMO transition localized to bisisoindigo. This indicates that there could be reactivity between the bisisoindigo structure and the *m*-CPBA, resulting in a disruption of conjugation along the polymer chain. At approximately 600 nm there is an isosbestic point where the absorption remains constant, which usually indicates a conversion to one product with constant reaction stoichiometry. This suggests that despite there being a disruption of the conjugated pathway, there is not necessarily a fragmentation of the polymer itself.

To further study the transformation occurring upon reaction of the polymer with *m*-CPBA, infrared absorption spectra were taken of the polymer samples from both before and after the reaction, shown below in Figure 3.2.

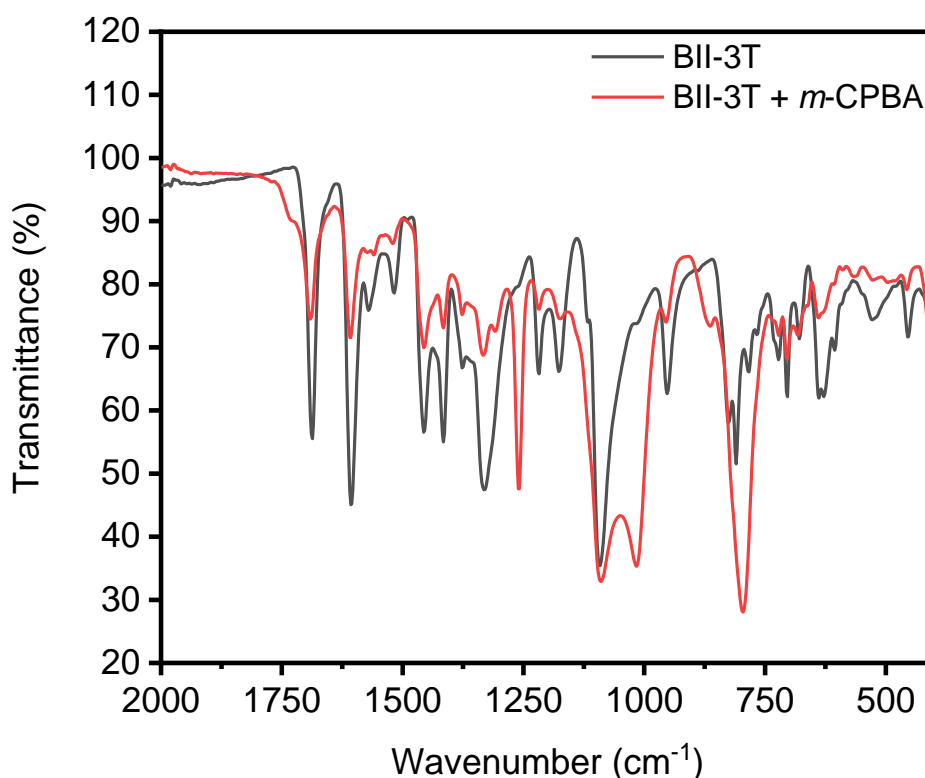


Figure 3.2 IR spectra of bisisoindigo-terthiophene copolymer before and after reaction with *m*-CPBA.

After the reaction there are three new stretching frequencies that appear quite prominently at 1260, 1017 and 795 cm⁻¹. These do not match with what is usually observed for sulfones (1315 and 1142 cm⁻¹)¹²⁴ or sulfoxides that could be present from incomplete oxidation (1074 cm⁻¹).¹²⁶ This suggests

that the major product from the reaction is not resulting from oxidation of the thiophene sulfur atoms to sulfones or sulfoxides. An alternative explanation for the new infrared stretching bands is the presence of epoxides within the polymer. Epoxidation of alkenes by *m*-CPBA is a well-known reaction in organic chemistry and could explain the new IR peaks. Epoxides have three characteristic stretching modes of ring breathing, symmetric ring deformation, and antisymmetric ring deformation.¹²⁷ The frequencies of these vibrations vary depending on the substituents attached to the carbon atoms making them not entirely reliable for conclusive identification, but fall into the ranges of 1248-1271 cm⁻¹ for ring breathing, 883-985 cm⁻¹ for antisymmetric deformation and 830-877 cm⁻¹ for symmetric ring deformation. While these ranges do not match exactly with the observed IR stretches for the oxidized polymer, the reference data relates only to small molecule epoxides, while the epoxides within the polymer could have slightly different IR stretches due to the large difference in substituents on the epoxides. Additionally, epoxidation of the exocyclic carbon-carbon double bond in bisisoindigo would lead to a break in the conjugation along the polymer chain which is consistent with the observed decrease in the absorption band near 750 nm in UV/Vis spectroscopy.

As an additional method to probe the oxidation reaction, X-ray photoelectron spectroscopy (XPS) was used to study the polymer both before and after the reaction with *m*-CPBA. Polymer samples were measured using an Al K- α (1486.6 eV) source for both survey spectra and sulfur 2p spectra. Fitted peaks from the sulfur 2p experiment are displayed below in Figure 3.3.

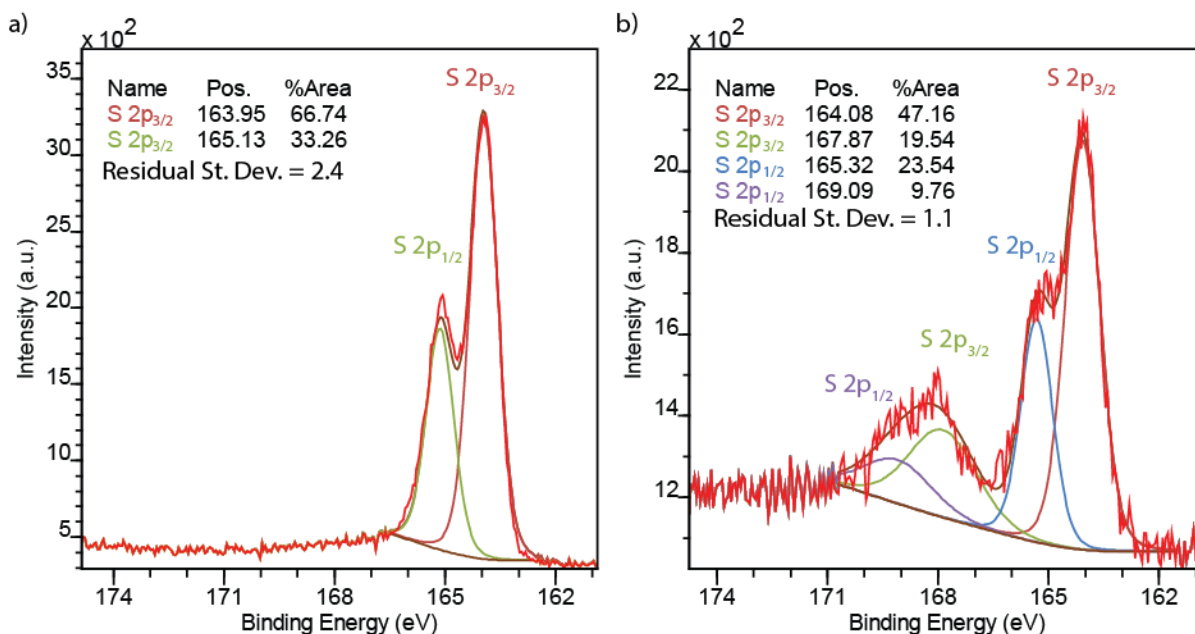


Figure 3.3 Fitted XPS spectra of the S 2p region for a) bisisoindigo-terthiophene polymer before and b) after reaction with *m*-CPBA.

Splitting peaks corresponding to the sulfur 2p_{3/2} and 2p_{1/2} are observed in both spectra at binding energies of approximately 164 and 165 eV. These binding energies match closely to those observed in other polythiophenes such as P3HT.¹²⁸ The spectra prior to oxidation (Figure 3.3 a) shows the expected 2:1 intensity ratio for the 2p_{3/2} and 2p_{1/2} fitted peaks. After the oxidation two new peaks are observed with binding energies of 167.87 and 169.09 eV. This matches well with binding energies observed for a variety of small molecule sulfones near 168 eV.¹²⁹ The installation of the electron withdrawing oxygen atoms in the sulfone leads to less shielding of the nuclear charge experienced by the sulfur core 2p electrons. This results in the higher binding energy relative to the sulfur atoms in the polymer prior to the reaction. The XPS data indicates that the reaction between the bisisoindigo-terthiophene polymer and *m*-CPBA likely produced a small amount of the desired sulfone product. Based on the peak areas in Figure 3.3 b) it can be roughly estimated that the oxidation reaction occurred on approximately 30% of the sulfur atoms within the polymer.

The appearance of a new XPS peak corresponding to the sulfone suggests that thiophene dioxides were formed to some extent in the reaction of the bisisoindigo-terthiophene polymer with *m*-CPBA. Other experiments using UV/Vis and infrared spectroscopy suggest that the main result of the reaction of the polymer with *m*-CPBA was the formation of epoxides, potentially at the exocyclic double bond within the bisisoindigo structure, rather than the desired thiophene

oxidation. Based on this information, a proposed polymer structure after oxidation that is consistent with all the experimental observations is shown below in Figure 3.4.

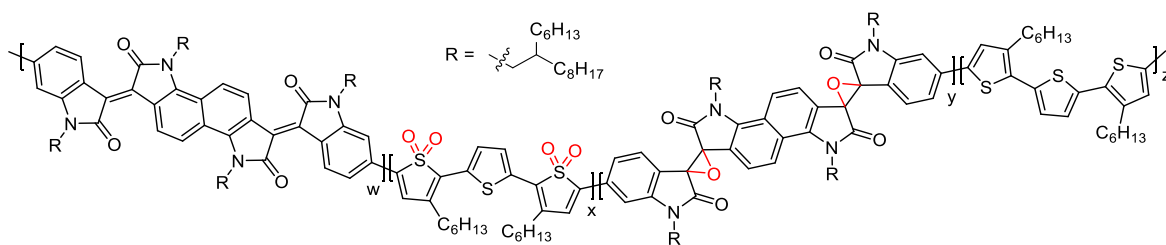


Figure 3.4 Representation of the bisoindigo-terthiophene polymer after reaction with *m*-CPBA featuring segments of the polymer chain with unreacted bisoindigo (w), oxidized terthiophene units (x), epoxide functionalized bisoindigo units (y), and unreacted terthiophene units (z).

Experimental data suggests that the formation of thiophene dioxides (in segment x) is quite low while formation of the epoxide functionalized bisoindigo (in segment y) is relatively high. As the disruption of conjugation along the polymer would likely have significant detrimental effects on the performance of this material in organic electronic devices, the post-polymerization functionalization approach was not pursued any further.

3.3 Conclusions

In this chapter a variety of synthetic routes towards thiophene dioxide containing polymers were explored. The strongly electron-deficient thiophene dioxides are a promising structure for electron conducting conjugated polymers due to their low LUMO energy level and stable quinoidal structure. The synthesis of a thiophene dioxide containing terthiophene unit was completed; however, it could not be functionalized appropriately to allow for polymerization with bisoindigo, presumably due to the poor selectivity of the strong bases used. An alkylated variant of this structure was instead targeted to prevent the issue of regioselectivity; however, this terthiophene could not be incorporated into polymers. Synthesis of the alkylated terthiophene dioxide showed that end-capping of terthiophene units during *m*-CPBA oxidation to prevent dimerization was unnecessary, in contrast to the literature. As traditional monomer-based synthesis of thiophene dioxide polymers was unsuccessful, a post-polymerization modification method was applied to a bisoindigo-terthiophene polymer by reaction with *m*-CPBA, a relatively mild and safe oxidizing agent. UV/Vis and infrared spectroscopy suggested this resulted in epoxide formation within the bisoindigo structure, disrupting conjugation within the polymer. X-ray photoelectron spectroscopy indicated that thiophene dioxides were formed in small amounts. While epoxidation

was the main reaction occurring, this shows that *m*-CPBA can be used to functionalize polymers to some extent post-polymerization. The use of this strategy on conjugated polymers without reactive alkenes may allow for more successful post-polymerization modification using *m*-CPBA in the future.

Chapter 4 – Conclusions and Outlook

4.1 Summary and Conclusions

The primary goal of this thesis was to explore the effect of increasing the proportion of electron acceptor units within bisisoindigo copolymers, as this has been previously shown to lower frontier molecular orbital energies and improve electron mobilities in OFETs.⁸⁰ This structural modification was achieved by synthesizing bisisoindigo and benzothiadiazole containing conjugated polymers. The benzothiadiazole units were more electron withdrawing than previously used thiophene and alkene donors, and fluorination of the benzothiadiazole was used to further increase the electron withdrawing character. These polymers performed well as ambipolar semiconductors in bottom-gate bottom-contact OFETs with Au electrodes. The OFET threshold voltages were significantly improved by changing the source and drain electrodes to LiF/Al contacts which allowed for improved energy alignment of the polymer LUMO with the electrode Fermi energy. Disordered packing of polymer thin films and a nonlinear polymer backbone were identified as potential limiting factors towards high charge carrier mobilities. Additionally, the electron rich thiophene units were assumed to give sufficient donor character to the polymers to prevent unipolar electron transport as observed in all-acceptor polymers.

Thiophene dioxides were also explored as an alternative to benzothiadiazole acceptor units. Several synthetic routes were used to make thiophene dioxides and terthiophene dioxides; however, these materials could not be properly functionalized to be used in traditional cross-coupling reactions. As an alternative, post-polymerization functionalization was used to produce similar polymers containing thiophene dioxides using *m*-CPBA, a relatively safe oxidant that can be used under mild reaction conditions. Characterization of the *m*-CPBA modified polymer was performed using UV/Vis and IR absorption spectroscopy along with XPS. The post-polymerization modification worked to some degree, leading to a small amount of produced thiophene dioxide and a large disruption of the conjugation along the polymer backbone, likely the result of epoxidation.

4.2 Discussion and Limitations

The work in Chapter 2 on bisisoindigo and benzothiadiazole containing polymers produced materials with increased acceptor proportion relative to previous bisisoindigo polymers but did not produce unipolar n-channel OFETS like other acceptor-acceptor polymers. This suggests that

neither the bisoindigo unit or the dithienyl benzothiadiazole unit are as strong acceptors as other common acceptor units like diketopyrrolopyrrole or naphthalene diimide. Despite having lower frontier molecular orbital energies than previous bisoindigo polymers, there was no significant change in the charge carrier mobilities of these new materials. This indicates that the molecular geometry and film morphology of these polymers is likely more important than frontier molecular orbital energies in determining charge carrier mobilities in these materials. The selection of less sterically demanding alkyl chains and more planar conjugated units that also allow for more linear polymer geometries could allow for improved charge carrier mobilities in future materials. Previous work by Lei et al.^{59–61} on isoindigo donor-acceptor polymers suggested the importance of centrosymmetric units which allowed for more linear polymer chains and higher crystallinity in polymer thin films. The dithienyl-benzothiadiazole units used in Chapter 2 were predicted in DFT calculations to be axisymmetric rather than centrosymmetric, leading to non-linear polymer chains. This likely contributed to the disordered packing observed by GIWAXS and lowered the observed charge carrier mobilities in OFETs. The observation of a significantly reduced threshold voltage with a selection of LiF/Al electrodes highlights the importance of the contact metals, particularly for ambipolar and n-channel OFETs. These electrodes however also resulted in decreased currents and Al electrodes tend to be relatively unstable, so better electrode materials are still desirable.

The post-polymerization functionalization of conjugated polymers in Chapter 3 led to significant problems of low conversion and selectivity for the desired thiophene dioxides. This is somewhat unsurprising given that similar reactions required the use of very reactive oxidizing agents. This could suggest that the installation of thiophene dioxides is not the best target for post-polymerization functionalization of conjugated polymers, or that the polymer starting materials need to be particularly well suited to this type of reaction.

4.3 Future Work

Based on the above discussion of limitations of the present work, there are many potential directions for future study. Modification of the bisoindigo structure towards a more planar geometry could result in better packing in thin films and improved charge transport. It has been shown that replacement of the benzene rings in isoindigo with thiophenes to create thienoisindigo led to a more planar structure by the removal of the steric interactions of the carbonyl oxygen with the nearby hydrogen atoms.^{130,131} Applying this same strategy to bisoindigo could produce a more

planar structure that would allow for better π stacking in thin films. Including the more electron rich thiophene units may however reduce the acceptor strength of this bisoindigo analogue. The use of less sterically demanding alkyl chains like those used in work by Lei et al.^{69–71} could also allow increased π stacking in thin films and allow for better charge transport. The proposed thienobisindigo structure for use in making conjugated polymers is shown below in Figure 4.1. The dibrominated thienobisindigo could be used in traditional metal catalyzed cross coupling reactions to produce conjugated polymers.

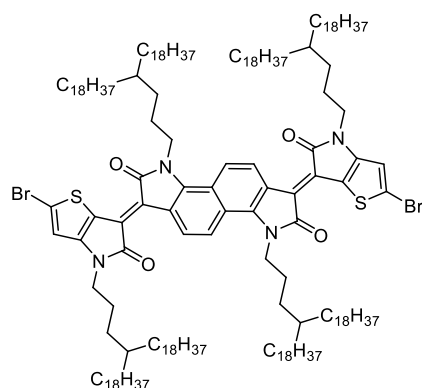


Figure 4.1 Thienobisindigo, a proposed structural analogue of bisoindigo predicted to give a more planar structure.

In selecting a comonomer coupling partner for thienobisindigo there are several directions to improve on the benzothiadiazole based acceptor units used in Chapter 2. One limitation that was identified was that the thiophene units in the dithienyl-benzothiadiazoles were likely too electron rich to be used in unipolar electron conducting acceptor-acceptor polymers. It has been shown that thiazoles can be used in place of thiophenes to make all-acceptor conjugated polymers.^{132,133} Combining thiazoles with benzothiadiazoles could replace the dithienyl-benzothiadiazoles used in Chapter 2 and allow a direct comparison between the thiazoles and thiophenes when incorporated into conjugated polymers as shown in Figure 4.2.

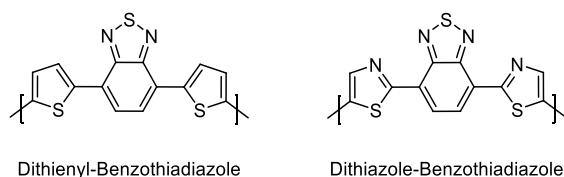


Figure 4.2 Comparison of dithienyl-benzothiadiazole used in Chapter 2 with proposed dithiazole-benzothiadiazole which could be paired with bisoindigo or thienobisindigo to make acceptor-acceptor polymers.

These new acceptors are still predicted to give axisymmetric rather than centrosymmetric structures, which has been associated with non-linear polymer backbones, poorer film morphologies, and lower charge carrier mobilities. Adding an additional benzothiadiazole unit can be used to create centrosymmetric acceptors and potentially increase ordering in thin films and charge carrier mobilities. Proposed structures based on previously synthesized benzothiadiazoles are shown below in Figure 4.3.^{134,135}

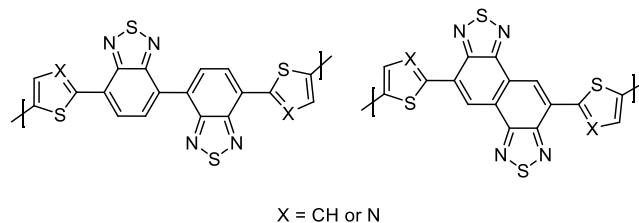
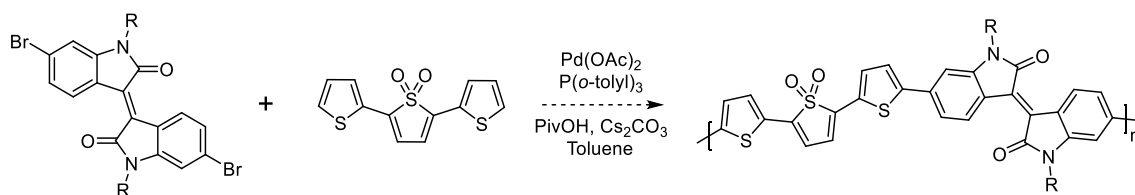


Figure 4.3 Structures for centrosymmetric benzothiadiazole acceptor units flanked by thiophene or thiazole units.

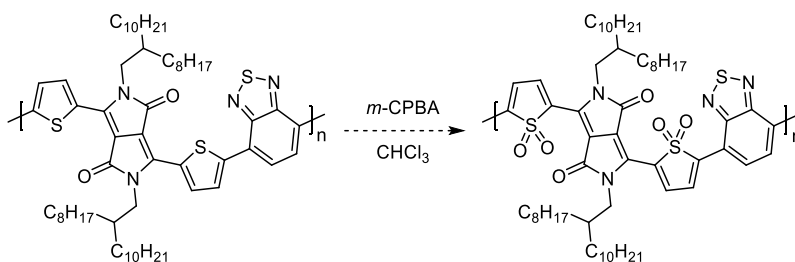
Combining some or all of these structural modifications would allow for a series of structural analogues of the polymers synthesized in Chapter 2 to be made. Comparison of the optoelectronic properties of these materials as well as their thin film morphology and OFET performance would allow for evaluation of the different structural modifications and identify which factors are most important in developing high performance OFET materials.

In Chapter 3 the thiophene dioxide containing units were unable to be functionalized for use in Stille or Suzuki cross-coupling reactions to yield conjugated polymers. As an alternative method, direct-heteroarylation polymerization (DHAP) could be used to produce conjugated polymers. Brominated isoindigo units have been successfully coupled with various thiophenes using DHAP and could be used to make new acceptor-acceptor materials.^{64,136,137} A proposed route is shown below in Scheme 4.1. This polymer could then be compared against poly(isoindigo-terthiophene) and poly(isoindigo-dithienyl-benzothiadiazole) polymers to determine the acceptor strength of the terthiophene dioxide unit relative to these more well studied systems.



Scheme 4.1 DHAP synthesis of isoindigo-terthiophene dioxide copolymer. Synthetic conditions are general, as taken from DHAP reviews by Leclerc and coworkers.^{19–22}

The post-polymerization functionalization of a bisoindigo-terthiophene copolymer with *m*-CPBA was shown to produce terthiophene dioxides and epoxides. To adopt this functionalization more successfully it could be applied to polymers that do not have alkenes susceptible to epoxidation as in bisoindigo. One candidate for this would be diketopyrrolopyrrole (DPP) based polymer. DPP units are usually synthesized with thiophene units flanking the acceptor unit, creating a weaker overall acceptor than the DPP unit alone.⁴ Oxidation of a DPP containing polymer by *m*-CPBA could strengthen this acceptor unit to make it better suited for n-channel OFET materials. This could be studied on a previously reported high performing DPP-benzothiadiazole polymer by Sonar et al.¹³⁸ which showed hole and electron mobilities of 0.35 cm²V⁻¹s⁻¹ and 0.40 cm²V⁻¹s⁻¹ respectively. Conversion of the thiophene units to thiophene dioxides, shown in Scheme 4.2, could allow for decreased HOMO and LUMO energies potentially resulting in unipolar n-channel OFET performance.



Scheme 4.2 Preparation of an electron conducting polymer by post-polymerization functionalization of ambipolar dithienyldiketopyrrolopyrrole-benzothiadiazole copolymer using *m*-CPBA.

Chapter 5 – Experimental

5.1 Materials and Methods

Solvents used in all reactions were obtained from an MBraun solvent purification system and were dried over 3Å molecular sieves before use. Pd₂(dba)₃, Pd(PPh₃)₄ and P(*o*-tolyl)₃ were purchased from Strem Chemicals and stored in an inert atmosphere nitrogen glovebox when not in use. Dibromobisisoindigo was prepared as previously reported.⁸⁰ 2,1,3-Benzothiadiazole-4,7-bis(boronic acid pinacol ester) was purchased from Millipore Sigma dried via high vacuum before use. Solutions of *n*-BuLi were titrated in THF against 2,6-di-*tert*-butyl-4-methyl-phenol (BHT) with fluorene as an indicator. All other reagents were purchased from either Millipore-Sigma, Fisher Scientific, or Matrix Scientific and used as received.

NMR spectra were obtained using a Bruker Avance 500 MHz spectrometer. UV/Vis measurements reported in Chapter 2 were performed using a Cary 6000i UV/vis spectrophotometer in dual beam mode with baseline and zero corrections, or for experiments in Chapter 3 using a Varian Cary 50 with baseline and zero corrections. Solution UV/Vis spectra were collected with polymers dissolved in chloroform. Thin films for UV/Vis were prepared on cut glass slides that were sonicated for 15 minutes each in 2% Extran in water, deionized water, acetone and isopropanol, dried by heating at 200 °C for 15 minutes, ozone cleaned, and then polymer films were spin cast from ~10 mg/mL solutions at 1000 rpm. Voltammetry was carried out in 0.05 mol·L⁻¹ tetrabutylammonium hexafluorophosphate dissolved in dry, degassed acetonitrile. The working electrode was glassy carbon, the counter electrode was a Pt wire, and the reference electrode was a Ag wire. Polymer films were drop cast from chloroform solution onto the working electrode and allowed to dry in air before use. Differential pulse voltammetry was performed using 15 mV steps with a 0.5 s interval time, swept from negative to positive potentials. Voltammograms were referenced to a Fc/Fc⁺ standard, estimated to be 5.1 V vs. vacuum. Cyclic voltammetry was collected at a scan rate of 100 mV/s. Mass spectra were acquired on a JEOL AccuToF 4G GCv mass spectrometer with an EiFi field desorption ionization source.

5.2 Gel Permeation Chromatography

GPC experiments were performed by Poly-Analytik using a Tosoh HLC8321 GPC/HT system with a refractive index detector. The columns were 2 x TSKgel GMHHR (S) HT2, particle size of 13 μm , with a column size of 7.8 mm ID \times 30 cm. Calibration of the GPC was performed using a either a polyethylene or polystyrene calibration kit. The polymer samples were prepared in 1,2,4-trichlorobenzene at concentrations of ~ 3.0 mg/mL. Samples were heated for minimum 1 h at 140 $^{\circ}\text{C}$ and injected into the GPC instrument.

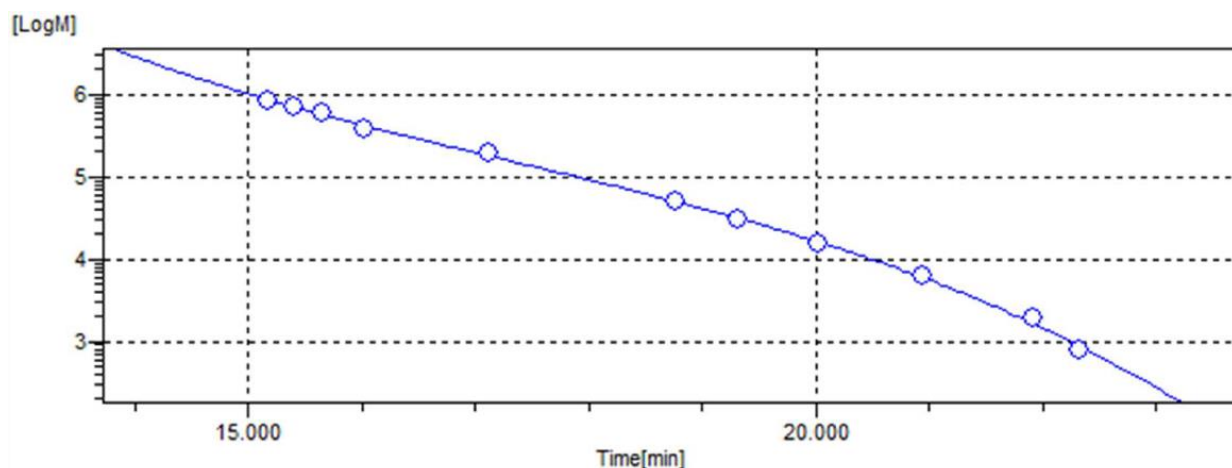


Figure 5.1 GPC calibration curve based on polyethylene standards.

Table 5.1 Calibration data from the RI detector for polyethylene conventional calibration kit. The correlation coefficient for this curve was 0.994.

Elution Time (min)	Molecular Mass (Da)	Error (%)
15.168	843,039	-2.61
15.405	718,026	2.51
15.640	593,501	3.69
16.027	381,763	-8.70
17.115	196,119	8.85
18.760	49,236	-2.10
19.313	30,221	-3.93
20.027	15,351	-4.73
20.938	6,111	2.53
21.922	1,880	13.83
22.330	773	-12.23

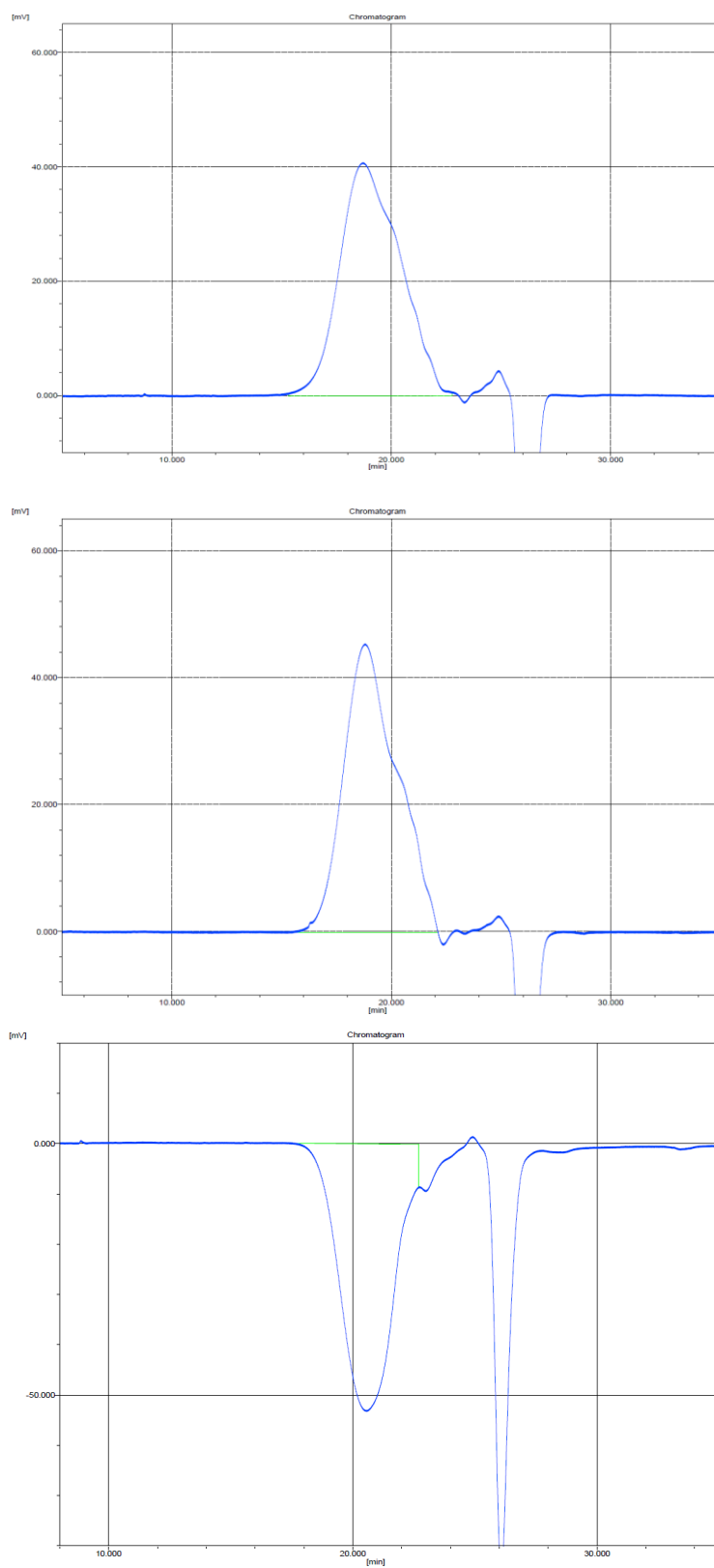


Figure 5.2 GPC traces for P1(H) (top), P2(F) (middle), and P3(B) (bottom) collected using polyethylene standards.

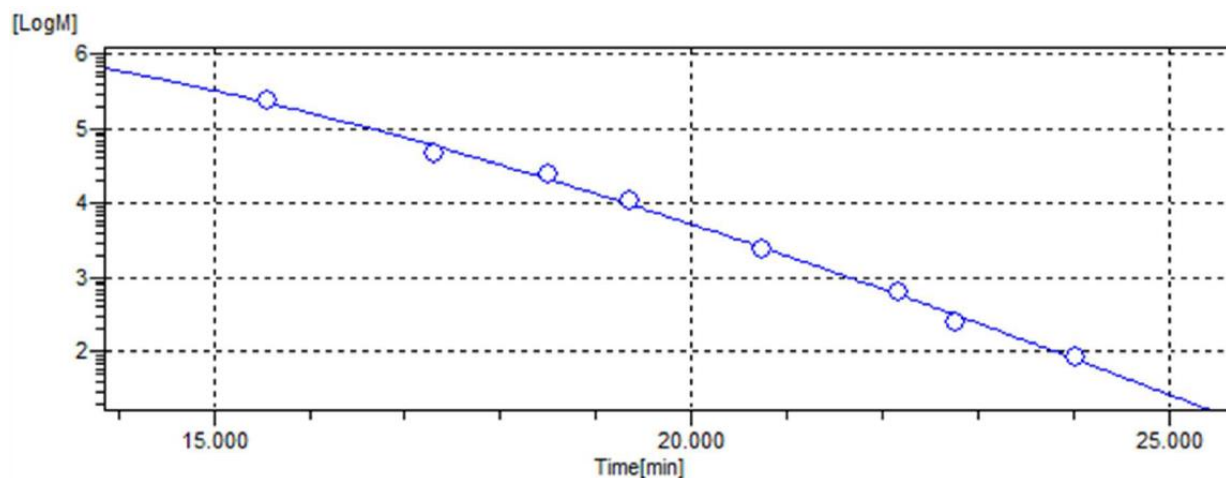


Figure 5.3 GPC calibration curve based on polystyrene standards.

Table 5.2 Calibration data from the RI detector for polystyrene conventional calibration kit. The correlation coefficient for this curve was 0.997.

Elution Time (min)	Molecular Mass (Da)	Error (%)
15.567	238,986	6.67
17.308	46,082	-28.34
18.513	24,260	13.23
19.358	10,829	10.19
20.743	2,468	-2.79
22.170	635	7.81
22.767	254	-22.25
24.020	86	7.52

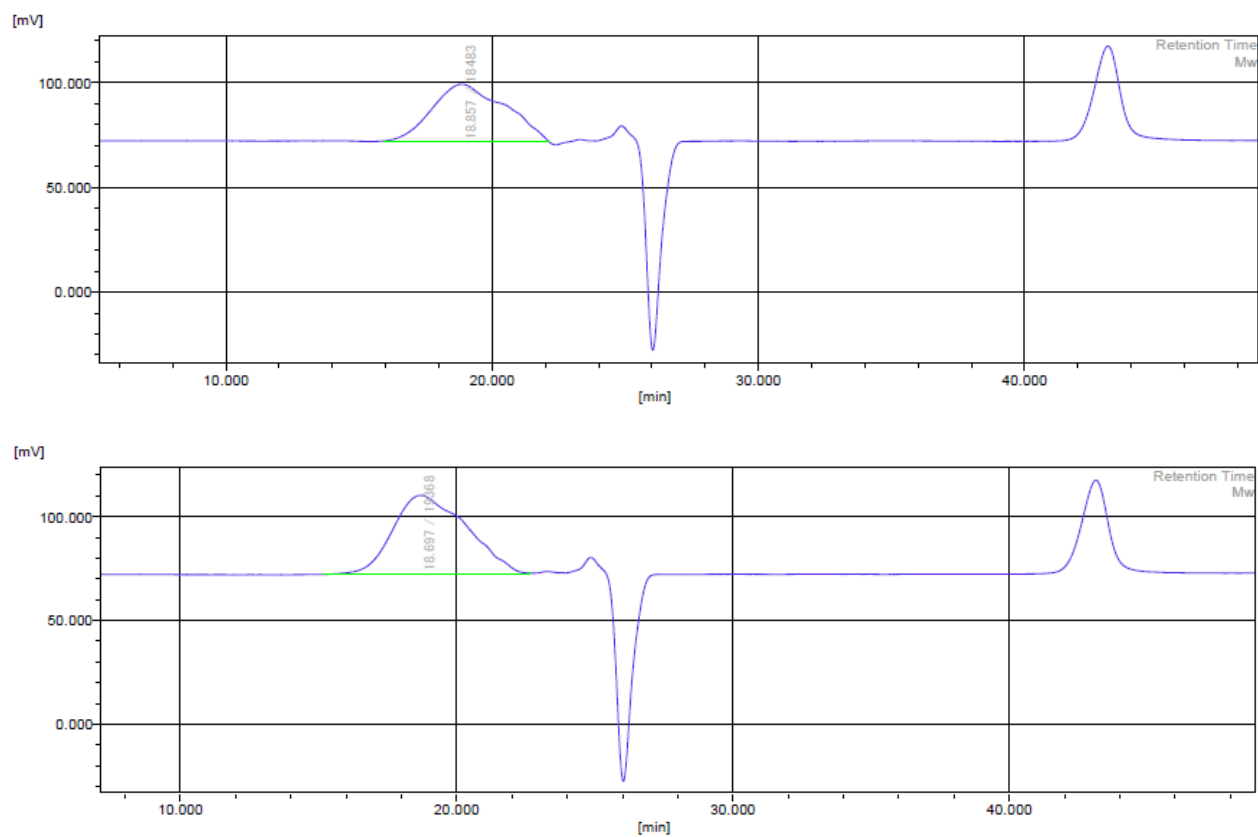


Figure 5.4 GPC traces for P1(H) (top) and P2(F) (bottom) collected using polystyrene standards.

5.3 Thermal Analysis

Thermal gravimetric analysis was run using a TA Instruments TGA Q5000IR. For each measurement ~5 mg of polymer was heated under a nitrogen atmosphere at a rate of 10 °C/min. from room temperature to 500 °C. Differential scanning calorimetry (DSC) was carried out on a TA Q20 DSC with ~2 mg of polymer which was heated from room temperature to 250 °C or 300 °C depending on the polymer decomposition temperature, then cooled to 50 °C and reheated to 250 °C or 300 °C. DSC scans were performed at a rate of 20 °C/min.

5.4 Computational Details

Density functional theory (DFT) calculations were performed using the Gaussian16 and Gaussview suites of software.¹³⁹ All calculations were performed at the ω B97XD/6-31+G(d,p) level of theory, unless otherwise noted. Geometry optimizations were performed on all structures, then frequency analyses were performed to ensure that the optimizations had successfully converged to a potential energy minimum. Single point energy and time-dependent calculations were performed using a solvent continuum model with a dielectric constant equal to that of chloroform. Time dependent DFT (TD-DFT) calculations were used to determine the vertical excited state transitions and their corresponding oscillator strengths.

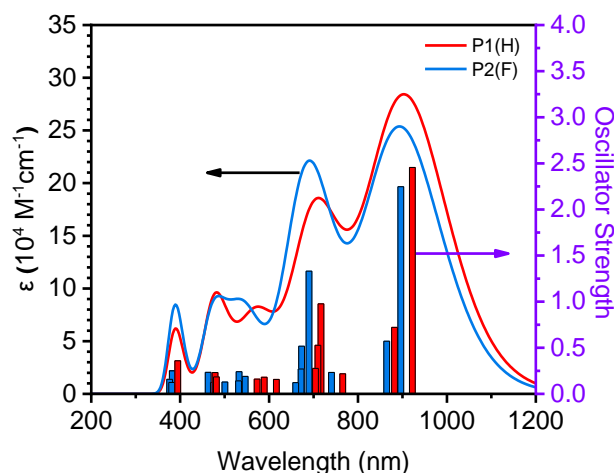


Figure 5.5 TD-DFT calculated UV-Vis spectra for 2.5 repeat unit oligomers (ex. dTBT-BII-dTBT-BII-dTBT) using B3LYP/6-31G(d,p). The lower level of theory relative to ω B97XD allowed for modelling of longer oligomers and resulted in smaller calculated bandgaps more similar to experimental data, but gives poorer reproduction of experimental UV/Vis spectra.

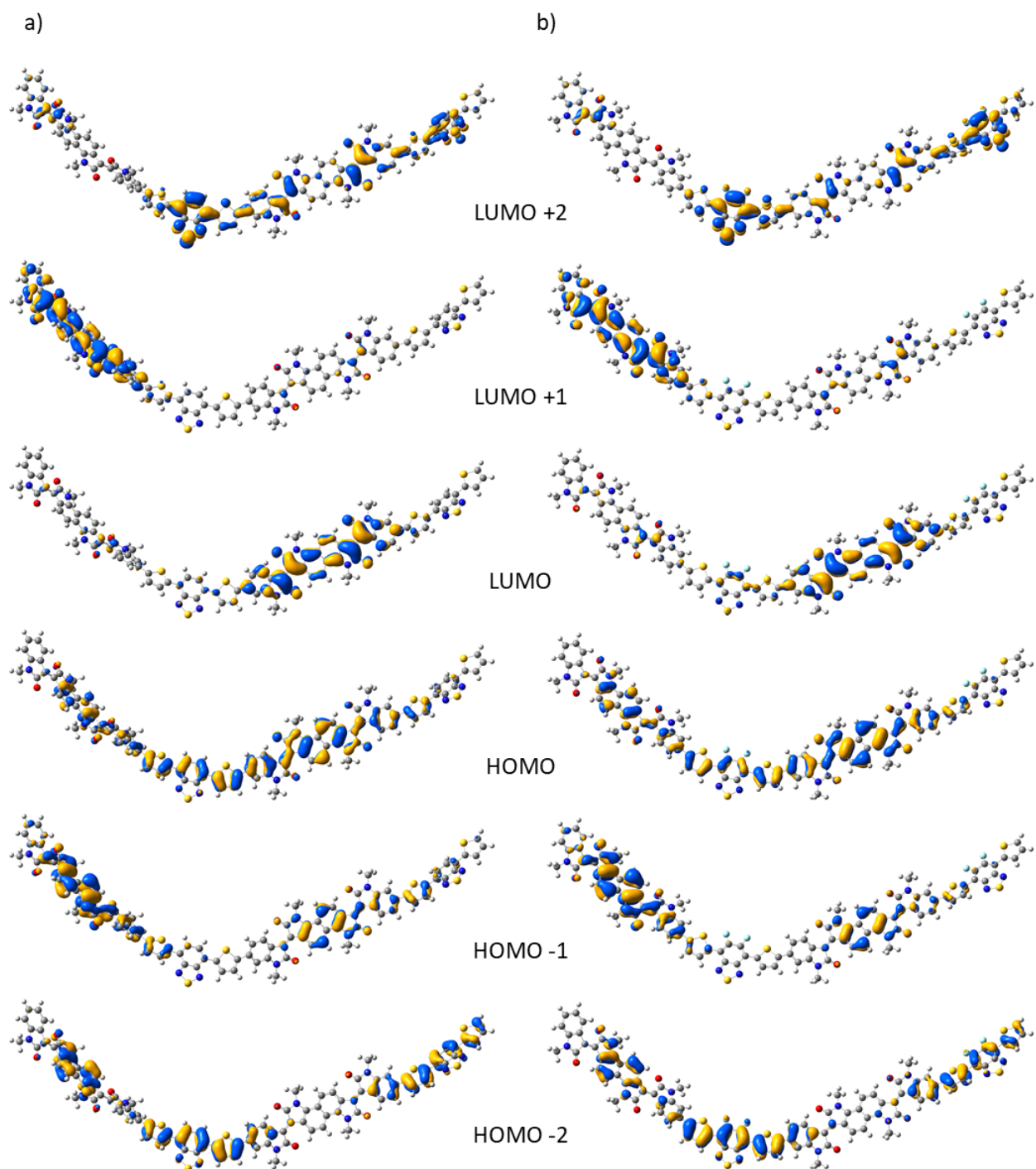


Figure 5.6 Orbital isosurfaces for two-repeat-unit oligomers of a) P1(H) (BII-dTBT-BII-dTBT) and b) P2(F) (BII-FdTBT-BII-FdTBT). Isosurfaces generated using ω B97XD/6-31+G(d,p) using a dielectric constant equal to that of chloroform.

5.5 OFET Manufacturing and Testing

Bottom-gate bottom-contact OFETs were manufactured using a p-doped silicon wafer as the gate electrode and a thermally grown SiO₂ dielectric layer (300nm). Au source and drain electrodes were patterned onto the SiO₂ layer using conventional photolithography. Polymers were spin-coated from chloroform solution (5 mg/mL) at 2000 rpm. The channel lengths and widths were 30 and 1000 μm respectively. Thermal annealing was sequentially performed in 20-minute intervals at the indicated temperatures in an inert atmosphere glovebox.

Bottom-gate top-contact OFET devices were manufactured using a n-doped silicon wafer as the gate electrode and a thermally grown SiO₂ dielectric layer (300 nm). The surface of the Si/SiO₂ substrate was modified by dodecyltrichlorosilane solution (10 mM in toluene) by submerging the substrate in the solution for 20 minutes. Polymers were spin-coated from chloroform solution (5 mg/mL) at 2000 rpm. Thermal annealing was performed for 20 minutes at 100 °C. Source and drain contacts were added by thermally evaporating LiF (1 nm) and Al (100 nm). The channel lengths and widths were 100 and 3000 μm respectively.

Charge carrier mobilities were extracted from the saturation regime using the slope of the $(I_D)^{1/2}$ plotted against the gate potential using equation 1.19.

$$\mu_{\text{sat}} = \frac{2L}{CW} \left(\frac{\partial \sqrt{I_D}}{\partial V_G} \right)^2 \quad \text{Equation 1.19}$$

5.6 GIWAXS Measurements

GIWAXS experiments were performed at the Hard X-ray Microanalysis (HXMA) beamline at the Canadian Light Source (CLS). A photon energy of 12.688 keV was used as selected by a Si(111) monochromator. GIWAXS patterns were collected using a MAR165 detector. The sample to detector distance was 224 mm as determined by a silver behenate thin film reference standard. A lead beam stop was used to block the direct beam path. Polymer thin films were spin-coated at 1000 rpm from chloroform solutions (5 mg/mL) onto single crystal Si wafers cut into 1.5×1.5 cm² pieces. Thermal annealing after deposition of polymer thin films was performed for 20 minutes at 200 °C, with scattering patterns measured for samples with and without thermal annealing. All scattering patterns were collected while the samples were within a helium filled

sample chamber. Data processing was performed using both Datasqueeze and the Matlab plugin GIXSGUI.

5.7 Post-polymerization Functionalization

5.7.1 Titration of *m*-CPBA

Prior to use in post-polymerization functionalization, *m*-CPBA was titrated to determine its purity by weight percent, as it was received at a purity of $\leq 77\%$ by mass to limit its shock sensitivity. The *m*-CPBA was first reacted with NaI to produce a red I₂ solution, which was then titrated to a colorless endpoint by reaction with Na₂S₂O₃. Solutions prepared with approximately 1.5 g NaI and 0.1 g *m*-CPBA (weighed accurately), 50 mL distilled water, 5 mL glacial acetic acid and 5 mL chloroform. A 0.100 M solution of Na₂S₂O₃ was prepared in distilled water, then was slowly added to the above solution by burette with vigorous mixing until a completely clear colorless solution was achieved. This procedure was repeated in triplicate and the *m*-CPBA was determined to be $74 \pm 1\%$ pure by mass.

5.7.2 Functionalization of BII-3T with *m*-CPBA

Two dry argon filled Schlenk flasks were prepared. To one was added BII-3T (0.0293, 0.0162 mmol of repeat unit) and 10 mL dry chloroform. To the other was added *m*-CPBA (74% pure by mass, 0.2266 g, 0.9717 mmol) and 6 mL dry chloroform. Each solution was stirred to dissolve the solids. The UV/Vis spectrum before start of reaction was measured using 0.1 mL of BII-3T solution and dissolving it with 10 mL (10.1 mL total volume). After this, 0.1 mL of *m*-CPBA solution (1 eq) was transferred to the polymer solution, allowed to stir for 15 minutes. Then 0.1 mL of reaction mixture removed, diluted with 10 mL of chloroform and measured using UV/Vis. This process was repeated every 15 minutes until 6 equivalents of *m*-CPBA was added and changes in the UV/Vis spectra began to be observed. The mixture was then left to continue stirring and UV/Vis measurements were performed at 4, 18, 20, 22, and 24 hours from initial addition of oxidant. No more changes were observed after 22h, so the solution was poured over water, washed three times with NaHCO₃, then washed with brine and dried over Na₂SO₄ and concentrated, yielding 0.0321 g as a green/black solid. IR measurements performed on solid polymer samples from before and after the reaction using a Bruker Alpha II Compact FTIR Spectrometer in reflection mode.

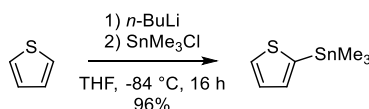
5.8 X-ray Photoelectron Spectroscopy

All X-ray Photoelectron Spectroscopy (XPS) measurements were collected using a Kratos (Manchester, UK) AXIS Supra system at the Saskatchewan Structural Sciences Centre (SSSC). This system is equipped with a 500 mm Rowland circle monochromated Al K- α (1486.6 eV) source and combined hemi-spherical analyzer (HSA) and spherical mirror analyzer (SMA). A spot size of hybrid slot (300x700) microns was used. All survey scan spectra were collected in the -5-1200 eV binding energy range in 1 eV steps with a pass energy of 160 eV. High resolution scans of 2 regions were also conducted using 0.05 eV steps with a pass energy of 20 eV. An accelerating voltage of 15 keV and an emission current of 15 mA was used for the analysis.

Polymer samples were measured as solids adhered on carbon tape. Binding energies were calibrated to the adventitious carbon peaks at 284.8 eV. Peak fitting of the S 2p peaks was performed using a combination of Gaussian and Lorentzian peak shapes using the CasaXPS software package with a Tougaard type background.

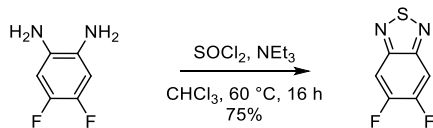
5.9 Detailed Synthetic Procedures

5.9.1 Synthesis of 2-trimethylstannyl thiophene (1)



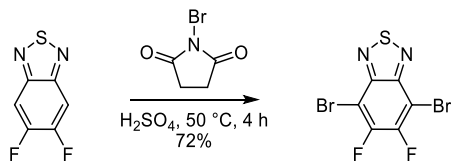
To a dry argon filled flask was added 1.50 mL thiophene (18.8 mmol) and 35 mL dry THF before cooling to -84 °C. While stirring, *n*-BuLi was added dropwise (7.50 mL, 2.5 M solution in hexanes, 18.8 mmol) and reaction left to stir at -84 °C for one hour, giving color change to red solution. To this was added SnMe₃Cl (20.0 mL, 1.0 M in hexanes, 20 mmol) at -84 °C, then reaction allowed to warm to room temperature and stirred overnight. Reaction was quenched with 50 ml saturated NH₄Cl_(aq) solution, extracted with ethyl acetate. Organic layer was washed with water, dried over MgSO₄ and concentrated, giving the product as an orange liquid (4.450 g, 96.0%). ¹H NMR (500 MHz, CDCl₃) δ : 7.83 (m, 1H), 7.46 (m, 2H), 0.61 (s, 9H).

5.9.2 Synthesis of 5,6-difluoro-2,1,3-benzothiadiazole (2)



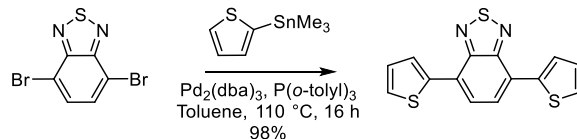
To a dry argon filled flask was added 4.017 g 1,2-diamino-4,5-difluorobenzene (27.9 mmol), 16.0 mL NEt_3 (114.8 mmol), and 80 mL of dry CHCl_3 before being set to stir at $0\text{ }^\circ\text{C}$. To a second flask was added 20 mL dry CHCl_3 and 4.8 mL SOCl_2 (65.8 mmol), then cooled in ice bath to $0\text{ }^\circ\text{C}$. Upon cooling, the SOCl_2 solution was slowly transferred into the flask with the diamine solution at $0\text{ }^\circ\text{C}$. After complete addition the ice bath was removed and the reaction was refluxed overnight. Reaction mixture was brought to room temperature, poured over water (Caution, produces HCl and SO_2) and extracted with CH_2Cl_2 , organic layer was washed with water, dried over Na_2SO_4 , then concentrated. Product redissolved in CH_2Cl_2 , passed through silica plug and concentrated to give a brown crystalline solid. (3.585 g, 75% yield). ^1H NMR (500 MHz, CDCl_3) δ : 7.74 (t, $^3J = 8.7\text{ Hz}$, 2H). ^{19}F NMR (470 MHz, CDCl_3) δ : -128.93 (t, $^3J = 8.7\text{ Hz}$).

5.9.3 Synthesis of 4,7-dibromo-5,6-difluoro-2,1,3-benzothiadiazole (3)



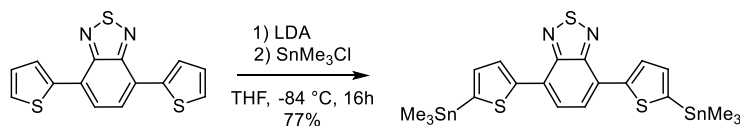
To a dry argon filled flask was added 1.019 g 5,6-difluoro-2,1,3-benzothiadiazole (5.92 mmol) and 50 mL conc. H_2SO_4 . Mixture stirred to dissolve, covered with foil, then added 4.674 g *N*-bromosuccinimide (26.26 mmol) and heated to $50\text{ }^\circ\text{C}$ for 4 hours. Mixture cooled to room temperature, poured over ice (Caution, exothermic) and filtered. Solid washed with water to give an off-white solid (1.404 g, 72% yield). No peaks observed in the ^1H NMR. ^{19}F NMR (470 MHz, CDCl_3) δ : -119.54 (s).

5.9.4 Synthesis of 4,7-dithieno-2,1,3-benzothiadiazole (4)



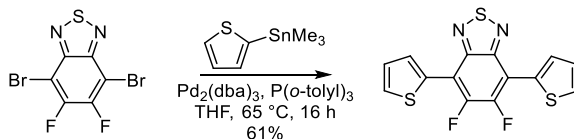
To a dry argon filled flask was added 4,7-dibromo-2,1,3-benzothiadiazole (1.165 g, 3.96 mmol), tris(dibenzylideneacetone)dipalladium (0.185 g, 0.020 mmol), tri(*o*-tolyl) phosphine (0.203 g, 0.67 mmol) and 2-trimethylstannylthiophene (2.502 g, 10.13 mmol) were dissolved in 75 mL dry toluene. Reaction mixture brought to reflux and stirred overnight. Reaction mixture cooled to room temperature, poured over sat. $\text{NH}_4\text{Cl}_{(\text{aq})}$ and extracted with ethyl acetate. The organic layer was washed with water, dried over Na_2SO_4 , filtered through a silica plug, concentrated, then recrystallized from methanol giving a dark red solid (1.169 g, 98% yield). ^1H NMR (500 MHz, CDCl_3) δ : 8.12 (dd, $^3J = 3.7$ Hz, $^4J = 1.1$ Hz, 2H), 7.88 (s, 2H), 7.46 (dd, $^3J = 5.1$ Hz, $^4J = 1.0$ Hz, 2H), 7.22 (dd, $^3J = 5.1$ Hz, $^3J = 3.7$ Hz, 2H).

5.9.5 Synthesis of 4,7-bis(5-(trimethylstannyl)thiophen-2-yl)-2,1,3-benzothiadiazole (5)



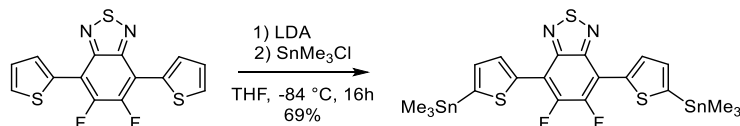
To a dry argon filled flask was added 0.235 g 4,7-dithieno-2,1,3-benzothiadiazole (0.78 mmol) and 10 mL dry THF. To a second dry argon filled Schlenk flask was added 0.78 mL diisopropylamine (5.57 mmol), and 5 mL dry THF. Each flask was degassed with bubbling argon for 30 minutes. Diisopropylamine solution was cooled to 0 °C before dropwise addition of *n*-BuLi (0.78 mL, 2.5 M solution in hexanes, 1.95 mmol). This solution was stirred for 45 minutes to generate lithium diisopropyl amide. The other solution was cooled in -84 °C bath before dropwise addition of the LDA solution and stirred for 2 hours, giving color changes from orange to dark red, to green, to blue, and finally to dark purple. At -84 °C SnMe_3Cl solution was added (1.50 mL, 1.0 M solution in hexanes, 1.50 mmol) turning solution to a dark brown color. Reaction then allowed to warm to room temperature and stirred overnight. Reaction mixture was poured over water, extracted with CH_2Cl_2 , dried over Na_2SO_4 , concentrated, then crude solid was recrystallized by with layered CH_2Cl_2 and methanol to give black needle crystals (0.373 g, 77% yield). ^1H NMR (500 MHz, CDCl_3) δ : 8.18 (d, $^3J = 3.5$ Hz, 2H), 7.88 (s, 2H), 7.30 (d, $^3J = 3.5$ Hz), 0.43 (s, 18H).

5.9.6 Synthesis of 5,6-difluoro-4,7-dithieno-2,1,3-benzothiadiazole (6)



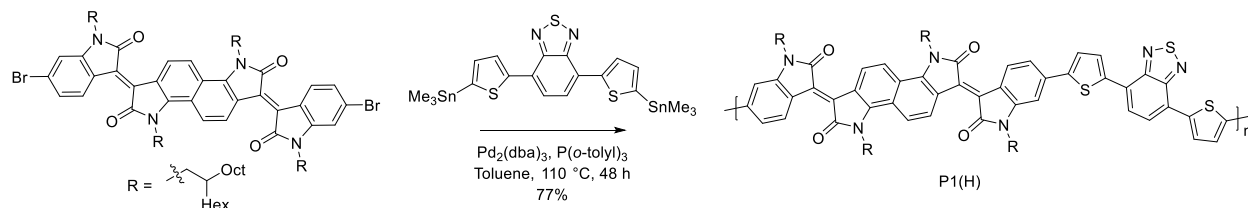
To a dry argon filled flask was added 4,7-dibromo-5,6-difluoro-2,1,3-benzothiadiazole (1.157 g, 3.51 mmol), tris(dibenzylideneacetone)dipalladium (0.177 g, 0.019 mmol), tri(*o*-tolyl) phosphine (0.175 g, 0.57 mmol) and 2-trimethylstannylthiophene (2.550 g, 10.33 mmol) were dissolved in 75 mL dry toluene. Reaction mixture brought to reflux and stirred overnight. Reaction mixture cooled to room temperature, poured over water and extracted with ethyl acetate. The organic layer was washed with aqueous saturated sodium chloride, dried over Na₂SO₄ and concentrated. Column chromatography was performed using 20:80 dichloromethane: hexanes as the mobile phase. Product isolated as an orange solid (0.715 g, 61% yield). ¹H NMR (500 MHz, CDCl₃) δ: 8.30 (d, ³*J* = 3.7 Hz, 2H), 7.63 (d, ³*J* = 5.1 Hz, 2H), 7.28 (t, ³*J* = 4.5 Hz, 2H). ¹⁹F NMR (470 MHz, CDCl₃) δ: -128.99 (s).

5.9.7 Synthesis of 5,6-Difluoro-4,7-bis(5-(trimethylstannyl)thiophen-2-yl)-2,1,3-benzothiadiazole (7)



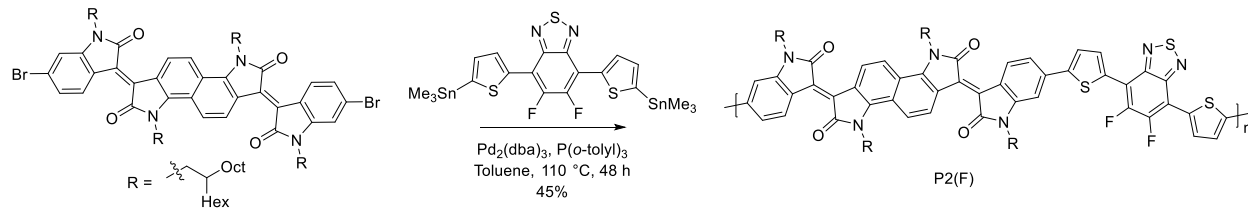
To a dry argon filled flask was added 0.285 g 5,6-difluoro-4,7-dithieno-2,1,3-benzothiadiazole (0.85 mmol) and 40 mL dry THF. To a second dry argon filled Schlenk flask was added 0.30 mL diisopropylamine (2.14 mmol), and 5 mL dry THF. Each flask was degassed with bubbling argon for 30 minutes. Diisopropylamine solution was cooled to 0 °C before dropwise addition of *n*-BuLi (0.80 mL, 2.5 M solution in hexanes, 2.00 mmol). This solution was stirred for 1 hour to generate lithium diisopropyl amide. The other solution was cooled in -84 °C bath before dropwise addition of the LDA solution and stirred for 2 hours, giving color changes from orange to dark red, to dark purple. At -84 °C SnMe₃Cl solution was added (1.69 mL, 1.0 M solution in hexanes, 1.69 mmol). Reaction then allowed to warm to room temperature and stirred overnight. Reaction mixture was poured over water, extracted with Et₂O, washed with brine, dried over Na₂SO₄, concentrated, then crude solid was recrystallized by with layered CH₂Cl₂ and methanol to give black needle crystals

5.9.8 Synthesis of Poly(bisindigo-dithienylbenzothiadiazole) P1(H)



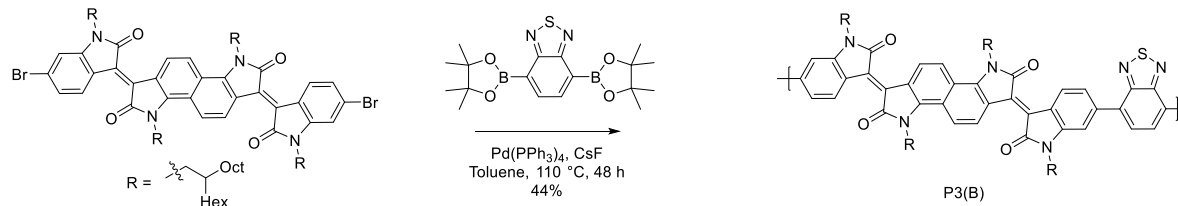
92

5.9.9 Synthesis of Poly(bisisoindigo-difluoro-dithienyl-benzothiadiazole) P2(F)



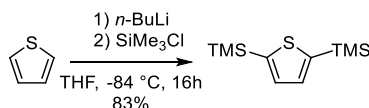
To a dry argon filled flask was added 5,6-difluoro-4,7-bis(5-(trimethylstannyl)thiophen-2-yl)-2,1,3-benzothiadiazole (0.108 g, 0.164 mmol), dibromobisisoindigo (0.253 g, 0.164 mmol) and 20 mL dry toluene. This mixture was stirred and degassed for 1 h before addition of $\text{Pd}_2(\text{dba})_3$ (0.017 g, 0.019 mmol) and $\text{P}(o\text{-tolyl})_3$ (0.017 g, 0.055 mmol). The mixture was then stirred and brought to reflux for 48 h. The reaction was then cooled to room temperature and a spatula of diethyldithiocarbamic acid diethylammonium salt was added, then stirred additional 1 h. The reaction mixture was then slowly poured over methanol to precipitate crude product. The crude solid was filtered to isolate, then purified by Soxhlet extraction using methanol (24 h), acetone (24 h), hexanes (24 h), and chloroform (48 h). The chloroform was then concentrated to a minimal volume, poured over methanol to precipitate and the polymer was filtered to isolate, then dried under high vacuum to give the product as a blue-black solid (0.126 g, 45% yield). ^1H NMR (500 MHz, CDCl_3) δ : 9.02 (br), 8.92 (br), 8.34 (br), 7.63 (br), 7.42 (br), 7.16 (br), 6.70 (br), 4.10 (br), 3.77 (br), 1.25 (br), 0.84 (br). ^{19}F NMR (470 MHz, CDCl_3) δ : -127.31 (br). Elemental anal. Calculated for $\text{C}_{116}\text{H}_{164}\text{F}_2\text{N}_6\text{O}_4\text{S}_3$: C, 75.69; H, 8.98; N, 4.57; Found: C, 74.93; H, 9.11, N, 4.97.

5.9.10 Synthesis of Poly(bisisoindigo-benzothiadiazole) P3(B)



To a dry argon filled flask was added 4,7-bis (4,4,5,5-tetramethyl-1,3,2-dioxaborolan-2-yl)-2,1,3-benzothiadiazole (0.038 g, 0.097 mmol), dibromobisisoindigo (0.150 g, 0.097 mmol), CsF (0.059 g, 0.039 mmol) and 8 mL dry toluene. Reaction mixture was then stirred and degassed for 30 minutes before addition of Pd(PPh₃)₄ (0.013 g, 0.011 mmol), then brought to reflux and stirred for 48 h. Mixture then cooled to room temperature and a spatula of diethyldithiocarbamic acid diethylammonium salt was added, then stirred additional 1 h. Reaction mixture was then slowly poured over methanol to precipitate crude product. The crude solid was filtered to isolate, then purified by Soxhlet extraction using methanol (24 h), acetone (24 h), hexanes (24 h), and chloroform (48 h). The chloroform fraction was then concentrated, and any residual solvent was removed by high vacuum, yielding desired product as a black-blue solid (0.065 g, 44% yield). ¹H NMR (500 MHz, CDCl₃) δ: 9.20 (br), 9.08 (br), 7.92 (br), 7.71 (br), 7.58 (br), 4.20 (br), 3.73 (br), 1.23 (br), 0.83 (br). No signals were observed in ¹⁹F NMR.

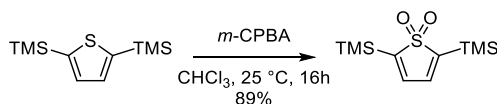
5.9.11 Synthesis of 2,5-Trimethylsilylthiophene (8)



To a dry argon filled flask was added thiophene (2.00 mL, 24.98 mmol) and 100 mL dry THF before mixture was degassed with bubbling argon for 20 minutes. The flask was then cooled in a -84 °C bath before dropwise addition of *n*-BuLi (31.00 mL, 2.31 M solution in hexanes, 71.5 mmol), giving color change from colorless to a yellow solution. Mixture was stirred for 1 hour at -84 °C before slow addition of trimethylsilyl chloride (9.5 mL, 74.9 mmol). Reaction mixture was allowed to warm to room temperature and stirred overnight. Reaction mixture washed with water, then brine, then the organic layer was dried over Na₂SO₄ and concentrated. Crude material dried on high vacuum line to remove residual solvent and any monosilylated product, and product was isolated

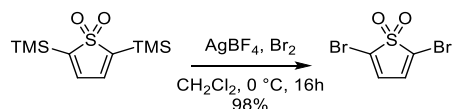
as a light yellow oil (4.740 g, 83% yield). ^1H NMR (500 MHz, CDCl_3) δ : 7.33 (s, 2H), 0.33 (s, 18H).

5.9.12 Synthesis of 2,5-Trimethylsilylthiophene-*S,S*-dioxide (9)



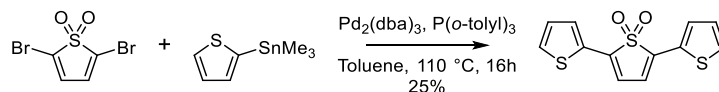
To a dry argon filled Schlenk flask was added 2,5-trimethylsilylthiophene (2.292 g, 10.03 mmol) and 40 mL dry CH_2Cl_2 . To a second dry argon filled flask was added *m*-CPBA (9.362 g, 74% pure by mass, 41.30 mmol) and 80 mL dry CH_2Cl_2 . Both were stirred to dissolve solids, then the thiophene containing flask was cooled in a 0 °C bath before slow transfer of *m*-CPBA solution into the cooled thiophene solution. Upon complete addition the mixture was allowed to warm to room temperature and stirred overnight. Reaction mixture was then filtered to remove insoluble material, then filtrate was washed three times with saturated K_2CO_3 to remove remaining 3-chlorobenzoic acid. Organic layer was then washed with water, dried over Na_2SO_4 and concentrated to give a white solid (2.332 g, 89%). ^1H NMR (500 MHz, CDCl_3) δ : 6.74 (s, 2H), 0.34 (s, 18H).

5.9.13 Synthesis of 2,5-Dibromothiophene-*S,S*-dioxide (10)



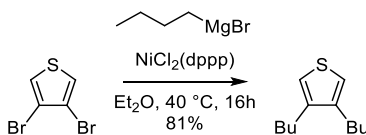
To a dry argon filled flask was added 2,5-trimethylsilylthiophene-*S,S*-dioxide (0.514 g, 1.973 mmol) and 100 mL dry CH_2Cl_2 delivered by cannula. This mixture was stirred and degassed for 40 minutes. Reaction flask was covered with aluminum foil and cooled in an ice bath before addition of AgBF_4 (1.168 g, 6.000 mmol) and liquid bromine (0.20 mL, 3.90 mmol). Reaction allowed to stir for one hour at 0 °C, then was diluted by cautious addition of 80 mL CH_2Cl_2 before filtration through silica plug. Filtrate was concentrated and product was isolated as an off-white solid (0.531 g, 98%). ^1H NMR (500 MHz, CDCl_3) δ : 6.87 (s, 2H).

5.9.14 Synthesis of 2,5-Thienylthiophene-*S,S*-dioxide (11)



To a dry argon filled flask was added 2,5-dibromothiophene-*S,S*-dioxide (0.249 g, 0.908 mmol), 2-trimethylstannylthiophene (0.623 g, 2.52 mmol) and 20 mL of dry toluene. Reaction mixture was stirred and degassed for 1 hour before addition of $\text{Pd}_2(\text{dba})_3$ (0.051 g, 0.055 mmol) and $\text{P}(o\text{-tolyl})_3$ (0.049 g, 0.162 mmol). Reaction mixture brought to reflux and stirred overnight. The reaction was cooled to room temperature then quenched by pouring over water, then extracted with CH_2Cl_2 , organic layers washed with water, dried over Na_2SO_4 and concentrated. Crude material was purified by column chromatography using 80:20 CH_2Cl_2 : hexanes as the mobile phase. Product was isolated as a red solid (0.064 g, 25%). ^1H NMR (500 MHz, CDCl_3) δ : 7.65 (dd, $^3J = 3.8$ Hz, $^4J = 0.9$ Hz, 2H), 7.45 (dd, $^3J = 5.1$ Hz, $^4J = 0.9$ Hz, 2H), 7.15 (dd, $^3J = 5.1$ Hz, $^3J = 3.8$ Hz, 2H), 6.78 (s, 2H). ^{13}C NMR (125 MHz, CDCl_3) δ : 136.2, 129.9, 128.9, 128.4, 128.1, 118.7. HRMS (m/z): (M^+) Cal. ($\text{C}_{12}\text{H}_8\text{O}_2\text{S}_3$): 279.9686 found: 279.9683.

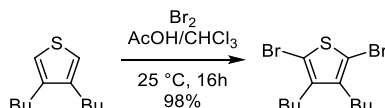
5.9.15 Synthesis of 3,4-Dibutylthiophene (12)



To a dry argon filled flask was added magnesium turnings (3.168 g, 130.3 mmol) before flame drying and refilling with argon two additional times. To this flask was added 50 mL dry Et_2O before degassing for 10 minutes with bubbling argon. To the magnesium containing flask was added a spatula tip of iodine, then stirred for 15 minutes at room temperature to give color change from brown to light cloudy grey. This mixture was then cooled to 0 °C before slow addition of 1-bromobutane (10.50 mL, 97.8 mmol), resulting in vigorous boiling as the Grignard reagent is formed. This mixture was heated to 35 °C and stirred for 1.5 hours. To a second dry argon filled flask was added $\text{NiCl}_2(\text{dppp})$ (0.526 g, 0.971 mmol), 3,4-dibromothiophene (3.60 mL, 32.6 mmol), and 50 mL dry Et_2O before degassing for 10 minutes. Both mixtures were cooled to 0 °C and the Grignard solution was slowly transferred to the other flask before reaction was stirred overnight at room temperature. The reaction was carefully quenched by slow addition of 20 mL 4 M HCl , then

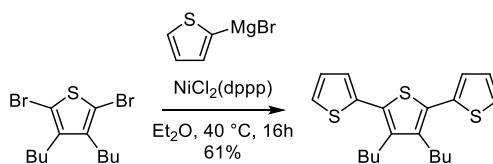
mixture was poured over water, extracted with Et₂O, organic layer washed with brine, dried over Na₂SO₄, filtered through silica and concentrated to give orange cloudy oil. This crude material was distilled under high vacuum at 150 °C to give the product as a clear colorless liquid (5.187 g, 81 %). ¹H NMR (500 MHz, CDCl₃) δ: 6.90 (s, 2H), 2.52 (m, 4H), 1.61 (m, 4H) 1.41 (m, 4H), 0.96 (t, ³J = 7.4 Hz, 6H).

5.9.16 Synthesis of 2,5-Dibromo-3,4-dibutylthiophene (13)



To a flame dried argon filled flask was added 3,4-dibutylthiophene (5.007 g, 25.50 mmol), 40 mL glacial acetic acid and 20 mL dry CHCl₃. The reaction flask was covered with aluminum foil, then the mixture was stirred and degassed with bubbling argon for 10 minutes before cooling in a 0 °C bath. To the cold flask was added liquid bromine (3.40 mL 66.4 mmol) and the reaction was allowed to warm to room temperature and stirred overnight. The reaction mixture was then poured over water, organic layer extracted with CHCl₃, washed three times with water, washed with Na₂S₂O₃ (aq), washed with brine, dried over MgSO₄ and concentrated to give the product as a yellow oil (8.904 g, 98 %). ¹H NMR (500 MHz, CDCl₃) δ: 2.51 (m, 4H), 1.42 (m, 8H), 0.94 (t, ³J = 7.2 Hz, 6H).

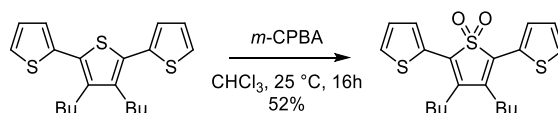
5.9.17 Synthesis of 3'4'-Dibutylterthiophene (14)



To a dry argon filled flask was added magnesium turnings (0.338 g, 13.9 mmol) before flame drying and refilling with argon two additional times. To this flask was added 10.0 mL dry Et₂O before degassing for 10 minutes with bubbling argon. To the magnesium containing flask was added a spatula tip of iodine, then stirred for 15 minutes at room temperature to give color change from brown to light cloudy grey. This mixture was then cooled to 0 °C before slow addition of 2-bromothiophene (1.518 g mL, 9.31 mmol), resulting in vigorous boiling as the Grignard reagent is formed. This mixture was heated to 35 °C and stirred for one hour. To a second dry argon filled

flask was added NiCl₂(dppp) (0.085 g, 0.056 mmol), 2,5-dibromo-3,4-dibutylthiophene (0.961 g, 2.71 mmol), and 10.0 mL dry Et₂O before degassing for 10 minutes. Both mixtures were cooled to 0 °C and the Grignard solution was slowly transferred to the other flask before reaction was stirred overnight at room temperature. Reaction was carefully quenched by slow addition of 10% HCl_(aq), then mixture was poured over water, extracted with CH₂Cl₂, organic layer washed with brine, dried over Na₂SO₄, filtered through celite and silica, then concentrated to give brown oil. This crude material was purified by column chromatography using hexanes as the mobile phase to give the product as a yellow oil. (0.599 g, 61 %). ¹H NMR (500 MHz, CDCl₃) δ: 7.30 (dd, ³J = 5.2 Hz, ⁴J = 1.1 Hz, 2H), 7.13 (dd, ³J = 3.6 Hz, ⁴J = 1.1 Hz, 2H), 7.06 (dd, ³J = 5.2 Hz, ⁴J = 3.6 Hz, 2H), 2.70 (m, 4H), 1.55 (m, 4H) 1.43 (m, 4H), 0.95 (t, ³J = 7.4 Hz, 6H).

5.9.18 Synthesis of 3'4'-Dibutylterthiophene-S',S'-dioxide (15)



To a dry argon filled Schlenk flask was added 3'4'-dibutylterthiophene (0.767 g, 2.13 mmol) and 40 mL dry CHCl₃. The mixture was stirred to dissolve and degassed for 15 minutes then covered with foil before the addition of *m*-CPBA (1.496 g, 6.42 mmol). Reaction was stirred overnight at room temperature. The mixture was then poured over water, washed with 5% NaHCO₃ and concentrated. Crude material was purified by column chromatography using a gradient mobile phase from 50:50 CH₂Cl₂: hexanes to pure CH₂Cl₂ to give product as a green solid (0.437 g, 52%). ¹H NMR (500 MHz, CDCl₃) δ: 7.74 (dd, ³J = 3.8 Hz, ⁴J = 0.9 Hz, 2H), 7.50 (dd, ³J = 5.1 Hz, ⁴J = 0.9 Hz, 2H), 7.19 (dd, ³J = 5.1 Hz, ⁴J = 3.8 Hz, 2H), 2.68 (m, 4H), 1.57 (m, 8H) 0.99 (t, ³J = 7.2 Hz, 6H). ¹³C NMR (125 MHz, CDCl₃) δ: 137.5, 130.4, 128.9, 128.6, 128.2, 128.1, 30.7, 26.9, 23.2, 13.9. HRMS (*m/z*): (M⁺) Cal. (C₂₀H₂₄O₂S₃): 392.0938 found: 392.0947.

5.10 NMR Spectra

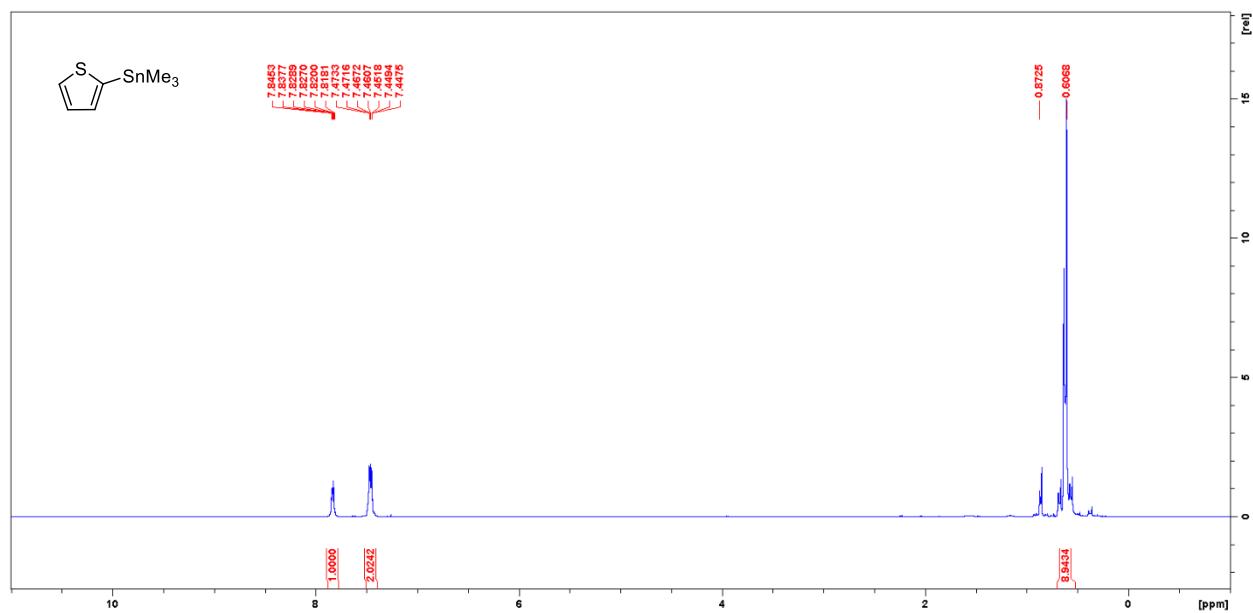


Figure 5.7 2-trimethylstannyl thiophene (1) ¹H NMR.

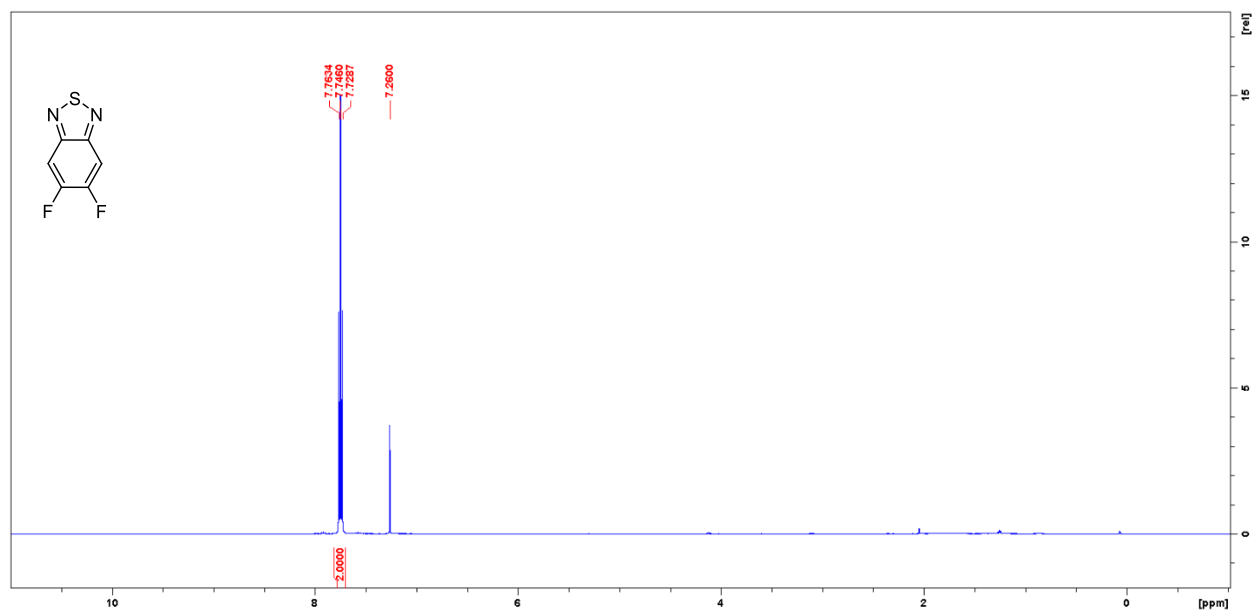


Figure 5.8 5,6-Difluoro-2,1,3-benzothiadiazole (2) ¹H NMR.

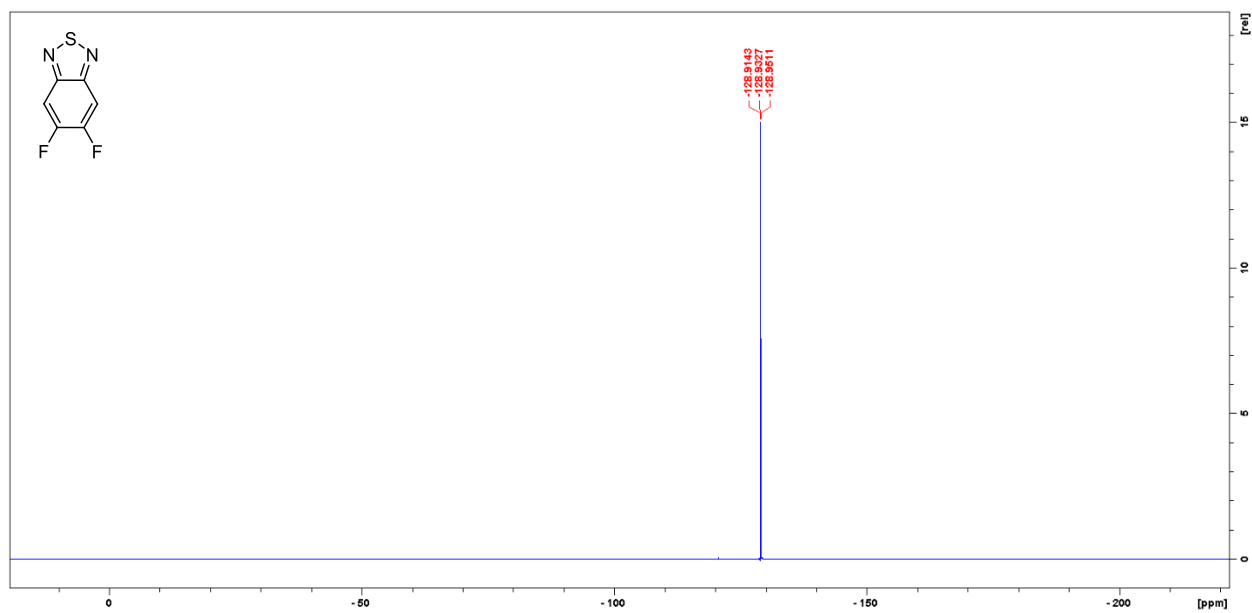


Figure 5.9 5,6-Difluoro-2,1,3-benzothiadiazole (2) ¹⁹F NMR.

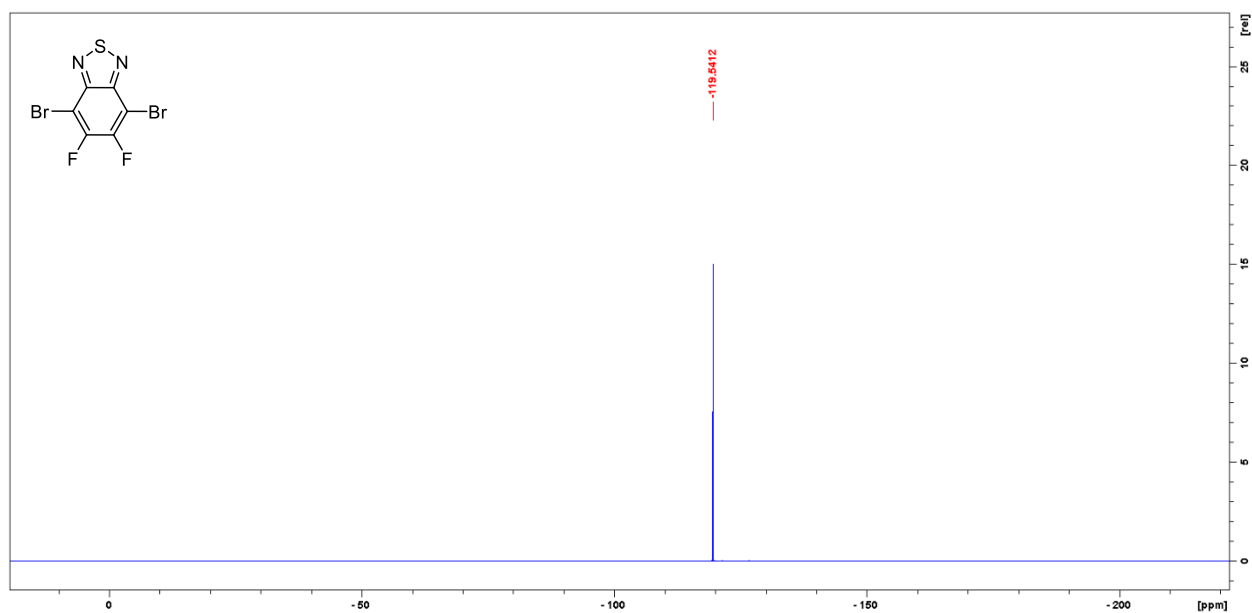


Figure 5.10 4,7-Dibromo-5,6-difluoro-2,1,3-benzothiadiazole (3) ¹⁹F NMR.

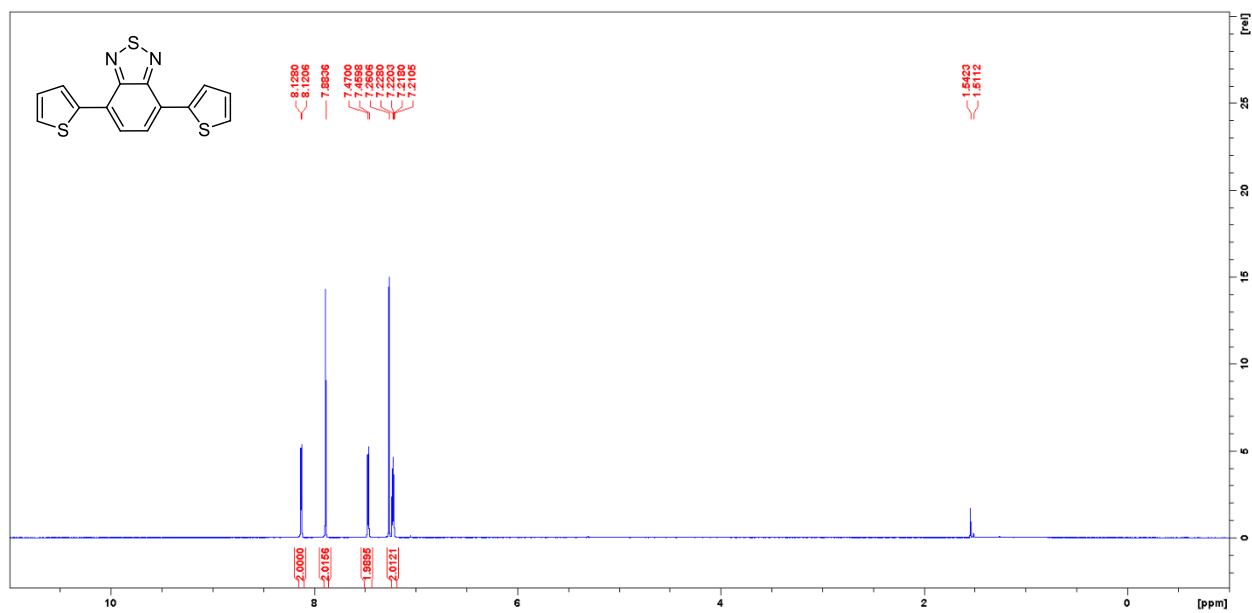


Figure 5.11 4,7-Dithieno-2,1,3-benzothiadiazole (4) ^1H NMR.

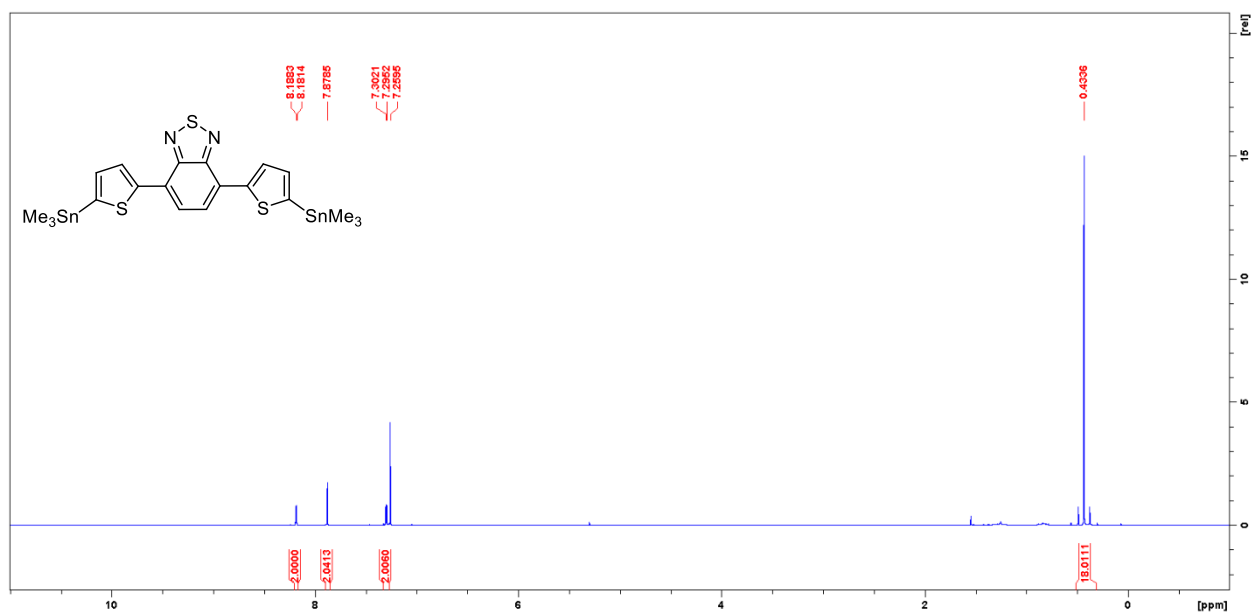


Figure 5.12 4,7-Bis(5-(trimethylstannyl)thiophene-2-yl)-2,1,3-benzothiadiazole (5) ^1H NMR.

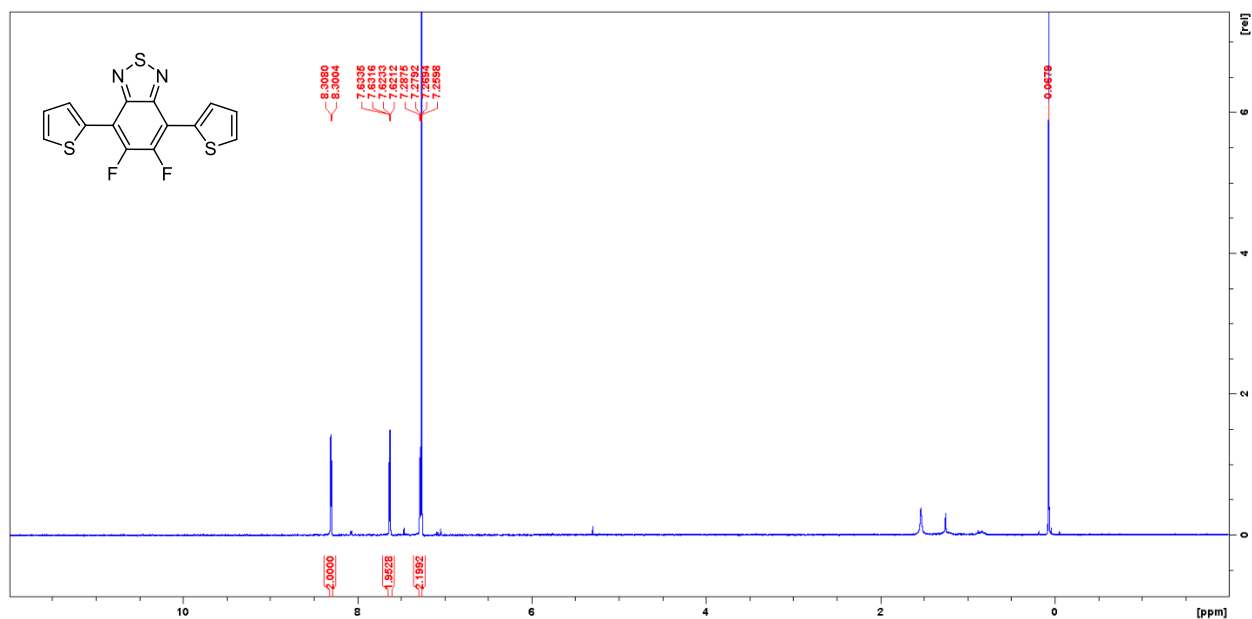


Figure 5.13 5,6-Difluoro-4,7-dithieno-2,1,3-benzothiadiazole (6) ^1H NMR.

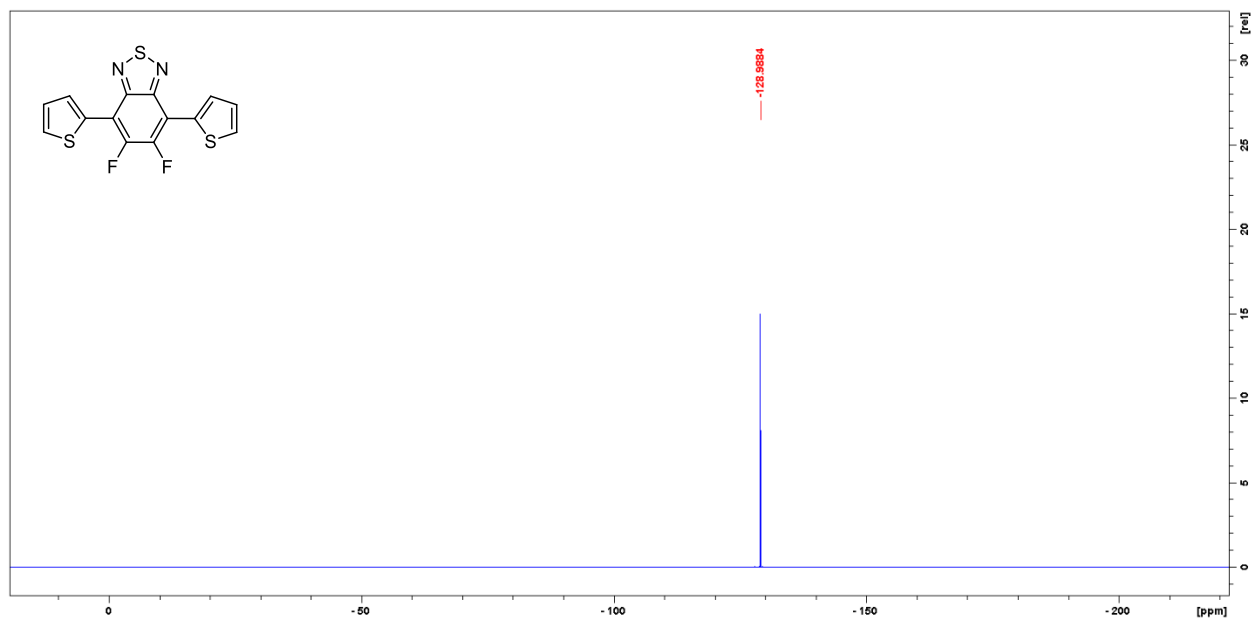


Figure 5.14 5,6-Difluoro-4,7-dithieno-2,1,3-benzothiadiazole (6) ^{19}F NMR.

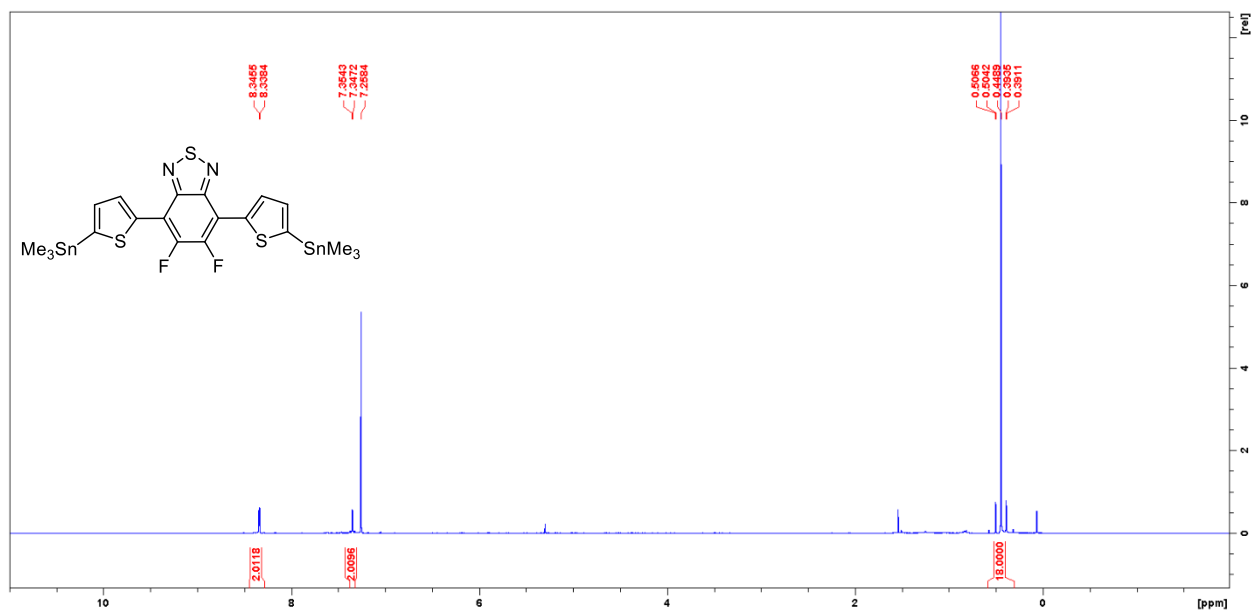


Figure 5.15 5,6-Difluoro-4,7-bis(5-(trimethylstannyl)thiophen-2-yl)-2,1,3-benzothiadiazole (7) ¹H NMR.

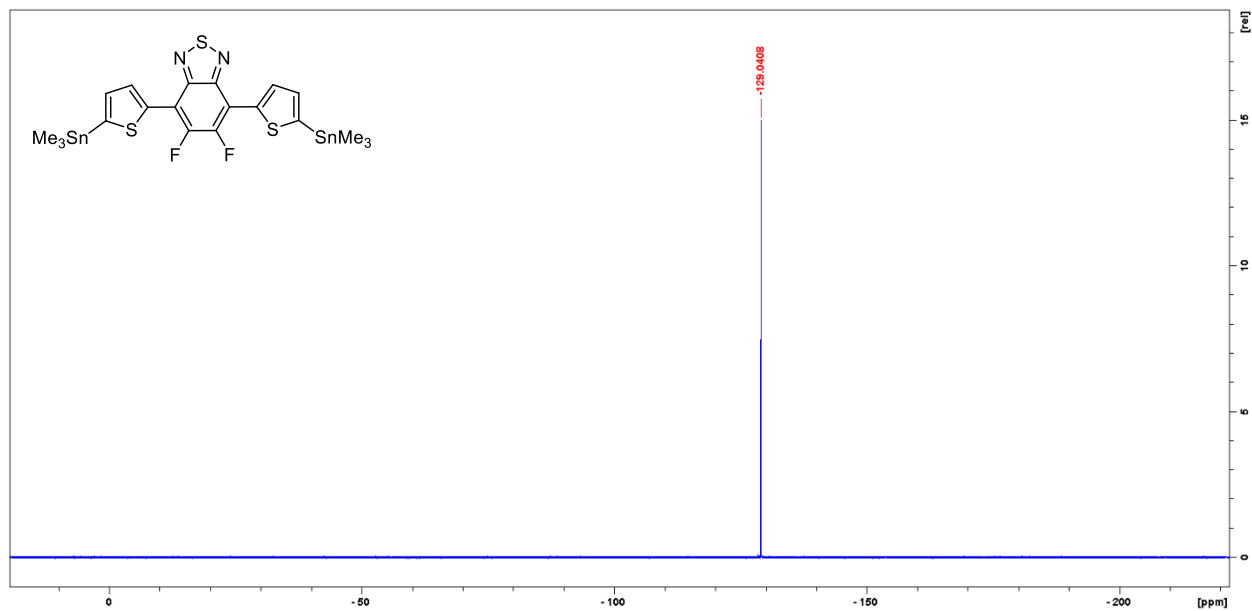


Figure 5.16 5,6-Difluoro-4,7-bis(5-(trimethylstannyl)thiophen-2-yl)-2,1,3-benzothiadiazole (7) ¹⁹F NMR.

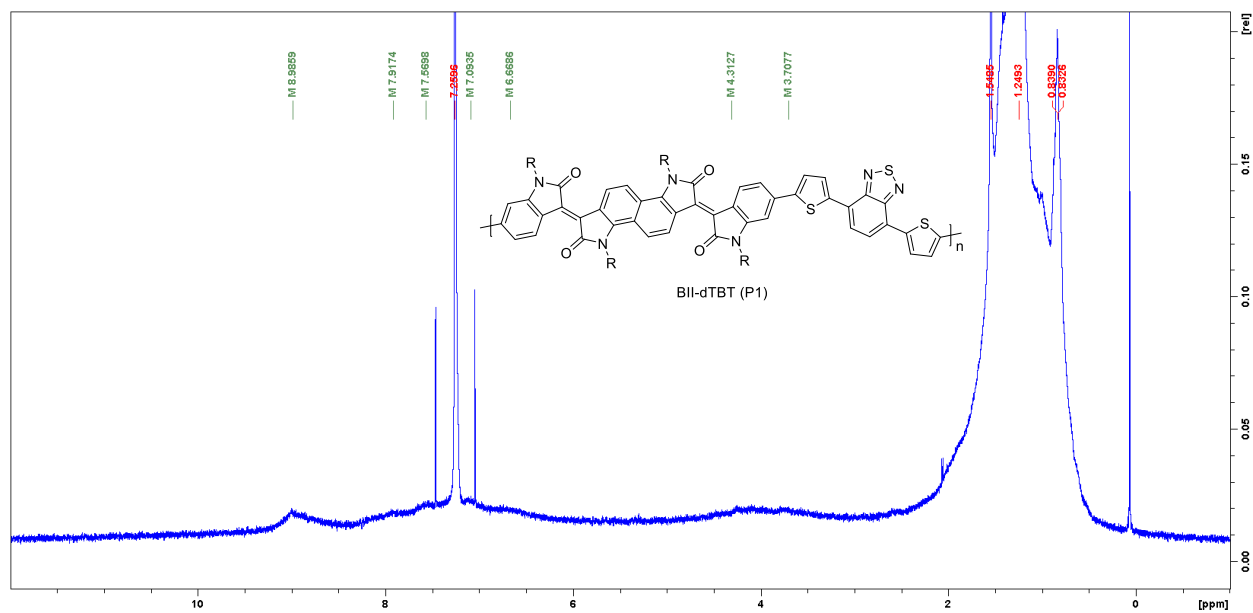


Figure 5.17 Poly(bisindigo-dithienylbenzothiadiazole) P1(H) ^1H NMR.

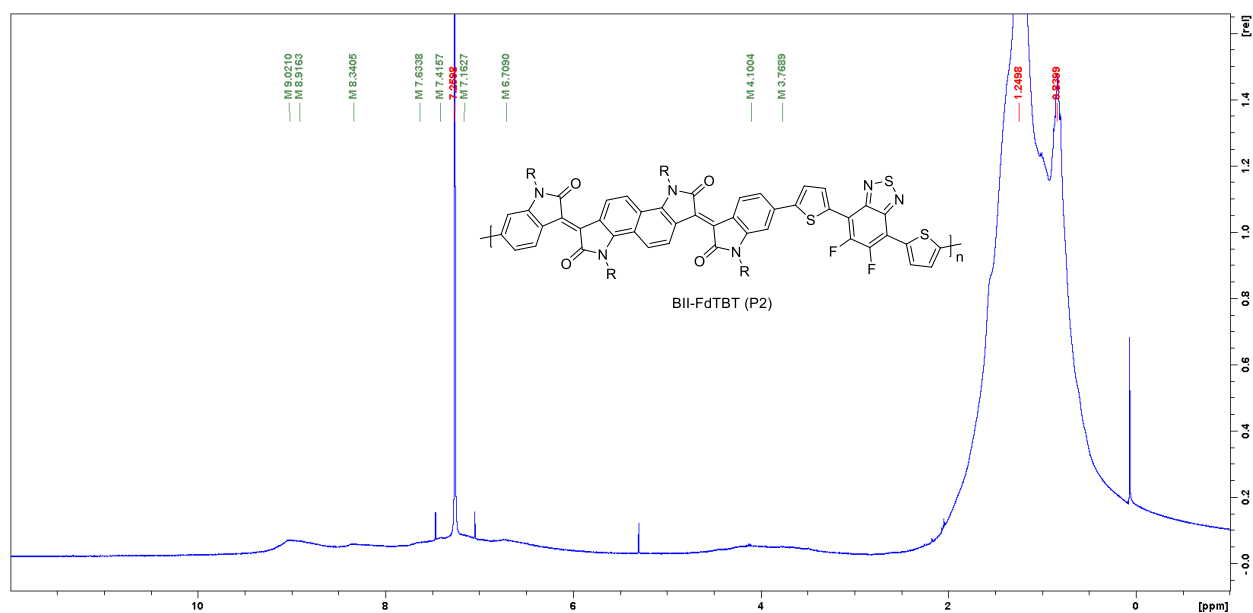


Figure 5.18 Poly(bisindigo-difluoro, dithienylbenzothiadiazole) P2(F) ^1H NMR

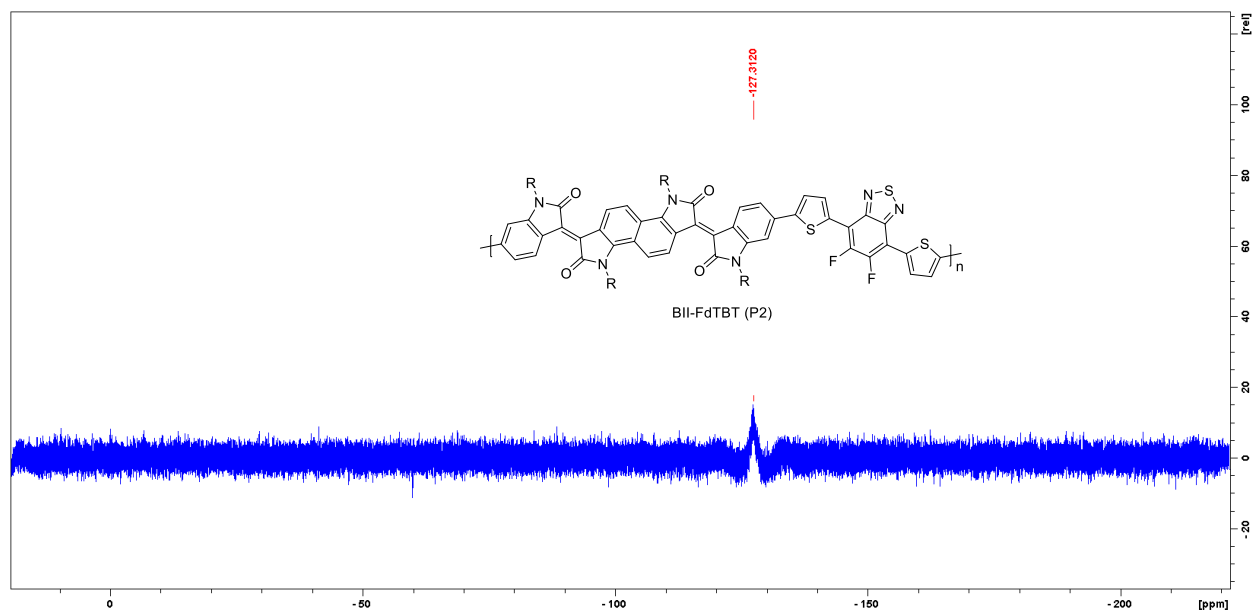


Figure 5.19 Poly(bisindigo-difluoro, dithienylbenzothiadiazole) P2(F) ^{19}F NMR.

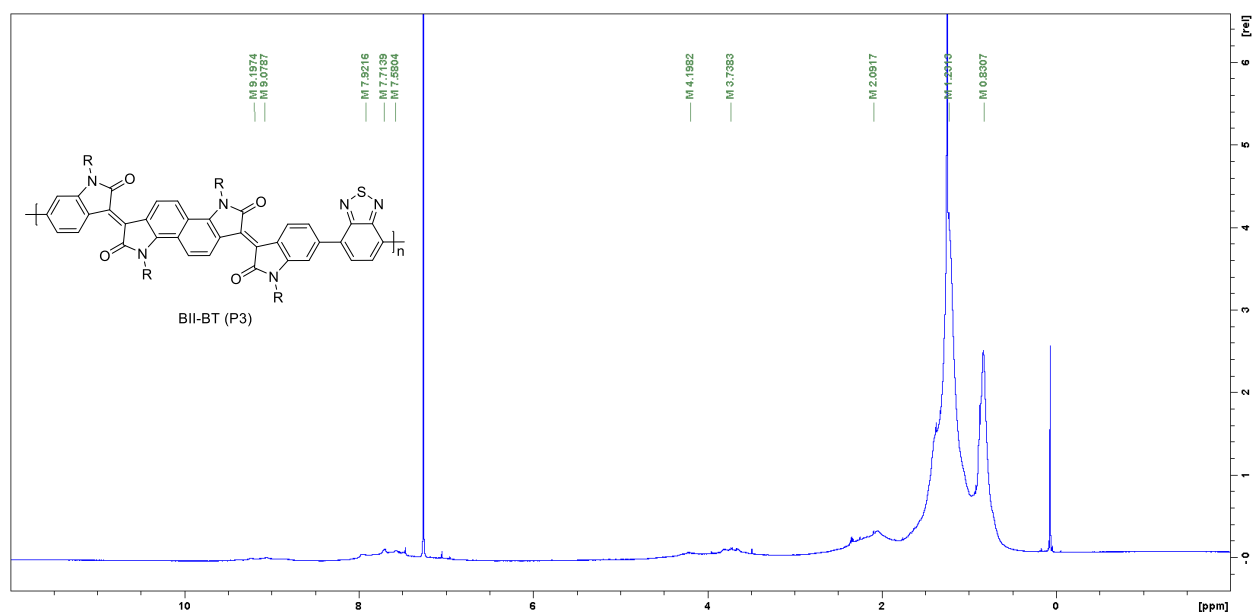


Figure 5.20 Poly(bisindigo-benzothiadiazole) P3(B) ^1H NMR.

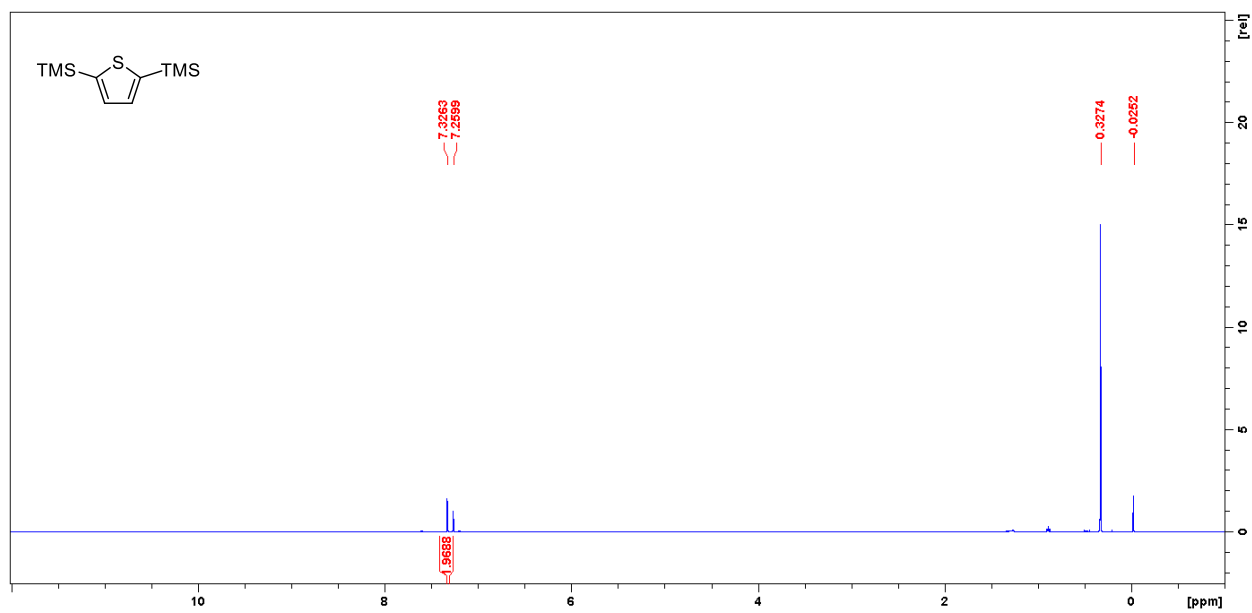


Figure 5.21 2,5-Trimethylsilylthiophene (8) ^1H NMR.

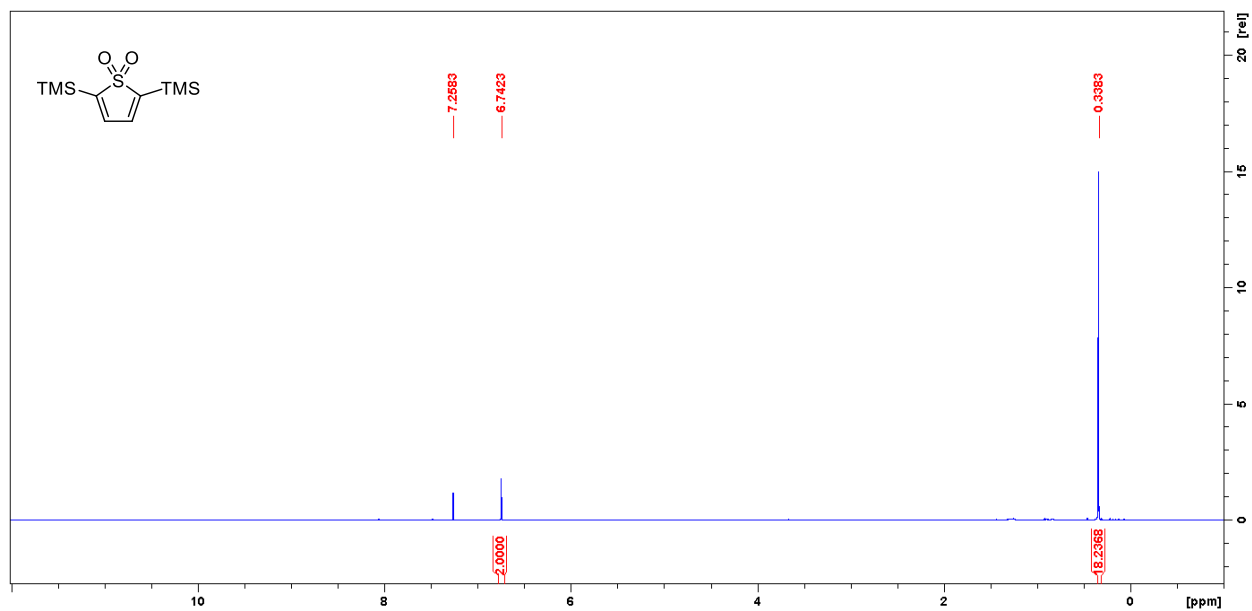


Figure 5.22 2,5-Trimethylsilylthiophene-*S,S*-dioxide (9) ^1H NMR.

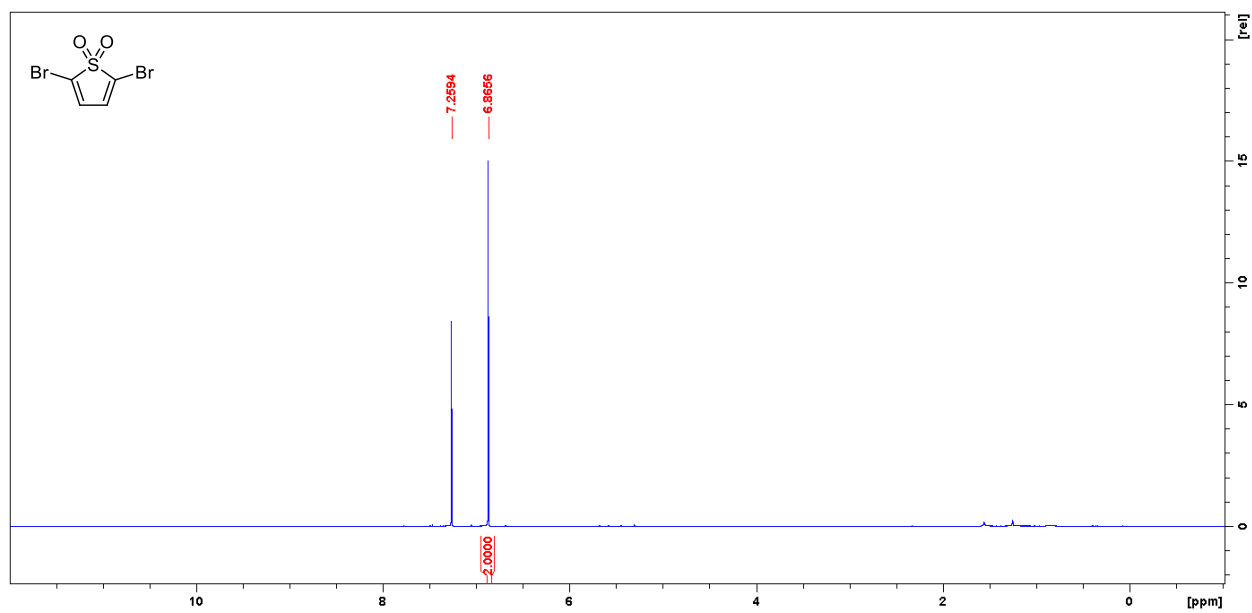


Figure 5.23 2,5-Dibromothiophene-*S,S*-dioxide (10) ^1H NMR.

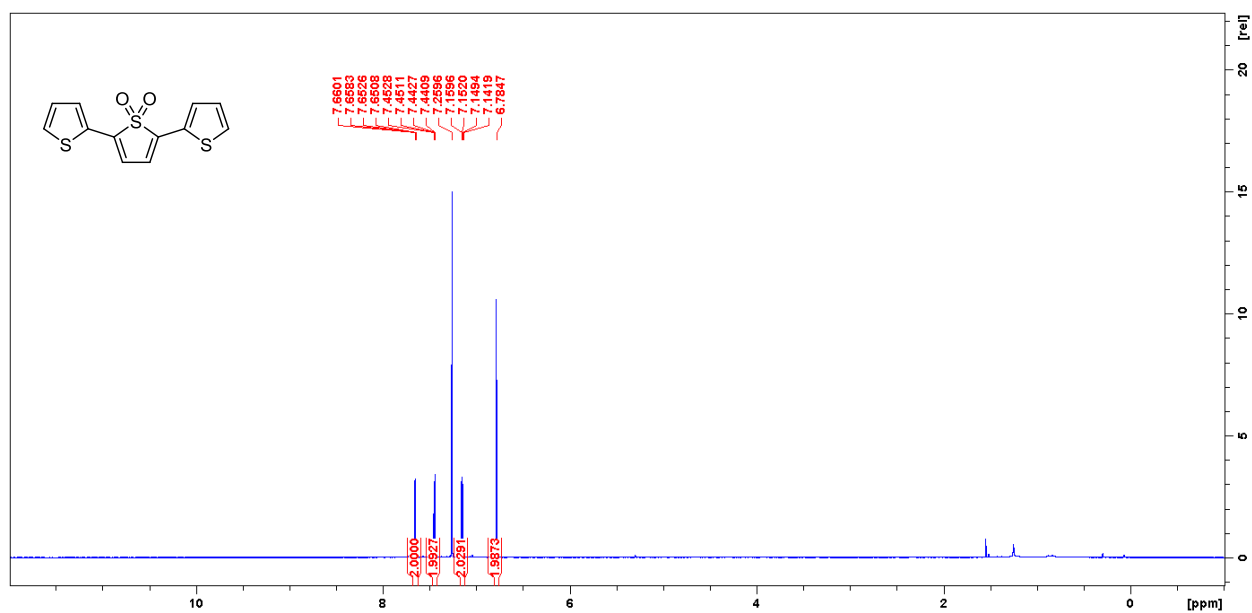


Figure 5.24 2,5-Thienylthiophene-*S,S*-dioxide (11) ^1H NMR.

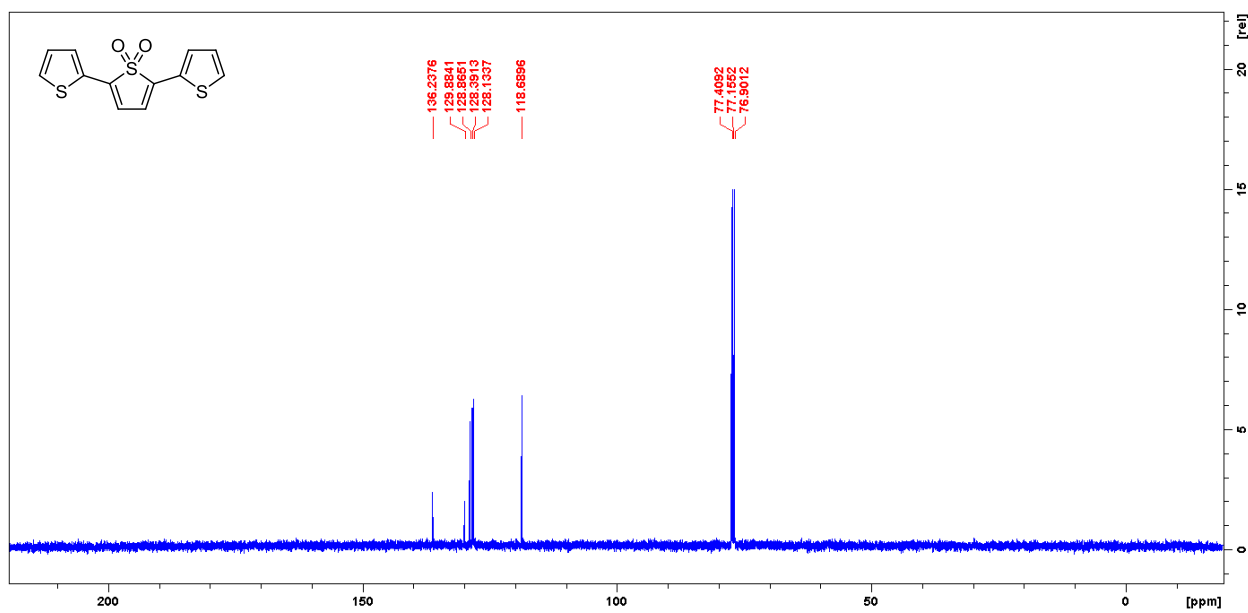


Figure 5.25 2,5-Thienylthiophene-*S,S*-dioxide (11) ¹³C NMR.

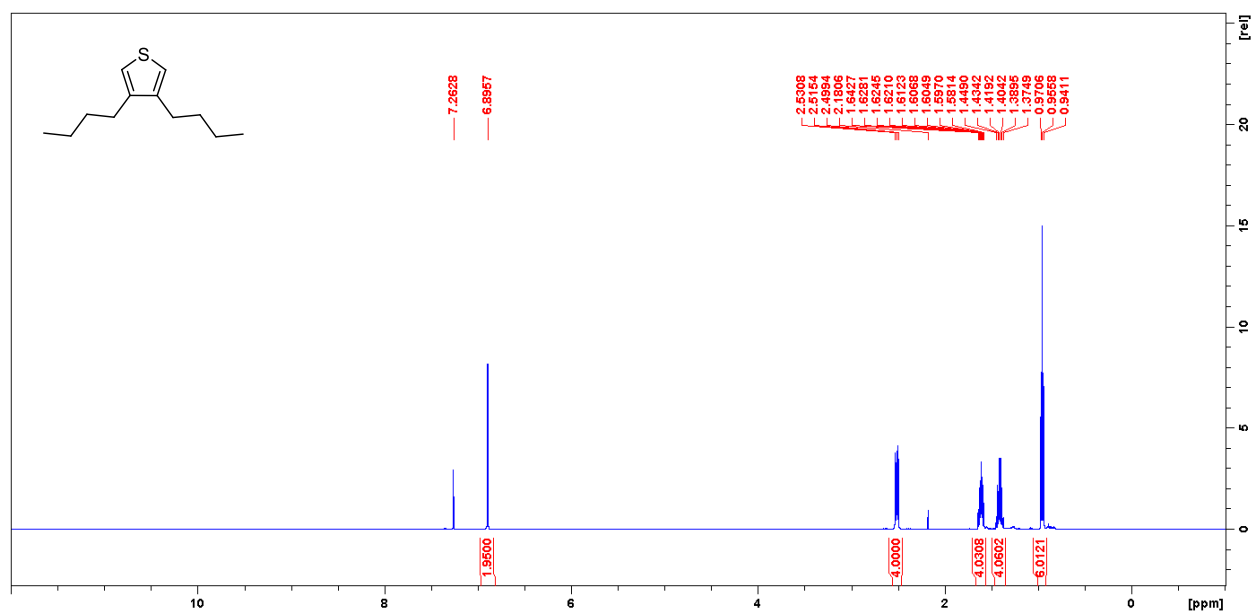


Figure 5.26 3,4-Dibutylthiophene (12) ¹H NMR.

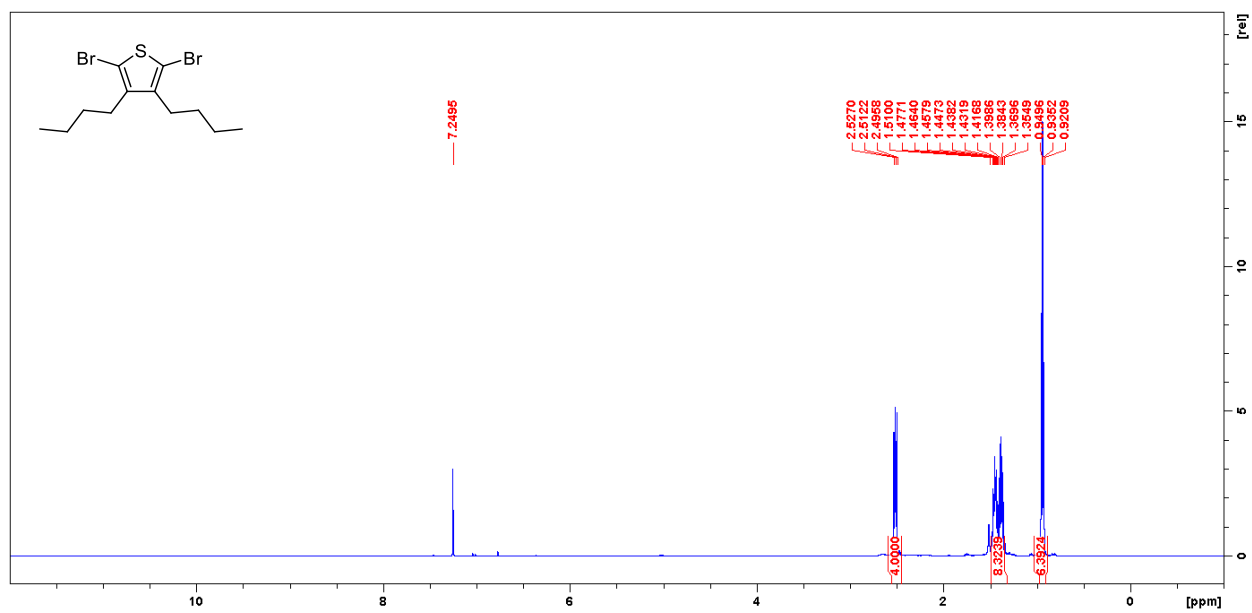


Figure 5.27 2,5-Dibromo-3,4-dibutylthiophene (13) ¹H NMR.

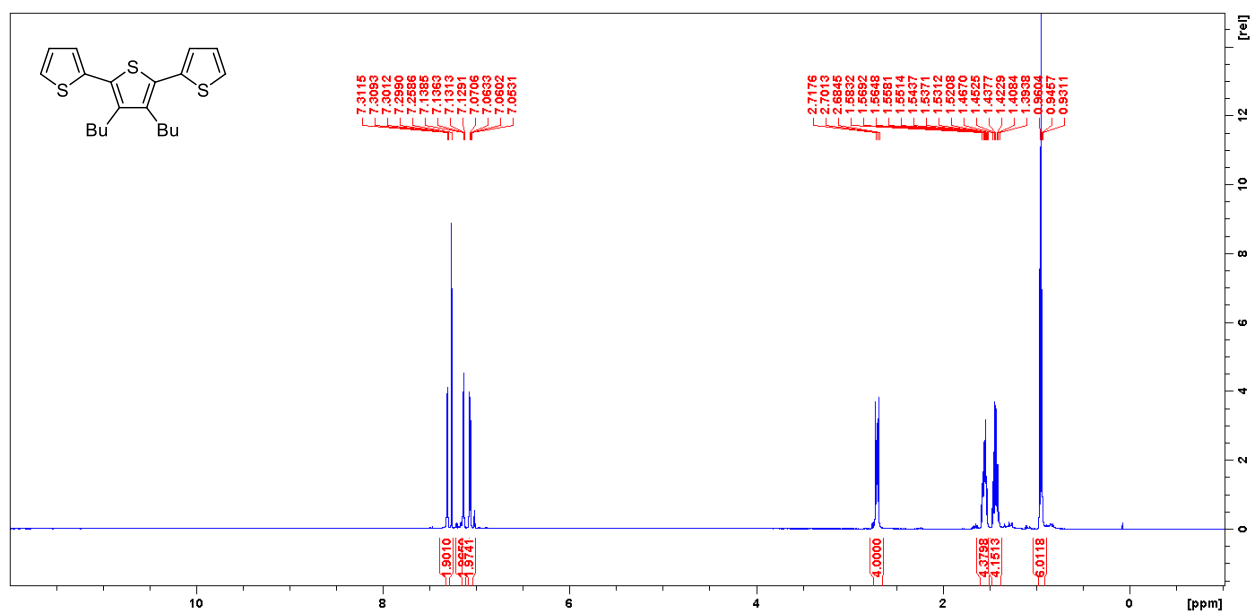


Figure 5.28 3',4'-Dibutylterthiophene (14) ¹H NMR.

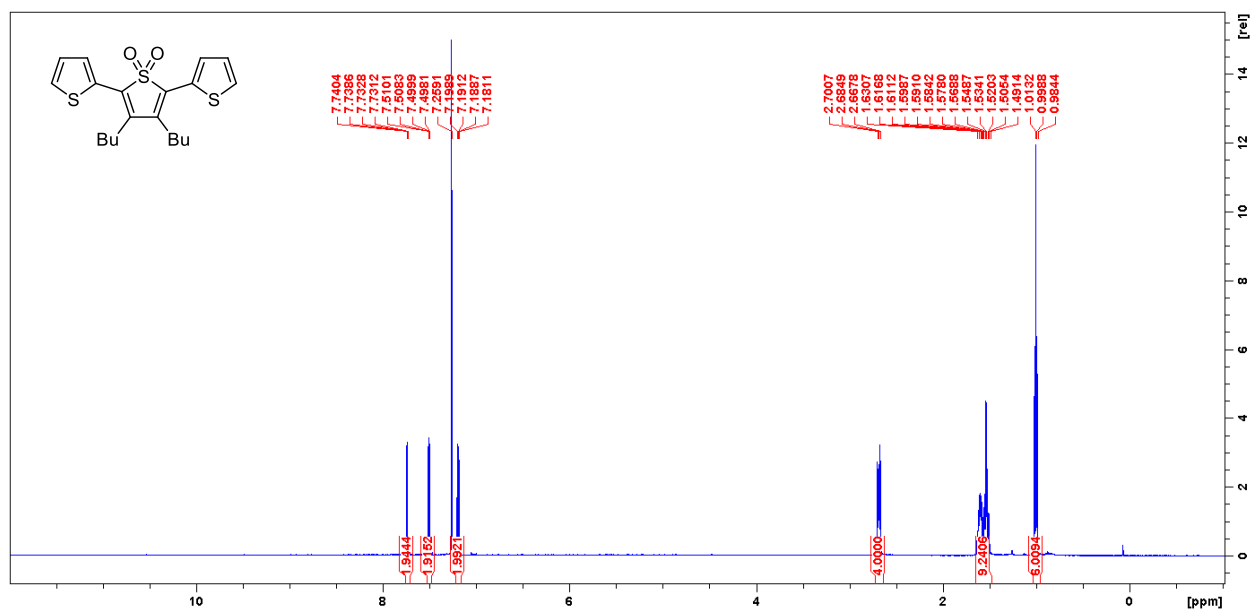


Figure 5.29 3,4'-Dibutylterthiophene-*S,S'*-dioxide (15) ¹H NMR.

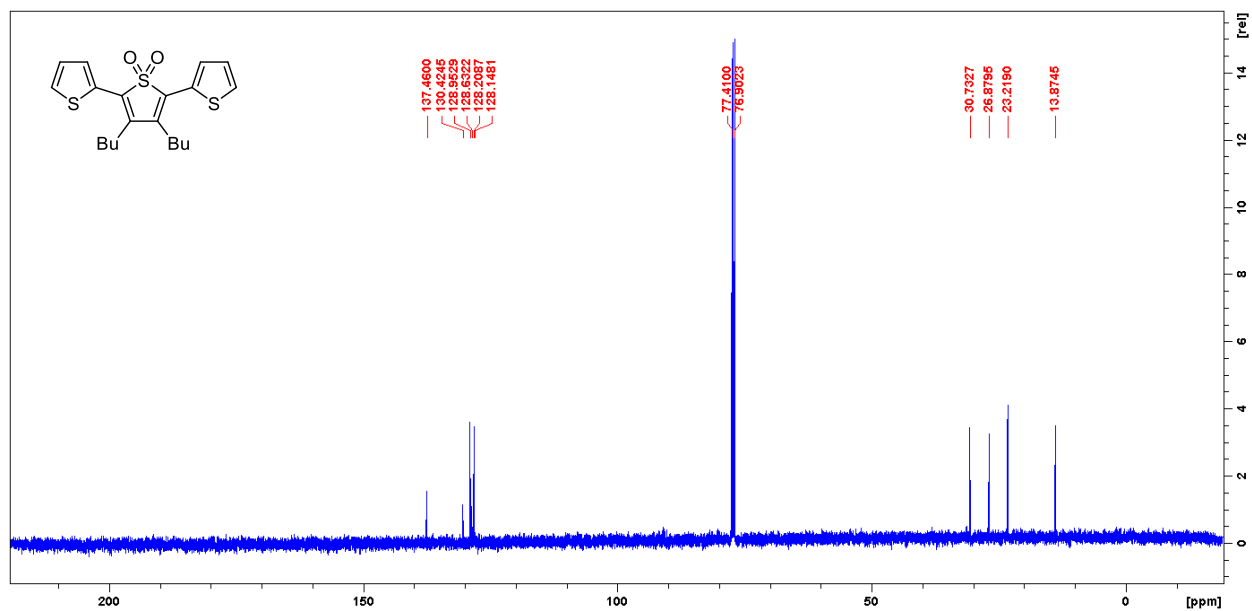


Figure 5.30 3,4'-Dibutylterthiophene-*S,S'*-dioxide (15) ¹³C NMR.

Chapter 6 – References

- (1) Heeger, Alan J. ; MacDiarmid, Alan G. ; Shirakawa, H. Advanced Information - The Nobel Prize in Chemistry 2000. **2000**, 1–16.
- (2) Mazzio, K. A.; Luscombe, C. K. The Future of Organic Photovoltaics. *Chem. Soc. Rev.* **2015**, *44*, 78–90.
- (3) Kim, Y.; Lim, E. Development of Polymer Acceptors for Organic Photovoltaic Cells. *Polymers* **2014**, *6*, 382–407.
- (4) Quinn, J. T. E.; Zhu, J.; Li, X.; Wang, J.; Li, Y. Recent Progress in the Development of N-Type Organic Semiconductors for Organic Field Effect Transistors. *J. Mater. Chem. C* **2017**, *5*, 8654–8681.
- (5) Surya, S. G.; Raval, H. N.; Ahmad, R.; Sonar, P.; Salama, K. N.; Rao, V. R. Organic Field Effect Transistors (OFETs) in Environmental Sensing and Health Monitoring: A Review. *Trends Anal. Chem.* **2019**, *111*, 27–36.
- (6) Shi, W.; Guo, Y.; Liu, Y. When Flexible Organic Field-Effect Transistors Meet Biomimetics: A Prospective View of the Internet of Things. *Adv. Mater.* **2019**, 1901493.
- (7) Bredas, J. L.; Calbert, J. P.; Filho, D. A. S.; Cornil, J. Organic Semiconductors: A Theoretical Characterization of the Basic Parameters Governing Charge Transport. *Proc. Natl. Acad. Sci. U. S. A.* **2002**, *99*, 5804–5809.
- (8) Noriega, R.; Salleo, A. Charge Transport Theories in Organic Semiconductors. In *Organic Electronics II*; Wiley-VCH Verlag GmbH & Co. KGaA: Weinheim, Germany, 2012; pp 67–104.
- (9) Noriega, R.; Rivnay, J.; Vandewal, K.; Koch, F. P. V.; Stingelin, N.; Smith, P.; Toney, M. F.; Salleo, A. A General Relationship between Disorder, Aggregation and Charge Transport in Conjugated Polymers. *Nat. Mater.* **2013**, *12*, 1038–1044.
- (10) Shirakawa, H. Synthesis and Characterization of Highly Conducting Polyacetylene. *Synth. Met.* **1995**, *69*, 3–8.
- (11) Gorman, C. B.; Ginsburg, E. J.; Grubbs, R. H. Soluble, Highly Conjugated Derivatives of

- Polyacetylene from the Ring-Opening Metathesis Polymerization of Monosubstituted Cyclooctatetraenes: Synthesis and the Relationship between Polymer Structure and Physical Properties. *J. Am. Chem. Soc.* **1993**, *115*, 1397–1409.
- (12) Loewe, R. S.; Khersonsky, S. M.; McCullough, R. D. A Simple Method to Prepare Head-to-Tail Coupled, Regioregular Poly(3-Alkylthiophenes) Using Grignard Metathesis. *Adv. Mater.* **1999**, *11*, 250–253.
 - (13) Geoghegan, M.; Hadziioannou, G. Synthesis and Macromolecular Design. In *Polymer Electronics*; 2013; pp 98–130.
 - (14) Cordovilla, C.; Bartolomé, C.; Martínez-Ilarduya, J. M.; Espinet, P. The Stille Reaction, 38 Years Later. *ACS Catal.* **2015**, *5*, 3040–3053.
 - (15) Amatore, C.; Jutand, A.; Leduc, G. The Triple Role of Fluoride Ions in Palladium-Catalyzed Suzuki-Miyaura Reactions: Unprecedented Transmetalation from [ArPdFL₂] Complexes. *Angew. Chemie - Int. Ed.* **2012**, *51*, 1379–1382.
 - (16) Lennox, A. J. J.; Lloyd-Jones, G. C. Transmetalation in the Suzuki-Miyaura Coupling: The Fork in the Trail. *Angew. Chemie - Int. Ed.* **2013**, *52*, 7362–7370.
 - (17) Brookins, R. N.; Schanze, K. S.; Reynolds, J. R. Base-Free Suzuki Polymerization for the Synthesis of Polyfluorenes Functionalized with Carboxylic Acids. *Macromolecules* **2007**, *40*, 3524–3526.
 - (18) Lee, J.; Han, A.-R.; Lee, S. M.; Yoo, D.; Oh, J. H.; Yang, C. Siloxane-Based Hybrid Semiconducting Polymers Prepared by Fluoride-Mediated Suzuki Polymerization. *Angew. Chemie - Int. Ed.* **2015**, *54*, 4657–4660.
 - (19) Bura, T.; Blaskovits, J. T.; Leclerc, M. Direct (Hetero)Arylation Polymerization: Trends and Perspectives. *J. Am. Chem. Soc.* **2016**, *138*, 10056–10071.
 - (20) Pouliot, J. R.; Grenier, F.; Blaskovits, J. T.; Beaupré, S.; Leclerc, M. Direct (Hetero)Arylation Polymerization: Simplicity for Conjugated Polymer Synthesis. *Chem. Rev.* **2016**, *116*, 14225–14274.
 - (21) Bura, T.; Beaupré, S.; Légaré, M. A.; Quinn, J.; Rochette, E.; Blaskovits, J. T.; Fontaine, F.

- G.; Pron, A.; Li, Y.; Leclerc, M. Direct Heteroarylation Polymerization: Guidelines for Defect-Free Conjugated Polymers. *Chem. Sci.* **2017**, *8*, 3913–3925.
- (22) Blaskovits, J. T.; Leclerc, M. C–H Activation as a Shortcut to Conjugated Polymer Synthesis. *Macromol. Rapid Commun.* **2019**, *40*, 1800512.
- (23) Blaskovits, J. T.; Johnson, P. A.; Leclerc, M. Mechanistic Origin of β -Defect Formation in Thiophene-Based Polymers Prepared by Direct (Hetero)Arylation. *Macromolecules* **2018**, *51*, 8100–8113.
- (24) Onwubiko, A.; Yue, W.; Jellett, C.; Xiao, M.; Chen, H. Y.; Ravva, M. K.; Hanifi, D. A.; Knall, A. C.; Purushothaman, B.; Nikolka, M.; Flores, J. C.; Salleo, A.; Bredas, J. L.; Sirringhaus, H.; Hayoz, P.; McCulloch, I. Fused Electron Deficient Semiconducting Polymers for Air Stable Electron Transport. *Nat. Commun.* **2018**, *9*, 416.
- (25) Zhang, G.; Dai, Y.; Liu, Y.; Liu, J.; Lu, H.; Qiu, L.; Cho, K. Facile Green Synthesis of Isoindigo-Based Conjugated Polymers Using Aldol Polycondensation. *Polym. Chem.* **2017**, *8*, 3448–3456.
- (26) Ganguly, A.; He, K.; Hendsbee, A. D.; Abdelsamie, M.; Bennett, R. N.; Li, Y.; Toney, M. F.; Kelly, T. L. Synthesis of Poly(Bisisoindigo) Using a Metal-Free Aldol Polymerization for Thin-Film Transistor Applications. *ACS Appl. Mater. Interfaces* **2020**, *12*, 14265–14271.
- (27) Klauk, H. Organic Thin-Film Transistors. *Chem. Soc. Rev.* **2010**, *39*, 2643–2666.
- (28) Sirringhaus, H. 25th Anniversary Article: Organic Field-Effect Transistors: The Path beyond Amorphous Silicon. *Adv. Mater.* **2014**, *26*, 1319–1335.
- (29) Paterson, A. F.; Singh, S.; Fallon, K. J.; Hodsdon, T.; Han, Y.; Schroeder, B. C.; Bronstein, H.; Heeney, M.; McCulloch, I.; Anthopoulos, T. D. Recent Progress in High-Mobility Organic Transistors: A Reality Check. *Adv. Mater.* **2018**, *1801079*, 1–33.
- (30) Zschieschang, U.; Klauk, H. Organic Transistors on Paper: A Brief Review. *J. Mater. Chem. C* **2019**, *7*, 5522–5533.
- (31) Newman, C. R.; Frisbie, C. D.; Da Silva Filho, D. A.; Bredas, J. L.; Ewbank, P. C.; Mann, K. R.; Da Silva Filho, D. A.; Bredas, J. L.; Ewbank, P. C.; Mann, K. R. Introduction to

- Organic Thin Film Transistors and Design of N-Channel Organic Semiconductors. *Chem. Mater.* **2004**, *16*, 4436–4451.
- (32) Noh, Y.-Y.; Chang, J.; Cheng, X.; Baeg, K.-J. Polymer Field-Effect Transistors. In *Polymer Electronics*; 2013; pp 65–108.
- (33) Facchetti, A. Conjugated Semiconductors for Organic N-Channel Transistors and Complementary Circuits. In *Organic Electronics II: More Materials and Applications*; 2012; pp 137–195.
- (34) Wang, Y.; Huang, X.; Li, T.; Li, L.; Guo, X.; Jiang, P. Polymer-Based Gate Dielectrics for Organic Field-Effect Transistors. *Chem. Mater.* **2019**, *31*, 2212–2240.
- (35) Zhao, W.; Jie, J.; Wei, Q.; Lu, Z.; Jia, R.; Deng, W.; Zhang, X.; Zhang, X. A Facile Method for the Growth of Organic Semiconductor Single Crystal Arrays on Polymer Dielectric toward Flexible Field-Effect Transistors. *Adv. Funct. Mater.* **2019**, *29*, 1902494.
- (36) Yi, H. T.; Payne, M. M.; Anthony, J. E.; Podzorov, V. Ultra-Flexible Solution-Processed Organic Field-Effect Transistors. *Nat. Commun.* **2012**, *3*, 1257–1259.
- (37) Klauk, H. Will We See Gigahertz Organic Transistors? *Adv. Electron. Mater.* **2018**, *4*, 1–8.
- (38) Chan, P. K. L. The Motivation for and Challenges to Scaling Down Organic Field-Effect Transistors. *Adv. Electron. Mater.* **2019**, *5*, 1900029.
- (39) Neaman, D. E. *Semiconductor Physics and Devices*, Third.; McGraw Hill, 2003.
- (40) Lamport, Z. A.; Haneef, H. F.; Anand, S.; Waldrip, M.; Jurchescu, O. D. Tutorial: Organic Field-Effect Transistors: Materials, Structure and Operation. *J. Appl. Phys.* **2018**, *124*, 071101.
- (41) Gargi, D.; Kline, R. J.; DeLongchamp, D. M.; Fischer, D. A.; Toney, M. F.; O'Connor, B. T.; O'Connor, B. T. Charge Transport in Highly Face-On Poly(3-Hexylthiophene) Films. *J. Phys. Chem. C* **2013**, *117*, 17421–17428.
- (42) Ya-Rui, S.; Hui-Ling, W.; Ya-Ting, S.; Yu-Fang, L. Theoretical Study of the Charge Transport Mechanism in π -Stacked Systems of Organic Semiconductor Crystals. *CrystEngComm* **2017**, *19*, 6008–6019.

- (43) Xia, Y.; Frisbie, C. D. Low-Voltage Electrolyte-Gated OTFTs and Their Applications. In *Organic Electronics II: More Materials and Applications*; 2012; pp 197–233.
- (44) Yu, B.-S.; Jeon, J.-Y.; Kang, B.-C.; Lee, W.; Kim, Y.-H.; Ha, T.-J. Wearable 1 V Operating Thin-Film Transistors with Solution-Processed Metal-Oxide Semiconductor and Dielectric Films Fabricated by Deep Ultra-Violet Photo Annealing at Low Temperature. *Sci. Rep.* **2019**, *9*, 8416.
- (45) Wang, Y.; Hasegawa, T.; Matsumoto, H.; Mori, T.; Michinobu, T. High-Performance n-Channel Organic Transistors Using High-Molecular-Weight Electron-Deficient Copolymers and Amine-Tailed Self-Assembled Monolayers. *Adv. Mater.* **2018**, *30*, 1707164.
- (46) Rivnay, J.; Inal, S.; Salleo, A.; Owens, R. M.; Berggren, M.; Malliaras, G. G. Organic Electrochemical Transistors. *Nat. Rev. Mater.* **2018**, *3*, 17086.
- (47) Paterson, A. F.; Anthopoulos, T. D. Enabling Thin-Film Transistor Technologies and the Device Metrics That Matter. *Nat. Commun.* **2018**, *9*, 5264.
- (48) Yan, C.; Barlow, S.; Wang, Z.; Yan, H.; Jen, A. K.-Y.; Marder, S. R.; Zhan, X. Non-Fullerene Acceptors for Organic Solar Cells. *Nat. Rev. Mater.* **2018**, *3*, 18003.
- (49) Kim, M.; Ryu, S. U.; Park, S. A.; Choi, K.; Kim, T.; Chung, D.; Park, T. Donor–Acceptor-Conjugated Polymer for High-Performance Organic Field-Effect Transistors: A Progress Report. *Adv. Funct. Mater.* **2019**, 1904545.
- (50) de Leeuw, D. M.; Simenon, M. M. J.; Brown, a. R.; Einerhand, R. E. F. Stability of N-Type Doped Conducting Polymers and Consequences for Polymeric Microelectronic Devices. *Synth. Met.* **1997**, *87*, 53–59.
- (51) Di Pietro, R.; Fazzi, D.; Kehoe, T. B.; Sirringhaus, H. Spectroscopic Investigation of Oxygen- and Water-Induced Electron Trapping and Charge Transport Instabilities in n-Type Polymer Semiconductors. *J. Am. Chem. Soc.* **2012**, *134*, 14877–14889.
- (52) Yoo, D.; Luo, X.; Hasegawa, T.; Ashizawa, M.; Kawamoto, T.; Masunaga, H.; Ohta, N.; Matsumoto, H.; Mei, J.; Mori, T. N-Type Organic Field-Effect Transistors Based on Bisthienoisatin Derivatives. *ACS Appl. Electron. Mater.* **2019**, *1*, 764–771.

- (53) Li, G.; Chang, W.-H.; Yang, Y. Low-Bandgap Conjugated Polymers Enabling Solution-Processable Tandem Solar Cells. *Nat. Rev. Mater.* **2017**, *2*, 17043.
- (54) Steingruber, E. Indigo and Indigo Colorants. *Ullman's Encyclopedia of Industrial Chemistry*; 2000; pp 673–680.
- (55) Maugard, T.; Enaud, E.; Choisy, P.; Marie Dominique, L. Identification of an Indigo Precursor from Leaves of *Isatis Tinctoria* (Woad). *Phytochemistry* **2001**, *58*, 897–904.
- (56) Deng, P.; Zhang, Q. Recent Developments on Isoindigo-Based Conjugated Polymers. *Polym. Chem.* **2014**, *5*, 3298–3305.
- (57) Wang, E.; Mammo, W.; Andersson, M. R. 25th Anniversary Article: Isoindigo-Based Polymers and Small Molecules for Bulk Heterojunction Solar Cells and Field Effect Transistors. *Adv. Mater.* **2014**, *26*, 1801–1826.
- (58) Mei, J.; Graham, K. R.; Stalder, R.; Reynolds, J. R. Synthesis of Isoindigo-Based Oligothiophenes for Molecular Bulk Heterojunction Solar Cells. *Org. Lett.* **2010**, *12*, 660–663.
- (59) Lei, T.; Cao, Y.; Fan, Y.; Liu, C. J.; Yuan, S. C.; Pei, J. High-Performance Air-Stable Organic Field-Effect Transistors: Isoindigo-Based Conjugated Polymers. *J. Am. Chem. Soc.* **2011**, *133*, 6099–6101.
- (60) Lei, T.; Cao, Y.; Zhou, X.; Peng, Y.; Bian, J.; Pei, J. Systematic Investigation of Isoindigo-Based Polymeric Field-Effect Transistors: Design Strategy and Impact of Polymer Symmetry and Backbone Curvature. *Chem. Mater.* **2012**, *24*, 1762–1770.
- (61) Lei, T.; Dou, J. H.; Pei, J. Influence of Alkyl Chain Branching Positions on the Hole Mobilities of Polymer Thin-Film Transistors. *Adv. Mater.* **2012**, *24*, 6457–6461.
- (62) Stalder, R.; Mei, J.; Subbiah, J.; Grand, C.; Estrada, L. A.; So, F.; Reynolds, J. R. N-Type Conjugated Polyisoindigos. *Macromolecules* **2011**, *44*, 6303–6310.
- (63) Kim, G.; Han, A.-R. R.; Lee, H. R.; Lee, J.; Oh, J. H.; Yang, C. Acceptor-Acceptor Type Isoindigo-Based Copolymers for High-Performance n-Channel Field-Effect Transistors. *Chem. Commun.* **2014**, *50*, 2180–2183.

- (64) Grenier, F.; Berrouard, P.; Pouliot, J.-R.; Tseng, H.-R.; Heeger, A. J.; Leclerc, M. Synthesis of New N-Type Isoindigo Copolymers. *Polym. Chem.* **2013**, *4*, 1836.
- (65) Randell, N. M.; Kelly, T. L. Recent Advances in Isoindigo-Inspired Organic Semiconductors. *Chem. Rec.* **2019**, *18*, 1–17.
- (66) Li, J.-L.; Cao, J.-J.; Duan, L.-L.; Zhang, H.-L. Evolution of Isoindigo-Based Electron-Deficient Units for Organic Electronics: From Natural Dyes to Organic Semiconductors. *Asian J. Org. Chem.* **2018**, *7*, 2147–2160.
- (67) Stalder, R.; Mei, J.; Graham, K. R.; Estrada, L. A.; Reynolds, J. R. Isoindigo, a Versatile Electron-Deficient Unit for High-Performance Organic Electronics. *Chem. Mater.* **2014**, *26*, 664–678.
- (68) Yan, Z.; Sun, B.; Li, Y. Novel Stable (3E,7E)-3,7-Bis(2-Oxoindolin-3-Ylidene)Benzo[1,2-b:4,5-B']Difuran-2,6(3H,7H)-Dione Based Donor–Acceptor Polymer Semiconductors for n-Type Organic Thin Film Transistors. *Chem. Commun.* **2013**, *49*, 3790.
- (69) Lei, T.; Dou, J.-H.; Cao, X.-Y.; Wang, J.-Y.; Pei, J. Electron-Deficient Poly(p-Phenylene Vinylene) Provides Electron Mobility over $1\text{ cm}^2\text{ V}^{-1}\text{ s}^{-1}$ under Ambient Conditions. *J. Am. Chem. Soc.* **2013**, *135*, 12168–12171.
- (70) Lei, T.; Dou, J.-H.; Cao, X.-Y.; Wang, J.-Y.; Pei, J. A BDOPV-Based Donor-Acceptor Polymer for High-Performance n-Type and Oxygen-Doped Ambipolar Field-Effect Transistors. *Adv. Mater.* **2013**, *25*, 6589–6593.
- (71) Zheng, Y.-Q.; Lei, T.; Dou, J.-H.; Xia, X.; Wang, J.-Y.; Liu, C.-J.; Pei, J. Strong Electron-Deficient Polymers Lead to High Electron Mobility in Air and Their Morphology-Dependent Transport Behaviors. *Adv. Mater.* **2016**, *28*, 7213–7219.
- (72) Dai, Y. Z.; Ai, N.; Lu, Y.; Zheng, Y. Q.; Dou, J. H.; Shi, K.; Lei, T.; Wang, J. Y.; Pei, J. Embedding Electron-Deficient Nitrogen Atoms in Polymer Backbone towards High Performance n-Type Polymer Field-Effect Transistors. *Chem. Sci.* **2016**, *7*, 5753–5757.
- (73) Deng, Y.; Sun, B.; He, Y.; Quinn, J.; Guo, C.; Li, Y. Thiophene- S , S -Dioxidized Indophenine: A Quinoid-Type Building Block with High Electron Affinity for Constructing n-Type Polymer Semiconductors with Narrow Band Gaps. *Angew. Chemie Int. - Ed.* **2016**,

55, 3459–3462.

- (74) Deng, Y.; Sun, B.; Quinn, J.; He, Y.; Ellard, J.; Guo, C.; Li, Y. Thiophene-S,S-Dioxidized Indophenines as High Performance n-Type Organic Semiconductors for Thin Film Transistors. *RSC Adv.* **2016**, *6*, 45410–45418.
- (75) Deng, Y.; Quinn, J.; Sun, B.; He, Y.; Ellard, J.; Li, Y. Thiophene-S,S-Dioxidized Indophenine (IDTO) Based Donor-Acceptor Polymers for n-Channel Organic Thin Film Transistors. *RSC Adv.* **2016**, *6*, 34849–34854.
- (76) Tormos, G. V.; Belmore, K. A.; Cava, M. P. The Indophenine Reaction Revisited. Properties of a Soluble Dialkyl Derivative. *J. Am. Chem. Soc.* **1993**, *115*, 11512–11515.
- (77) Deng, Y.; Sun, B.; He, Y.; Quinn, J.; Guo, C.; Li, Y. (3E,8E)-3,8-Bis(2-Oxoindolin-3-Ylidene)Naphtho-[1,2-b:5,6-B']Difuran-2,7(3H,8H)-Dione (INDF) Based Polymers for Organic Thin-Film Transistors with Highly Balanced Ambipolar Charge Transport Characteristics. *Chem. Commun.* **2015**, *51*, 13515–13518.
- (78) Randell, N. M.; Boutin, P. C.; Kelly, T. L. Bisisoindigo: Using a Ring-Fusion Approach to Extend the Conjugation Length of Isoindigo. *J. Mater. Chem. A* **2016**, *4*, 6940–6945.
- (79) Jiang, Y.; Gao, Y.; Tian, H.; Ding, J.; Yan, D.; Geng, Y.; Wang, F. Synthesis and Characterization of Isoindigo[7,6-g]Isoindigo-Based Donor–Acceptor Conjugated Polymers. *Macromolecules* **2016**, *49*, 2135–2144.
- (80) Randell, N. M.; Radford, C. L.; Yang, J.; Quinn, J.; Hou, D.; Li, Y.; Kelly, T. L. Effect of Acceptor Unit Length and Planarity on the Optoelectronic Properties of Isoindigo–Thiophene Donor–Acceptor Polymers. *Chem. Mater.* **2018**, *30*, 4864–4873.
- (81) Jiang, Y.; Zheng, X.; Deng, Y.; Tian, H.; Ding, J.; Xie, Z.; Geng, Y.; Wang, F. Fused Isoindigo Ribbons with Absorption Bands Reaching Near-Infrared. *Angew. Chemie - Int. Ed.* **2018**, *57*, 10283–10287.
- (82) Pankow, R. M.; Gobalasingham, N. S.; Munteanu, J. D.; Thompson, B. C. Preparation of Semi-Alternating Conjugated Polymers Using Direct Arylation Polymerization (DAP) and Improvement of Photovoltaic Device Performance through Structural Variation. *J. Polym. Sci. Part A Polym. Chem.* **2017**, *55*, 3370–3380.

- (83) Mohanty, M. E.; Madhu, C.; Reddy, V. L.; Paramasivam, M.; Bangal, P. R.; Rao, V. J. Direct Observation of the Rise of Delayed Fluorescence in Dithienylbenzothiadiazole and Its Role in the Excited State Dynamics of a Donor-Acceptor-Donor Molecule. *Phys. Chem. Chem. Phys.* **2017**, *19*, 9118–9127.
- (84) Wang, L.; Huang, W.; Li, R.; Gehrig, D.; Blom, P. W. M.; Landfester, K.; Zhang, K. A. I. Structural Design Principle of Small-Molecule Organic Semiconductors for Metal-Free, Visible-Light-Promoted Photocatalysis. *Angew. Chemie - Int. Ed.* **2016**, *55*, 9783–9787.
- (85) Deng, C.; Ling, J. Amphiphilic Copolymers of Polyfluorene Methacrylates Exhibiting Tunable Emissions for Ink-Jet Printing. *Macromol. Rapid Commun.* **2016**, *37*, 1352–1356.
- (86) Biniek, L.; Chochos, C. L.; Leclerc, N.; Boyron, O.; Fall, S.; Lévêque, P.; Heiser, T. 3,6-Dialkylthieno[3,2-b]Thiophene Moiety as a Soluble and Electron Donating Unit Preserving the Coplanarity of Photovoltaic Low Band Gap Copolymers. *J. Polym. Sci. Part A Polym. Chem.* **2012**, *50*, 1861–1868.
- (87) Medlej, H.; Nourdine, A.; Awada, H.; Abbas, M.; Dagron-Lartigau, C.; Wantz, G.; Flandin, L. Fluorinated Benzothiadiazole-Based Low Band Gap Copolymers to Enhance Open-Circuit Voltage and Efficiency of Polymer Solar Cells. *Eur. Polym. J.* **2014**, *59*, 25–35.
- (88) Fan, B.; Sun, C.; Jiang, X. F.; Zhang, G.; Chen, Z.; Ying, L.; Huang, F.; Cao, Y. Improved Morphology and Efficiency of Polymer Solar Cells by Processing Donor–Acceptor Copolymer Additives. *Adv. Funct. Mater.* **2016**, *26*, 6479–6488.
- (89) Jheng, J. F.; Lai, Y. Y.; Wu, J. S.; Chao, Y. H.; Wang, C. L.; Hsu, C. S. Influences of the Non-Covalent Interaction Strength on Reaching High Solid-State Order and Device Performance of a Low Bandgap Polymer with Axisymmetrical Structural Units. *Adv. Mater.* **2013**, *25*, 2445–2451.
- (90) Wright, S. W.; Hageman, D. L.; McClure, L. D. Fluoride-Mediated Boronic Acid Coupling Reactions. *J. Org. Chem.* **1994**, *59*, 6095–6097.
- (91) Butters, M.; Harvey, J. N.; Jover, J.; Lennox, A. J. J.; Lloyd-Jones, G. C.; Murray, P. M. Aryl Trifluoroborates in Suzuki-Miyaura Coupling: The Roles of Endogenous Aryl Boronic Acid and Fluoride. *Angew. Chemie - Int. Ed.* **2010**, *49*, 5156–5160.

- (92) Weng, K.; Xue, X.; Qi, F.; Zhang, Y.; Huo, L.; Zhang, J.; Wei, D.; Wan, M.; Sun, Y. Synergistic Effects of Fluorination and Alkylthiolation on the Photovoltaic Performance of the Poly(Benzodithiophene-Benzothiadiazole) Copolymers. *ACS Appl. Energy Mater.* **2018**, *1*, 4686–4694.
- (93) Stuart, A. C.; Tumbleston, J. R.; Zhou, H.; Li, W.; Liu, S.; Ade, H.; You, W. Fluorine Substituents Reduce Charge Recombination and Drive Structure and Morphology Development in Polymer Solar Cells. *J. Am. Chem. Soc.* **2013**, *135*, 1806–1815.
- (94) Osaka, I.; Shimawaki, M.; Mori, H.; Doi, I.; Miyazaki, E.; Koganezawa, T.; Takimiya, K. Synthesis, Characterization, and Transistor and Solar Cell Applications of a Naphthobisthiadiazole-Based Semiconducting Polymer. *J. Am. Chem. Soc.* **2012**, *134*, 3498–3507.
- (95) Wang, J. L.; Yin, Q. R.; Miao, J. S.; Wu, Z.; Chang, Z. F.; Cao, Y.; Zhang, R. B.; Wang, J. Y.; Wu, H. Bin; Cao, Y. Rational Design of Small Molecular Donor for Solution-Processed Organic Photovoltaics with 8.1% Efficiency and High Fill Factor via Multiple Fluorine Substituents and Thiophene Bridge. *Adv. Funct. Mater.* **2015**, *25*, 3514–3523.
- (96) Salzner, U.; Aydin, A. Improved Prediction of Properties of π -Conjugated Oligomers with Range-Separated Hybrid Density Functionals. *J. Chem. Theory Comput.* **2011**, *7*, 2568–2583.
- (97) Zhou, H.; Yang, L.; Stuart, A. C.; Price, S. C.; Liu, S.; You, W. Development of Fluorinated Benzothiadiazole as a Structural Unit for a Polymer Solar Cell of 7% Efficiency. *Angew. Chemie - Int. Ed.* **2011**, *50*, 2995–2998.
- (98) Olla, T.; Ibraikulov, O. A.; Ferry, S.; Boyron, O.; Méry, S.; Heinrich, B.; Heiser, T.; Lévêque, P.; Leclerc, N. Benzothiadiazole Halogenation Impact in Conjugated Polymers, a Comprehensive Study. *Macromolecules* **2019**, *52*, 8006–8016.
- (99) Hedström, S.; Wang, E.; Persson, P. Defining Donor and Acceptor Strength in Conjugated Copolymers. *Mol. Phys.* **2017**, *115*, 485–496.
- (100) Tang, W.; Huang, Y.; Han, L.; Liu, R.; Su, Y.; Guo, X.; Yan, F. Recent Progress in Printable Organic Field Effect Transistors. *J. Mater. Chem. C* **2019**, *7*, 790–808.

- (101) Hung, L. S.; Zhang, R. Q.; He, P.; Mason, G. Contact Formation of LiF/Al Cathodes in Alq-Based Organic Light-Emitting Diodes. *J. Phys. D. Appl. Phys.* **2002**, *35*, 103–107.
- (102) Huang, K.; Zhao, X.; Du, Y.-C.; Kim, S.; Wang, X.; Lu, H.-B.; Cho, K.; Zhang, G.; Qiu, L. Modulating Charge Transport Characteristics of Bis-Azaaisoindigo-Based D–A Conjugated Polymers through Energy Level Regulation and Side Chain Optimization. *J. Mater. Chem. C* **2019**, *7*, 7618–7626.
- (103) Hoefler, S. F.; Haberfehlner, G.; Rath, T.; Canteri, R.; Barozzi, M.; Hofer, F.; Trimmel, G. Elemental Nanoanalysis of Interfacial Alumina–Aryl Fluoride Interactions in Fullerene-Free Organic Tandem Solar Cells. *Adv. Mater. Interfaces* **2019**, 1901053.
- (104) Casado, J.; Zgierski, M. Z.; Ewbank, P. C.; Burand, M. W.; Janzen, D. E.; Mann, K. R.; Pappenfus, T. M.; Berlin, A.; Pérez-Inestrosa, E.; Ortiz, R. P.; Navarrete, J. T. L. Exploration of Ground and Excited Electronic States of Aromatic and Quinoid S,S-Dioxide Terthiophenes. Complementary Systems for Enhanced Electronic Organic Materials. *J. Am. Chem. Soc.* **2006**, *128*, 10134–10144.
- (105) Dell, E. J.; Capozzi, B.; Xia, J.; Venkataraman, L.; Campos, L. M. Molecular Length Dictates the Nature of Charge Carriers in Single-Molecule Junctions of Oxidized Oligothiophenes. *Nat. Chem.* **2015**, *7*, 209–214.
- (106) Meng, B.; Miao, J.; Liu, J.; Wang, L. A New Polymer Electron Acceptor Based on Thiophene-S,S-Dioxide Unit for Organic Photovoltaics. *Macromol. Rapid Commun.* **2018**, *39*, 1700505.
- (107) Cao, H.; Bauer, N.; Pang, C.; Rech, J.; You, W.; Rupar, P. A. End-Cap Group Engineering of a Small Molecule Non-Fullerene Acceptor: The Influence of Benzothiophene Dioxide. *ACS Appl. Energy Mater.* **2018**, *1*, 7146–7152.
- (108) Leclerc, N.; Michaud, A.; Sirois, K.; Morin, J.-F.; Leclerc, M. Synthesis of 2,7-Carbazolenevinylene-Based Copolymers and Characterization of Their Photovoltaic Properties. *Adv. Funct. Mater.* **2006**, *16*, 1694–1704.
- (109) Barbarella, G.; Bongini, A.; Mastragostino, M.; Arbizzani, C.; Sotgiu, G.; Zambianchi, M.; Favaretto, L. Controlling the Electronic Properties of Polythiophene through the Insertion

- of Nonaromatic Thienyl S,S-Dioxide Units. *Chem. Mater.* **2002**, *11*, 2533–2541.
- (110) Nagasawa, H.; Sugihara, Y.; Ishii, A.; Nakayama, J. Thiophene 1,1-Dioxide: Synthesis, Isolation, and Properties. *Bull. Chem. Soc. Jpn.* **1999**, *72*, 1919–1926.
- (111) Barbarella, G.; Pudova, O.; Arbizzani, C.; Mastragostino, M.; Bongini, A. Oligothiophene-S,S-Dioxides: A New Class of Thiophene-Based Materials. *J. Org. Chem.* **1998**, *63*, 1742–1745.
- (112) Barbarella, G.; Favaretto, L.; Sotgiu, G.; Zambianchi, M.; Antolini, L.; Pudova, O.; Bongini, A. Oligothiophene S,S-Dioxides. Synthesis and Electronic Properties in Relation to the Parent Oligothiophenes. *J. Org. Chem.* **1998**, *63*, 5497–5506.
- (113) Barbarella, G.; Favaretto, L.; Sotgiu, G.; Zambianchi, M.; Bongini, A.; Arbizzani, C.; Mastragostino, M.; Anni, M.; Gigli, G.; Cingolani, R. Tuning Solid-State Photoluminescence Frequencies and Efficiencies of Oligomers Containing One Central Thiophene-S,S-Dioxide Unit. *J. Am. Chem. Soc.* **2000**, *122*, 11971–11978.
- (114) Pappenfus, T. M.; Melby, J. H.; Hansen, B. B.; Sumption, D. M.; Hubers, S. A.; Janzen, D. E.; Ewbank, P. C.; McGee, K. A.; Burand, M. W.; Mann, K. R. Reverse Selectivity in M-CPBA Oxidation of Oligothiophenes to Sulfones. *Org. Lett.* **2007**, *9*, 3721–3724.
- (115) Miller, L. L.; Yu, Y. Synthesis of β -Methoxy, Methyl-Capped α -Oligothiophenes. *J. Org. Chem.* **1995**, *60*, 6813–6819.
- (116) Amir, E.; Rozen, S. Synthesis of [All]-S,S-Dioxide Oligothiophenes Using HOF·CH₃CN. *Angew. Chemie - Int. Ed.* **2005**, *44*, 7374–7378.
- (117) Dayan, S.; Bareket, Y.; Rozen, S. An Efficient α -Hydroxylation of Carbonyls Using the HOF·CH₃CN Complex. *Tetrahedron* **1999**, *55*, 3657–3664.
- (118) Nenajdenko, V. G.; Gavryushin, A. E.; Balenkova, E. S. A Facile Route to Thiophene-1,1-Dioxides Bearing Electron-Withdrawing Groups. *Tetrahedron Lett.* **2001**, *42*, 4397–4399.
- (119) Moiseev, A. M.; Balenkova, E. S.; Nenajdenko, V. G. Thiophene 1,1-Dioxides as Unique Building Blocks in Modern Organic Synthesis and Materials Chemistry. *Russ. Chem. Rev.* **2006**, *75*, 1015–1048.

- (120) Coombs, B. A.; Rutter, S. R.; Goeta, A. E.; Sparkes, H. A.; Batsanov, A. S.; Beeby, A. 2,5-Bis(Arylethynyl)Thienyl Systems: Preparation and Photophysical Properties. Part II. *RSC Adv.* **2012**, *2*, 1870–1876.
- (121) Tsai, C.-H. H.; Chirdon, D. N.; Maurer, A. B.; Bernhard, S.; Noonan, K. J. T. T. Synthesis of Thiophene 1,1-Dioxides and Tuning Their Optoelectronic Properties. *Org. Lett.* **2013**, *15*, 5230–5233.
- (122) Nichols, M. A.; Williard, P. G. Solid-State Structures of n-Butyllithium-TMEDA, -THF, and -DME Complexes. *J. Am. Chem. Soc.* **1993**, *115*, 1568–1572.
- (123) Snieckus, V. Directed Ortho Metalation. Tertiary Amide and O-Carbamate Directors in Synthetic Strategies for Polysubstituted Aromatics. *Chem. Rev.* **1990**, *90*, 879–933.
- (124) Wei, S.; Xia, J.; Dell, E. J.; Jiang, Y.; Song, R.; Lee, H.; Rodenbough, P.; Briseno, A. L.; Campos, L. M. Bandgap Engineering through Controlled Oxidation of Polythiophenes. *Angew. Chemie Int. - Ed.* **2014**, *53*, 1832–1836.
- (125) Dell, E. J.; Campos, L. M. The Preparation of Thiophene-S,S-Dioxides and Their Role in Organic Electronics. *J. Mater. Chem.* **2012**, *22*, 12945–12952.
- (126) Shockravi, A.; Mallakpour, S.; Atabaki, F. Synthesis and Characterization of New Poly(Sulfoxide-Ether-Amide)s from 2,2'-Sulfoxide Bis(4-Methyl Phenoxy Acetic Acid) and Various Diisocyanates. *Des. Monomers Polym.* **2008**, *11*, 261–269.
- (127) Nyquist, R. Epoxides and Ethers. In *Interpreting Infrared, Raman, and Nuclear Magnetic Resonance Spectra*; 2001; Vol. 2: Factors, pp 1–26.
- (128) Lachkar, A.; Selmani, A.; Sacher, E.; Leclerc, M.; Mokhliss, R. Metallization of Polythiophenes I. Interaction of Vapor-Deposited Cu, Ag and Au with Poly(3-Hexylthiophene) (P3HT). *Synth. Met.* **1994**, *66*, 209–215.
- (129) Lindberg, B. J.; Hamrin, K.; Johansson, G.; Gelius, U.; Fahlman, A.; Nordling, C.; Siegbahn, K. Molecular Spectroscopy by Means of ESCA II. Sulfur Compounds. Correlation of Electron Binding Energy with Structure. *Phys. Scr.* **1970**, *1*, 286–298.
- (130) Ashraf, R. S.; Kronemeijer, A. J.; James, D. I.; Sirringhaus, H.; McCulloch, I. A New

Thiophene Substituted Isoindigo Based Copolymer for High Performance Ambipolar Transistors. *Chem. Commun.* **2012**, 48, 3939–3941.

- (131) Kim, G.; Kang, S.-J. J.; Dutta, G. K.; Han, Y.-K. K.; Shin, T. J.; Noh, Y.-Y.; Yang, C. A Thienoisindigo-Naphthalene Polymer with Ultrahigh Mobility of 14.4 cm²/V·s That Substantially Exceeds Benchmark Values for Amorphous Silicon Semiconductors. *J. Am. Chem. Soc.* **2014**, 136, 9477–9483.
- (132) Buckley, C.; Thomas, S.; McBride, M.; Yuan, Z.; Zhang, G.; Bredas, J. L.; Reichmanis, E.; Brédas, J.-L.; Reichmanis, E. Synergistic Use of Bithiazole and Pyridinyl Substitution for Effective Electron Transport Polymer Materials. *Chem. Mater.* **2019**, 31, 3957–3966.
- (133) Shi, Y.; Guo, H.; Qin, M.; Zhao, J.; Wang, Y.; Wang, H.; Wang, Y.; Facchetti, A.; Lu, X.; Guo, X. Thiazole Imide-Based All-Acceptor Homopolymer: Achieving High-Performance Unipolar Electron Transport in Organic Thin-Film Transistors. *Adv. Mater.* **2018**, 30, 1–8.
- (134) Ni, Z.; Wang, H.; Dong, H.; Dang, Y.; Zhao, Q.; Zhang, X.; Hu, W. Mesopolymer Synthesis by Ligand-Modulated Direct Arylation Polycondensation towards n-Type and Ambipolar Conjugated Systems. *Nat. Chem.* **2019**, 11, 271–277.
- (135) Langis-Barsetti, S.; Maris, T.; Wuest, J. D. Molecular Organization of 2,1,3-Benzothiadiazoles in the Solid State. *J. Org. Chem.* **2017**, 82, 5034–5045.
- (136) Grenier, F.; Goudreau, K.; Leclerc, M. Robust Direct (Hetero)Arylation Polymerization in Biphasic Conditions. *J. Am. Chem. Soc.* **2017**, 139, 2816–2824.
- (137) Grenier, F.; Aïch, B. R.; Lai, Y.-Y.; Guérette, M.; Holmes, A. B.; Tao, Y.; Wong, W. W. H.; Leclerc, M. Electroactive and Photoactive Poly[Isoindigo-Alt-EDOT] Synthesized Using Direct (Hetero)Arylation Polymerization in Batch and in Continuous Flow. *Chem. Mater.* **2015**, 27, 2137–2143.
- (138) Sonar, P.; Singh, S. P.; Li, Y.; Soh, M. S.; Dodabalapur, A. A Low-Bandgap Diketopyrrolopyrrole-Benzothiadiazole-Based Copolymer for High-Mobility Ambipolar Organic Thin-Film Transistors. *Adv. Mater.* **2010**, 22, 5409–5413.
- (139) Gaussian 16, Revision C.01, Frisch, M. J.; Trucks, G. W.; Schlegel, H. B.; Scuseria, G. E.; Robb, M. A.; Cheeseman, J. R.; Scalmani, G.; Barone, V.; Petersson, G. A.; Nakatsuji, H.;

Li, X.; Caricato, M.; Marenich, A. V.; Bloino, J.; Janesko, B. G.; Gomperts, R.; Mennucci, B.; Hratchian, H. P.; Ortiz, J. V.; Izmaylov, A. F.; Sonnenberg, J. L.; Williams-Young, D.; Ding, F.; Lipparini, F.; Egidi, F.; Goings, J.; Peng, B.; Petrone, A.; Henderson, T.; Ranasinghe, D.; Zakrzewski, V. G.; Gao, J.; Rega, N.; Zheng, G.; Liang, W.; Hada, M.; Ehara, M.; Toyota, K.; Fukuda, R.; Hasegawa, J.; Ishida, M.; Nakajima, T.; Honda, Y.; Kitao, O.; Nakai, H.; Vreven, T.; Throssell, K.; Montgomery, J. A., Jr.; Peralta, J. E.; Ogliaro, F.; Bearpark, M. J.; Heyd, J. J.; Brothers, E. N.; Kudin, K. N.; Staroverov, V. N.; Keith, T. A.; Kobayashi, R.; Normand, J.; Raghavachari, K.; Rendell, A. P.; Burant, J. C.; Iyengar, S. S.; Tomasi, J.; Cossi, M.; Millam, J. M.; Klene, M.; Adamo, C.; Cammi, R.; Ochterski, J. W.; Martin, R. L.; Morokuma, K.; Farkas, O.; Foresman, J. B.; Fox, D. J. Gaussian, Inc., Wallingford CT, 2016.